Finite Element Analysis of Vibrations on Flexible Structures due to Turbulent Wind

by

Jordann Jubinville-Baron

Department of Civil Engineering and Applied Mechanics

McGill University
Montréal, Québec, Canada
August 2019

A Thesis submitted to McGill University in partial fulfillment of the requirements of the degree of Master's of Civil Engineering

[This page intentionally left blank]

Abstract

Wind load effects have a major impact on the design of numerous civil engineering structures. Building codes such as the National Building Code of Canada (NBC, 2015), the American Society of Civil Engineers Standards (ASCE-7, 2016) and the Eurocodes (Eurocode 8, 2016) display great details about the static effect of wind on different building shapes, surfaces and isolated exposed components. However, these standards provide very limited guidance on dynamic effects and current design methods are limited in scope and applicability, since they are based on dating experimental data such as a research from Vickery and Basu (1983), which did not use sophisticated experimental techniques as available nowadays. This research presents a dynamic analysis of two flexible telecommunication monopoles and a cantilevered sign structure, under static, harmonic and random wind loads using the nonlinear finite element analysis software ADINA. The analysis does not consider wind-structure dynamic interactions. The objective of this study is to investigate the response of different structures to a combination of wind actions and monitor any excessive or dangerous vibrations that may be engendered by resonance phenomena. Furthermore, the cyclic vibrations produced by wind can be used to assess the vulnerability of the modelled structures to fatigue and approximate their useful fatigue life. By modelling existing structures, field data can eventually be used to validate and adjust the models in order to mimic reality as much as possible and minimize uncertainty related to numerical predictions.

After applying 100 random wind time histories to the three structures, it was first found that, for monopole structures, the suggested gust factor of 2.0 by CAN/CSA S37-18 is accurate in predicting the dynamic amplification produced by natural wind gusts, with maximum tip displacements values found to be amplified by 51% and 98% in comparison with the maximum equivalent static load. With further analysis of the critical case, the stress range was determined and compared to the fatigue limit of the material according to the S-N curve method (Wohler, 1855). It was found that the stress range would not exceed 50% of the value of the endurance limit of steel after 10^8 cycles of vibration for

both monopoles. Thus, according to this method and under normal operating conditions, these two telecommunication towers will not likely suffer fatigue damages. Ambient Vibration Measurements (AVMs) were taken on one monopole and the first three modes of vibration of the structure as well as the damping corresponding to the first mode were obtained. It was found that the numerical model was about 10% stiffer than its real-life rendering. As such, the numerical model was adjusted beforehand to erase that disparity.

The cantilevered sign structure was subjected to the same 100 random wind time histories and the maximum displacement observed at the end of the cantilever was 25 mm. This value corresponds to a 150% dynamic amplification from the maximum equivalent static load of 10 mm. CAN/CSA S6-18 proposes a gust factor value of 2.5 which corresponds to the exact amplification value found through dynamic numerical analysis. Once again, fatigue analysis showed results of stress range under 30% of the endurance limit of steel for this particular cantilevered sign structure after 10^8 cycles of vibration. Therefore, according to the S-N method (Wohler, 1855) and under normal operating conditions, this cantilevered sign structure will not likely suffer fatigue damages. Ambient Vibration Measurements (AVMs) were also taken on the sign structure and the first 4 modes of vibration of the structure were obtained. It was found that the numerical model was about 13% stiffer than its real-life rendering. Therefore, the numerical model was once again adjusted beforehand to correspond to the actual values measured in-situ.

Sommaire

Les effets du vent ont un impact majeur sur la conception de nombreux ouvrages de génie civil. Les codes du bâtiment tels que le Code National du Bâtiment du Canada (CNB, 2015), les normes de l' «American Society of Civil Engineers» (ASCE-7, 2016) et l'Eurocode (Eurocode 8, 2016) contiennent beaucoup de détails pour évaluer les effets statiques du vent sur différentes formes et surfaces de bâtiments ainsi que sur certaines composantes exposées. Toutefois, ces codes ne procurent que très peu de détails sur les effets dynamiques du vent et les méthodes de conception courantes sont limitées en terme d'applicabilité puisqu'elles sont basées sur des données expérimentales veillissantes telles qu'obtenues par Vickery et Basu (1983), alors que les méthodes de mesures n'étaient pas aussi avancées qu'aujourd'hui. Cette recherche présente une analyse dynamique de deux structures de télécommunication (monopôles) et d'une structure de signalisation routière en porte-à-faux, sous une charge de vent statique, harmonique et aléatoire à l'aide du logiciel d'éléments finis ADINA. Cette analyse ne considère pas les interactions dynamiques entre le vent et la structure. L'objectif de cette étude est d'investiguer la réponse de différentes structures flexibles à une combinaison d'actions du vent et de surveiller quelconque vibration excessive ou dangeureuse qui pourrait être engendrée par des phénomènes de résonance. De plus, les cycles de vibrations produits par le vent peuvent être utilisés pour évaluer la vulnérabilité des structures modélisées à la fatigue et estimer leur durée de vie utile. Puisque des structures existantes sont modélisées, des données sur le terrain peuvent être utilisées pour valider et ajuster les modèles afin de mieux représenter la réalité et minimiser l'incertitude quant aux prédictions numériques.

Suite à l'application de 100 historiques de vent aléatoire sur les trois structures, il fut determiné que, pour les monopôles, le facteur de rafale de 2.0 suggéré par le CAN/CSA S37-18 est juste dans sa prédiction de l'amplification dynamique causée par les rafales de vent naturel, avec des valeurs de déplacement maximal au sommet amplifiées par 51% et 98% par rapport au déplacement statique maximal. En poussant l'analyse du cas

critique, l'intervalle des contraintes fut déterminé et comparé à la limite de fatigue du matériau selon la méthode classique des coubes S-N (Wholer, 1855). Il fut trouvé que l'intervalle des contraintes ne dépasse pas 50% de la valeur de l'endurance limite de l'acier après 10^8 cycles de vibration pour les deux monopôles. Donc, selon cette méthode et sous conditions d'opérations normales, ces deux tours de télécommunication ne souffriront probablement pas de dommages liés à la fatigue. Des Mesures de Vibrations Ambiantes (MVAs) ont été prises sur l'un des monopôles et les trois premiers modes de vibration de la structure ainsi que la valeur de l'amortissement interne correspondant au premier mode ont été obtenues. Il fut trouvé que le modèle numérique était environ 10% plus rigide que son homologue réel. Cela étant dit, le modèle numérique fut ajusté avant d'entreprendre les analyses pour éffacer cetter disparité.

La structure de signalisation en porte-à-faux fut sujette aux 100 mêmes historiques de vent aléatoire et le déplacement horizontal maximal observé à l'extrémité du porte-à-faux fut de 25 mm. Cette valeur correspond à une amplification dynamique de 150% par rapport au déplacement statique équivalent de 10 mm. Le CAN/CSA S6-18 propose un facteur de rafale de 2.5 ce qui correspond exactement à la valeur de l'amplification trouvée par l'analyse dynamique numérique. Encore une fois, l'analyse de la fatigue a démontré un intervalle de contraintes de moins de 30% de l'endurance limite de l'acier pour cette structure de signalisation après 10^8 cycles de vibration. Ce faisant, selon le méthode classique des courbes S-N (Wohler, 1855) et sous conditions normales d'opération, cette structure de signaliation ne devrait pas souffrir de dommages liés à la fatigue. Des Mesures de Vibrations Ambiantes (MVAs) ont également été prises sur cette structure de signalisation et les quatre premiers modes de vibration de la structure ont été obtenus. Il fut trouvé que le modèle numérique était environ 13% plus rigide que son homologue réel dans ce cas. Donc, le modèle numérique fut ajusté avant d'entreprendre les analyses afin de correspondre aux valeurs mesurées sur le site.

Acknowledgements

I would like to express the deepest appreciation to my supervisor, Professor Ghyslaine McClure, who has been accompanying me throughout this journey. Her knowledge and competence in the field have been an inestimable asset for the completion of this research. On a more personal level, her devotement and implication towards my personal development have made me grow as a person for which I will be forever grateful.

I would also like to thank all the collaborators, including M. Marcel Vallières and Ms. Lina Garcia from MTQ, M. César Galvez from Telecon, Ms. Sylvie Fortin and Ms. Mihaela Onita from Vidéotron for their help in gathering crucial data for the realisation of this thesis.

Also, I would like to thank the Centre d'études Interuniversitaire sur les Structures sous Charges Extrêmes (CEISCE) for their financial support through research assistantship.

In addition, I would like to extend my gratitude to my parents for their continuous support and encouragements throughout my educational journey. I also thank the rest of my family for their good words and interest in my academic adventure.

Finally, a big thanks to my close friends for taking my head out of my books and making sure that I keep having fun with the simple things in life.

List of Figures

List of Tables

List of symbols

A_s = Net projected area exposed to wind

a_L = Normalised limiting amplitude

C_a, C_p = Wind speed-up factor

C_C = Aerodynamic constant dependent on the cross-sectional shape

C_d = Drag coefficient

C_e = Height factor

C_g = Gust effect factor

c_{lat} = Lateral force coefficient

D = Across-wind dimension of the body

d = Linear viscous damping coefficient

D_H = Pole diameter averaged over the top third of the structure

d_{max} = Maximum tip displacement in a pure harmonic loading case

E = Modulus of elasticity of the material

e : Internal energy per unit mass

E_{adj} = Adjusted modulus of elasticity after model calibration

E_i = Initial modulus of elasticity before model calibration

$(EPA)_{ST,A}$ = Effective wind projected area of structure

F_A = Design wind force on appurtenances

f = Natural frequency of structure

F_G = Design wind force on guys

F_i : Component of body force in the i-direction

f_m = Natural frequency of the structure measured in-situ

f_n = Natural frequency of the structure initially found with the computer model

f_s = Shedding frequency of vortices

F_{ST} = Design wind force on the structure

F_{vs} = Equivalent static wind load for vortex shedding considerations

F_W = Design total wind load

$F_w(s)$ = Inertial force per unit length perpendicular to the wind direction

G_h = Gust effect factor

g = Expected wind peak factor

I = Importance factor

I_F = Fatigue importance factor

k = Spring stiffness constant

K = Mode shape factor

K_a = Aerodynamic damping parameter

K_d = Wind direction probability factor

k_p = Peak factor

K_W = Effective correlation length factor

K_z = Velocity pressure coefficient

K_{zt} = Topographic factor

l = Characteristic linear dimension

λ = Aspect ratio of the structure

m_H = Pole mass per unit length averaged over the top one-third of the structure

$m(s)$ = Vibrating mass of the structure per unit length

m = Mass of the structure

$n_{i,y}$ = Natural frequency of the structure in mode i

p = Wind pressure

P_G = Equivalent static galloping force

P_{NW} = Equivalent static natural wind gust pressure

P_{TG} = Equivalent static truck gust pressure

$\varphi_{i,y}(s)$ = Mode shape of the structure normalised to 1 at the max. amplitude in mode i

q_{10} = 10-year return period mean hourly wind pressure at 10 m above ground

q_{wg} = Natural wind gust pressure

$\boldsymbol{q}$: Heat flux vector

q = Reference velocity pressure

q_z = Wind velocity pressure

q_H = Wind pressure corresponding to the critical wind velocity at the top of the structure

R = Stress ratio of cyclic stresses

Re = Reynolds number

$R(t)$ = Cross-flow displacement of cylinder

ρ_a = Air density

Sc = Scruton number

s = Span length of the cylinder

S, St = Strouhal number

σ_a = Alternating stress

σ_m = Mean stress

σ_r = Applied stress range

σ_u = Standard deviation on mean wind speed

σ_y = Standard deviation on the displacement

σ_{ys} = Yield strength

σ_u = Ultimate strength

t = Time

T = Temperature

t_i = Turbulence intensity of the wind periodic function

τ_i = Shear stress in j-direction exerted on plane with normal in the i-direction

$\overline{U}$ = Mean wind speed

$u(t)$ = Longitudinal wind speed

$u'(t)$ = Fluctuating wind speed component

μ = Dynamic viscosity of air

v_i = Fluid velocity in the x, y or z direction

V = Mean velocity of the flow

ν = Kinematic viscosity of air

V= Basic wind speed for the loading condition under investigation

W = Wind load

ω = Natural angular frequency

x = Mean value of displacement

$y_{F,max}$ = Maximum displacement over time

ζ_a = Negative aerodynamic damping associated with vortex shedding

ζ_s = Structural damping ratio

∇ : Del operator of divergence

Table of Contents

1. Introduction

1.1 General

Wind loads generally have a major effect on the design of numerous civil engineering structures. Building codes such as the National Building Code of Canada (NBC, 2015), the American Society of Civil Engineers Standards (ASCE, 2016) and the Eurocodes (Eurocode, 2016) display great details about the static effect of wind on different building shapes, surfaces and isolated exposed components. However, it is a different story for dynamic wind actions as these standards provide very limited guidance on the aforementioned effects and current design methods are limited in scope and applicability, since they are mostly based on a limited number of relatively datedwind tunnel testing data. For instance, the NBC 2015 states that the dynamic effects of vortex shedding on circular and near-circular cylindrical structures can be estimated in accordance with a research from Vickery and Basu (1983). In its commentary I, it is mentioned that realistic wind velocity profiles and turbulence were not simulated in the referenced experiments, such that the proposed calculation methods should be used with caution. Considering that wind effects are typically governing design in areas where the climate is warm and earthquake hazards are low, and that some modern structures are reaching unrivaled heights, investigation of wind effects should be further and continuously conducted to ensure integrity of the structures and their safe operations.

This research is focusing on the study of free-standing steel or aluminum masts such as tubular poles serving as telecommunications structures, signage structures, lighting posts or traffic structures on public roads that are particularly sensitive to wind actions due to their slenderness. Their light weight and simple design have made them widely used (Chien and Jang, 2008). If not recognized and mitigated, sustained wind-induced vibrations can result in fatigue of some structural members and their connections (Peil and Behrens, 2002) and, in some extreme cases, total structural collapse (Caracoglia and Jones, 2006);(Solari and Pagnini, 1999). Several fatigue monopole failures have been reported throughout the years, which confirm the necessity of understanding better their

wind response. Furthermore, modern high-rise buildings tend to be taller and more slender than their predecessors, which makes them more susceptible to dynamic wind action. We anticipate that studies of the dynamic effects of wind on simple tubular masts will eventually be beneficial for more applications, recognizing that wind will affect these constructions differently depending on their respective shape, dimension, stiffness, mass and damping properties.

Recent editions of North American telecommunication structures design codes, such as CSA S37 (2019) in Canada and ANSI/TIA-222 (2017) Structural Standard for Antenna Supporting Structures, Antennas and Small Wind Turbine Support Structures in the US have provided guidelines to address fatigue in poles (monopoles and tripoles, in particular) that preclude the knowledge of their modal damping in the fundamental mode. Damping is a representation of energy dissipation and, in the classical viscous model it exponentially reduces the free vibration of a structure. However, damping is complex and not classical in these structures and comes from a variety of sources: inherent structural damping (hysteretic) provided by constitutive materials, dry friction damping in bolted connections and at contact surfaces of nested cylinders, radiation damping provided by the soil surrounding foundations, and aerodynamic damping, based on the structure's shape and its exposure to wind, where supported antennas and appurtenances modify the aeroelastic properties of the whole system.

1.2 Wind flow

In the lower atmosphere, wind flow is a random time-varying phenomenon composed of eddies of varying sizes and rotational velocities that move air relative to the earth's surface, towards which the relative wind velocity goes to zero (in the case of what is called a no-slip boundary condition). The wind flow can be modeled by a pseudo-static velocity component, consisting of the mean wind speed vector determined for a given duration (typically hourly mean wind speed in structural applications), plus a dynamic component due to wind speed variations from the mean value (turbulence). As explained by Harper

et al (2010), the variation of longitudinal (horizontal) wind speed with time, $u(t)$ can be represented as the sum of the mean wind speed $\overline{U}$ and a fluctuating component $u'(t)$ about the mean as:

$$u(t) = \overline{U} + u'(t) \qquad (1)$$

Furthermore, the expected maximum gust $\widehat{U}$ in a wind history with a mean value of $\overline{U}$ and a standard deviation of σ_u can be determined with:

$$\widehat{U} = \overline{U} + g\sigma_u \qquad (2)$$

Where g is the expected peak factor from a statistically based estimate. The original statistical approach was developed by Davenport (1964) and further refined by Greenway (1979). It considers the sampling of independent gust episodes of natural wind on a chosen period. With the assumption of a Gaussian Parent distribution, the sampling can be shown to produce a Gumbel distribution for the maximum gusts and the mean of this distribution is then taken as the expected value.

However, the measured values such as turbulence intensity, gust wind speed and peak factor are all dependent on the chosen instrument response and on the choice of measuring time period. The most widespread method used is the 3 seconds gust wind speed measurement at 10 m elevation above ground with a 3-cup anemometer. Although this method is fairly simple, there is limited data on the dynamic response characteristics of anemometers in turbulent winds (Miller, 2007).

As such, the wind flow exerts both static and aerodynamic forces on a free-standing exposed structure. The latter category includes drag forces, which act in the direction of the mean wind force vector, and the lift forces, which act perpendicular to the previously mentioned direction. These forces act at the center of pressure of the exposed component, which is not a fixed point and will vary as the angle of attack is varied, thus inducing a variable pitching moment that can be evaluated from a fixed reference.

When air is flowing around a bluff body (a solid body with flow separation over much of its surface due to its non-streamlined shape), large and small eddies are formed and

vortices are shed downstream alternately and periodically from either side of the body. These vortices are low-pressure zones towards which the object will tend to move and will therefore induce cross-wind oscillations (perpendicular to the wind flow), called vortex-shedding oscillations. Depending on the characteristics of the wind flow turbulence, these oscillations may be sustained or not, but they are not necessarily dangerous for the structure. However, if the frequency of this steady vortex shedding coincides with one of the lower natural frequencies of the bluff body, resonance or quasi-resonance (covering a range of critical natural frequencies) will occur, and large displacements will occur, which may cause important alternate stresses in structural joints and affect the fatigue life of the structure. Vortex shedding will only occur in a specific range of wind speeds governed by the Strouhal number relation (Equation 6).

In elastic structures, such displacements further increase as dynamic interactions between the moving structure and its surrounding air flow occur, and the aerodynamic damping exceeds the inherent structural damping. At that point, self-induced oscillations develop which may lead to eventual failure. This aerodynamic instability is called flutter. Flutter is very dangerous and must be avoided with proper structural design or vibration suppression measures. Unfortunately, flutter conditions are difficult to establish for geometrically complex structures.

Galloping is another form of flutter typically associated with a laminar wind flow (Hémon et al., 2016). It is defined as the large amplitude and low frequency self-induced cross-wind oscillations of flexible structures due to aerodynamic forces that are in-phase with the motion of the structure. A progressively increasing amplitude of transverse vibrations is generated with increased wind speed. Conductor galloping is a particular design concern in overhead transmission lines.

Buffeting, another wind-induced response, is defined as an irregular along-wind motion of a structure excited by turbulence in the flow (Fung, 2002). It has been observed generally to occur in slender towers or bridge decks. Since buffeting is associated with the turbulence in the wind, the response of the structure is usually larger at higher wind

speeds for a given turbulence intensity, and larger at higher turbulence intensity for a given wind speed.

It is important to recognize that problems related to wind-induced instabilities can arise from frequency coincidence with more than the fundamental mode of the structure. In fact, Samali (1998) has investigated the contribution of higher natural frequency components, particularly in the first four modes, by eigenvalue analysis on the response of tall structures to wind. Even though the fundamental mode of the structure generally governs the response, higher modes may have an impact depending on the mass distribution of the structure. Hence, higher modes shall not be disregarded.

Although free-standing tubular structures are intentionally flexible and able to sustain relatively large displacements, fatigue problems can arise after a large number of cyclic loadings. Fatigue is the weakening of the material caused by the repeated loading and unloading action. Under such treatment, a material may display a much lower ultimate capacity than under monotonic static loads, sometimes less than 50% for steel and even worse for aluminum that has negligible capacity after a large number of cycles as shown in Figure 1.

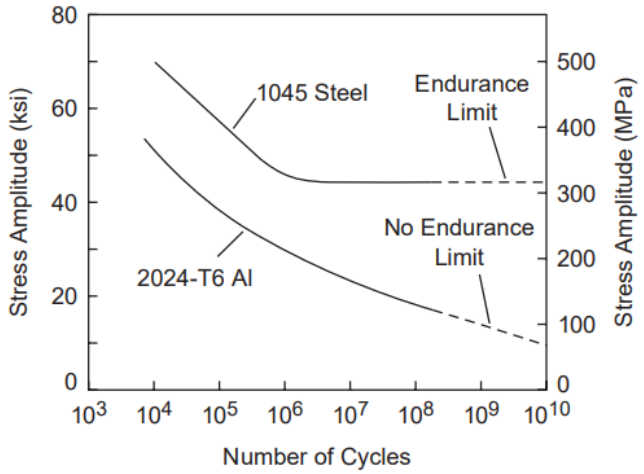

Figure 1: Comparison of Steel and Aluminum Fatigue behavior (Kalpakjian, 1995)

Fatigue life is often assessed using S-N curves, representing the magnitude of alternating stress versus the number of cycles to failure. When alternate cycles of compression and tension are applied to the structure, some progressive, localized and permanent change

occurs at the microstructure level which may lead to crack formation and potential catastrophic failure. In masts, cracks are generally found at the base connection of the structure, where bending stresses are higher and in zones of stress concentrations. Welds and surrounding areas are usually more concerned than bolted connections due to a greater stiffness differential and the presence of residual stresses. (Chen et al., 2001).

1.3 Research Objectives

This research presents a dynamic analysis of flexible structures, such as telecommunication monopoles and cantilevered signalisation structures, under static, harmonic and random wind loads using the nonlinear finite element analysis software ADINA (2019).

As previously mentioned, international standards tend to separate dynamic wind effects into independent phenomena for simplicity. However, in reality, these different actions usually interact together to create a combination of responses in the structure of interest. The objective of this study is to investigate the response of different structures to a combination of wind actions and monitor any excessive or dangerous vibrations that may be engendered.

Furthermore, the cyclic vibrations produced by wind can be used to assess the vulnerability of the modelled structures to fatigue and approximate their useful life.

By modelling existing structures, field data can eventually be used to validate and adjust the models in order to mimic reality as much as possible and minimize uncertainty related to numerical errors.

1.4 Methodology

Three structures were selected to be analysed for this study: two telecommunication towers (monopoles) and one cantilevered sign structure. Each structure will be subjected

to the same analysis procedure. First, it will be modeled with finite elements using ADINA according to the structural drawings provided. Then, the optimal meshing density will be found by increasing the density until the natural frequency of the structure converges to a predetermined tolerance. By doing so, the model will have a high level of detail and precision while avoiding unnecessary calculation time. Once optimality is reached, the maximum equivalent static load (applied as a pressure on all exposed surfaces) according to each structure's location will be calculated and applied to the model. Then, a harmonic load calibrated to cause resonance in each structure will be applied in order to observe a theoretical maximum response of the structure. In all cases, the horizontal displacement at the tip of the structure will be monitored and plotted against time. Finally, a series of 100 random wind time histories will be generated using a random number generator and applied to the structures with different average amplitudes, turbulence intensities and frequency content to observe the susceptibility of eachstructure to these different variables.

2. Brief Literature Review

2.1 Governing equations of wind flow

In order to further understand the interaction between the structure and the wind flow eventually causing instabilities, the basic governing laws of physics have to be examined. The flow in consideration is the atmospheric boundary layer, which is a turbulent boundary layer whose variation of the moving air properties can normally be neglected in the context of flow in urban areas (Arya and Plate, 1969). Wind flow can be described using the well-known continuity and momentum equations, consisting in the Navier-Stokes equations, in addition to the energy equation. These equations are shown below as presented in Panton's textbook (2005).

2.1.1 Continuity equation

The continuity equation holds its name to emphasize that the continuum assumptions, stating that fluid density and velocity can be defined at every point in space, are prerequisites. The continuity equation is derived from the conservation of mass: the time rate of change of the mass of a material region is zero. Firstly derived by Euler in 1757, the differential form of the continuity equation in symbolic notation can be written as

$$\frac{\partial \rho}{\partial t} + \nabla \cdot (\rho v_i) = 0 \qquad (3)$$

where

ρ : Density of the fluid

t : Time

∇ : Del operator of divergence

v_i : Fluid velocity in the x, y or z direction

2.1.2 Momentum equation

The momentum equation for a continuum is the analogue of Newton's second law for a single point mass. It is based on the following principle: the time rate of change of the linear momentum of a material region is equal to the sum of the forces on the region. Two types of forces may be encountered: body forces, which act on the core of the material in the region, and surface forces, which act on its boundary (Panton, 2005). The equation can be written as:

$$\partial_t(\rho v_i) + \partial_j\left(\rho v_i v_j\right) = -\partial_i p + \partial_j \tau_{ji} + \rho F_i \quad (4)$$

where

p : Pressure

τ : Shear stress in j-direction exerted on plane with normal in the i-direction

F_i : Component of body force in the i-direction

2.1.3 Energy equation

The energy equation is derived from the first law of thermodynamics, which states that the increase in energy of a material region is the result of work and heat transfer of the region. The differential equation governing the total energy at any point in the continuum in symbolic notation is expressed as

$$\frac{\partial}{\partial t}\left[\rho\left(e + \frac{1}{2}v^2\right)\right] + \nabla \cdot \left[\rho \boldsymbol{v}\left(e + \frac{1}{2}v^2\right)\right] = -\nabla \cdot \boldsymbol{q} + \nabla \cdot (\boldsymbol{T} \cdot \boldsymbol{v}) + \rho \boldsymbol{v} \cdot \boldsymbol{F} \quad (5)$$

where

e : Internal energy per unit mass

$\boldsymbol{q}$: Heat flux vector

$\boldsymbol{T}$: Temperature (°C)

The energy equation is used in many different forms and can be split into two equations: the mechanical energy equation and the thermal energy equation. Further derivations can be found in Panton's textbook (2005).

2.2 Wind flow around 2-D shapes

2.2.1 Vortex Shedding

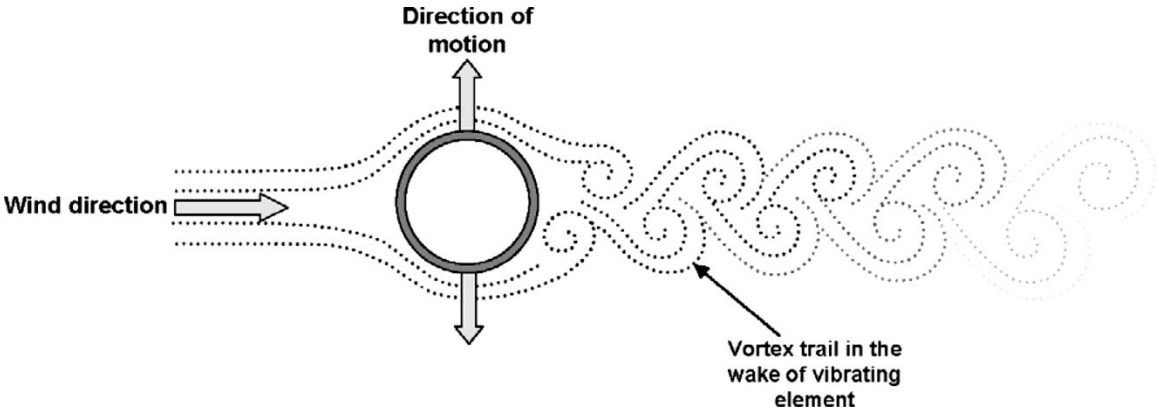

Figure 2: Vortex shedding caused by wind flow past a 2-D cylinder (Rice et al., 2007)

The shedding frequencies of the vortices in the wake of the object are controlled by the Strouhal relationship, which can be expressed as

$$S = \frac{Df_s}{V} \tag{6}$$

where D is the across-wind dimension of the body, f_s is the shedding frequency of the vortices, also known as the Strouhal frequency, V is the mean velocity of the flow and S is the Strouhal number (Strouhal, 1878). As such, S also depends on the Reynolds number defined as

$$Re = \frac{\rho v l}{\mu} \tag{7}$$

However, the variation of Strouhal number is limited between 0.15 and 0.30 (Zhou et al., 2009) so a range of critical velocities can be determined. Problems arise when the ''lock-in'' phenomenon occurs, where the natural frequency of the body controls the shedding of the vortices when it is close to the Strouhal frequency. In this state, the fluid-structure interaction creates steady across-wind oscillations with significant amplitude. This amplitude is self-limiting since aerodynamic damping increases at higher amplitudes (Zuo and Letchford, 2008) but may create a structural fatigue hazard as the number of cycles accumulates, as discussed in the introduction.

Vortex-induced vibration (VIV) of cylinders is a long-established field of study that has been studied in numerous researches. Progress has been summarised throughout the years by papers and books including ones from Parkinson (1974), Sarpkaya (2004), Bearman (1984) and Williamson and Govardhan (2004) amongst others.

Recent research efforts have used computational simulations to explore vortex-induced vibration (VIV) and vortex shedding of circular and polygonal cylindrical shapes in particular as they are commonly used in exposed structures (Placzek et al., 2009); (Garrett, 2003); (Blevins, 1990).

Besem et al. (2016) have developed a simplified aeroelastic model for vortex-induced vibrating cylinders subject to frequency lock-in. They calculate the response amplitude of an elastically supported cylinder experiencing vortex-induced vibrations by coupling a computational fluid dynamic (CFD) model of the flow to a structural model representation of the elastically supported cylinder. Three cases were analysed: the cylinder vibrating transverse to the flow, in-line with the flow and with both degrees of freedom.

In the first experiment, the researchers considered a single-degree-of-freedom spring-mass-viscous damper model as illustrated in Figure 3.

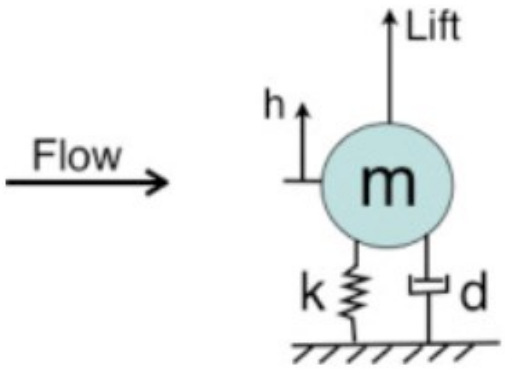

Figure 3: Representation of the cylinder in cross-flow as a spring-mass-viscous damper system (Besem et al., 2016)

In the paper, the authors derived the aeroelastic equation for the self-excited cylinder in cross-flow as

$$R(t) = m\frac{d^2h}{dt^2} + d\frac{dh}{dt} + kh - \frac{1}{2}\rho_\infty U_\infty^2 Dsc_l = 0 \tag{8}$$

where D is the circular cylinder diameter, with mass m and span s, representing the length of the cylinder, supported by a spring stiffness constant k, and a damper with linear viscous dimensional damping d. The non-dimensional, unsteady aerodynamic force c_l is dependent on the unsteady displacement of the cylinder h(t) and Reynolds number Re. The flow is characterized by a free stream density ρ and velocity U. After considering the motion of the cylinder and the sectional lift coefficient to be periodic in time with a fundamental frequency ω, the governing equations as such become

$$(-\omega^2 m + k)\bar{h}_{c_1} - \frac{1}{2}\rho_\infty U_\infty^2 Ds\bar{c}_{lc_1} = 0 \tag{9}$$

$$-\omega d\bar{h}_{c_1} - \frac{1}{2}\rho_\infty U_\infty^2 Dsc_{l_{s_1}} = 0 \tag{10}$$

Or, in non-dimensionalized form

$$(-\kappa^2 Re_\infty^2 St_\infty^2 + 1)\bar{h}_{c_1} - \frac{\kappa^2}{2\mu\pi^3} Re_\infty^2 c_{lc_1}\left(Re_\infty, St_\infty, \bar{h}'_{c_1}\right) = 0 \tag{11}$$

$$-2\kappa\xi Re_\infty St_\infty \bar{h}'_{c_1} - \frac{\kappa^2}{2\mu\pi^3} Re_\infty^2 c_{ls_1}\left(Re_\infty, St_\infty, \bar{h}'_{c_1}\right) = 0 \qquad (12)$$

where

$$\bar{h}'_{c_1} = \frac{\bar{h}_{c_1}}{D}, \quad \omega = \sqrt{\frac{k}{m}}, \quad \xi = \frac{d}{2m\omega_0}, \quad \mu = \frac{4m}{\pi\rho_\infty D^2 s}, \quad \kappa = \frac{2\pi v_\infty}{\omega_0 D^2}.$$

The full derivation can be found in Besem et al. (2016). They were then able to find results of cylinder oscillation amplitude using the Newton-Raphson method by fixing either the Reynolds number Re or the cross-flow displacement $\bar{h}$.

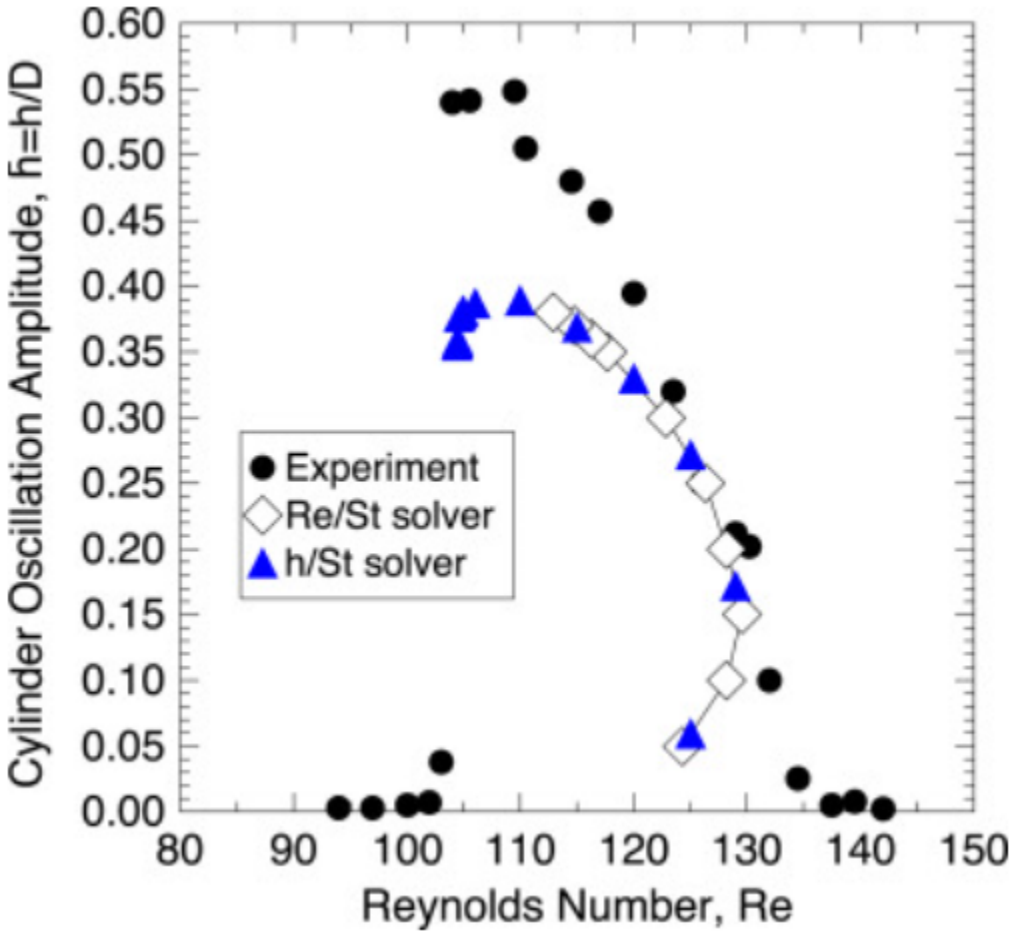

Figure 4: Aeroelastic response of a cylinder in cross flow direction with varying structural parameters (Besem et al., 2016)

Figure 4 compares the aeroelastic response of the model based on two different numerical models with the observed experimental results. Both numerical models yield a similar response at Reynolds number with a peak amplitude at approximately 110. However, a considerable difference is observed in terms of the maximum amplitude of oscillation that is underestimated by the numerical models for the same range of Re. The authors potentially explain this discrepancy by the model simplifications used, including the use of only one harmonic in the equations of motion, a constant viscous structural damping value with the vibration amplitude and no neighboring wall effect (present in the experiments). In that same paper, they have studied the effects of using a two-degrees-of-freedom system numerically, with an in-line and cross-flow oscillation, and have concluded that it would have a negligible impact on the response of the model compared to the previous single-degree-of-freedom system.

2.3 Codes and Standards

2.3.1 EUROCODE

The Eurocode 1, Annex E (informative only), addresses the effects of vortex shedding and aeroelastic instabilities phenomena on exposed structures. It suggests that the effect of vortex shedding be investigated when the ratio of the largest to the smallest crosswind dimension of the structure (slenderness) exceeds 6 or when the critical wind velocity for a given natural mode ''i''of the structure exceeds 1,25 times the characteristic 10 minutes mean wind velocity at the cross section of interest. The annex further suggests calculating the critical wind velocity with equation (11), with a Strouhal number of 0,18 for a circular cross-section. The inertia force per unit length acting perpendicular to the wind direction at location s on the axis of the structure is given by

$$F_w(s) = m(s) \cdot (2 \cdot \pi \cdot n_{i,y})^2 \cdot \varphi_{i,y}(s) \cdot y_{F,max} \qquad (13)$$

where

m(s) : Vibrating mass of the structure per unit length (kg/m)

$n_{i,y}$: Natural frequency of the structure for mode i

$\varphi_{i,y}(s)$: Mode shape of the structure normalised to 1 at the max. amplitude for mode i

$y_{F,max}$: Maximum displacement over time

The Eurocode then proposes two methods for the calculation of the cross-wind displacement amplitudes. The first one is based on several empirically determined factors and is described as

$$\frac{y_{F,max}}{b} = \frac{1}{St^2} \cdot \frac{1}{Sc} \cdot K \cdot K_W \cdot c_{lat} \quad (14)$$

where

St : The Strouhal number

Sc : The Scruton number

K_W : The effective correlation length factor

K : The mode shape factor

c_{lat} : The lateral force coefficient

The K_W, K and c_{lat} factors are empirical values that can be found in Annex E of the Eurocode. It is to be noted that the aeroelastic forces are taken into account by the K_W factor. The second approach is based on the research by Vickery and Basu (1983) who proposed a parabolic function for the aerodynamic damping in accordance with the Rayleigh formulation. The formula is

$$y_{max} = \sigma_y \cdot k_p \quad (15)$$

where

$$\sigma_y = \frac{b}{St^2} \cdot \frac{C_C}{\sqrt{\frac{Sc}{4\pi} - K_a \cdot \left(1 - \left(\frac{\sigma_y}{b \cdot a_L}\right)^2\right)}} \cdot \sqrt{\frac{\rho \cdot b^2}{m_e}} \cdot \sqrt{\frac{b}{h}} \quad (16)$$

and

σ_y : Standard deviation on the displacement

k_p : Peak factor

C_C : Aerodynamic constant dependent on the cross-sectional shape

K_a : Aerodynamic damping parameter

a_L : Normalised limiting amplitude giving the deflection of structures with low damping

ρ : Air density under vortex shedding conditions

m_e : Effective mass per unit length

h, b : Height and width of the structure

The aerodynamic damping parameter K_a depends on the Reynolds number and on the turbulence intensity of the incoming flow. It is defined with a negative parabola proposed by Vickery and Basu (1983) and shown in Figure 5.

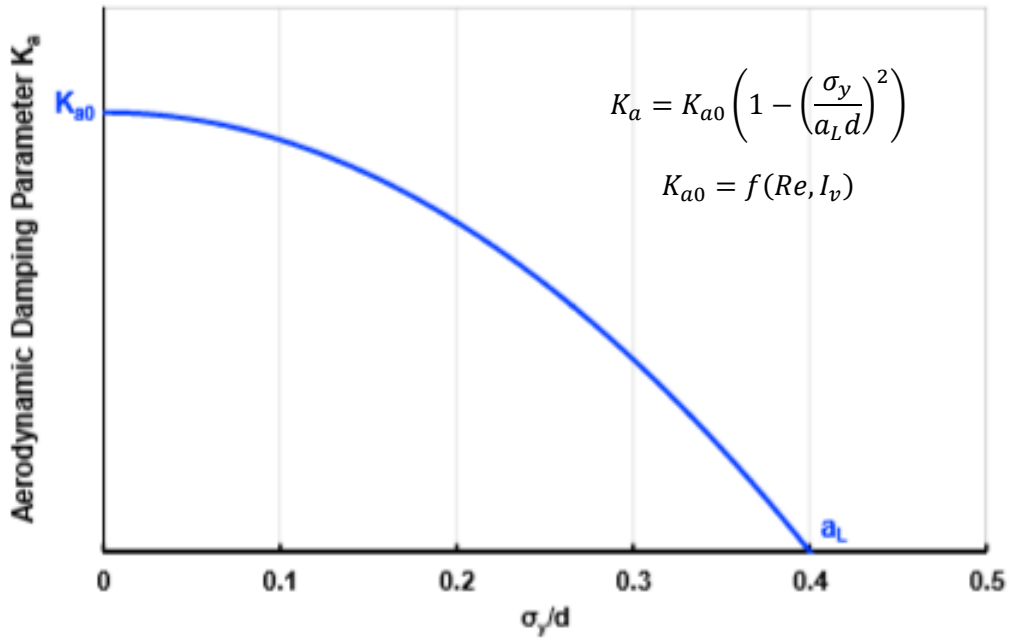

Figure 5 : Theoretical aerodynamic damping parameter K_a, resulting from the Rayleigh oscillator model (Vickery and Basu, 1983)

2.3.2 Canadian Standards

In Canada, the CSA S37 covers the design of antennas, towers and antenna-supporting structures. The Annex N, which has only become a mandatory part of the Standard in 2018, covers the dynamic effects of wind, especially instabilities due to vortex shedding. It is recommended therein to check for vortex-frequency coincidence with the natural frequencies of the first two lateral bending modes of a monopole. If so, a simplified static approach is used for a design check with additional equivalent wind forces. For a cylindrical structure, the dynamic effects of vortex shedding are approximated by applying a uniformly distributed static wind force acting over the top third of the structure perpendicular to the direction of the oncoming wind flow. This force can be calculated as:

$$F_{vs} = \frac{C_1}{\sqrt{\lambda}\sqrt{\zeta_s - \zeta_a}} q_H D_H \qquad (17)$$

where

C_1 : A constant defined in the Annex

ζ_s : The structural (mechanical) damping ratio expressed as a fraction of critical damping

λ : The aspect ratio of the structure (H/D)

ζ_a : The negative aerodynamic damping associated with vortex shedding (enter the equation with the absolute value as this damping is counteracting the effects of structural damping)

q_H : The wind pressure corresponding to the critical wind velocity at the top of the structure

D_H : The diameter averaged over the top third of the structure

In this Annex, the aerodynamic damping ratio for the fundamental sway mode can be estimated using the expression

$$\zeta_a = -C_2 \frac{\rho_a D_H^2}{m_H} \quad (18)$$

where

ρ_a : The air density

m_H : The mass per unit length averaged over the top one-third of the structure

C_2 : Constant defined in the Annex

2.3.3 EIA/TIA 222

In the United States, the EIA/TIA 222 is the reference for steel antenna towers and antenna supporting structures design. The design wind load, F_W, is found as the sum of the design wind force on the structure, F_{ST}, the design wind force on appurtenances, F_A, and the design wind force on guy wires (if present), F_G, if applicable.

$$F_W = F_{ST} + F_A + F_G \quad (19)$$

Since the structures considered in this research do not contain guys, this wind force F_G will be disregarded. The design wind force on the structure and its appurtenances are determined in a similar fashion as shown in equation (21) below.

$$F_{ST,A} = q_z G_h (EPA)_{ST,A} \quad (20)$$

where

q_z = velocity pressure

G_h = gust effect factor (1.10 for pole structures)

$(EPA)_{ST,A}$ = effective projected area

The velocity pressure, q_z, evaluated at height z is calculated by the following equation:

$$q_z = 0.613 K_z K_{zt} K_d V^2 I \quad (21)$$

where

K_z = Velocity pressure coefficient

K_{zt} = Topographic factor

K_d = Wind direction probability factor (0.95 for pole structures and appurtenances)

V = Basic wind speed for the loading condition under investigation

I = Importance factor

To account for the dynamic effects of wind gusts, different wind loading patterns are proposed to be considered for the strength limit state condition depending of the structure type. For pole structures, it is recommended to first check with full velocity pressure, q_z, applied over the entire height of the structure. Then, a lower mean velocity pressure can be applied to the different sections of the structure, as shown in Figure 6. This mean velocity pressure is obtained by multiplying the full velocity pressure, q_z, by a factor varying from 0.55 to 0.65, depending of the exposure category of the structure.

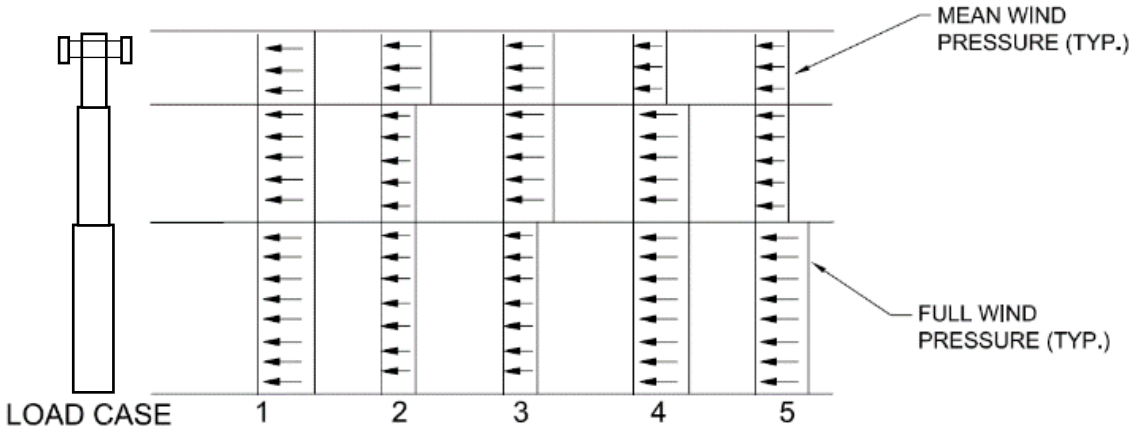

Figure 6: Wind Pattern Loading for self-supporting pole structure with three sections (TIA-222-G, 2005)

In the latest version of TIA-222-H (2018), a new Annex M for Wind-Induced Structural Oscillations has been introduced. It states that cantilevered tubular round sections used for pole structures can be subjected to significant wind induced oscillations, especially when there are minimal appurtenances supported. Vortex-shedding, buffeting and galloping are identified as the three general types of wind induced oscillations that can be observed. The Annex also mentions that the significance of oscillations depends of their amplitude, the frequency at which they occur and their duration, which may or may not lead to fatigue cracks especially at locations with openings or at abrupt changes in stiffness. It adds that no practical analytical method has been found to predict in advance if significant wind induced structural oscillations will occur at a particular site, which result from a complex combination of variables beyond the control of the manufacturer or the structure designer. Therefore, the Annex only proposes mitigation solutions if large oscillations occur, such as the installation of mass or liquid dampers, helical strakes or additional appurtenances intended to introduce turbulence in the air flow. It concludes by recommending a more frequent maintenance at sites where wind induced oscillations are known to occur to identify early signs of fatigue and mitigate its effect before possible catastrophic failure.

2.3.4 AASHTO

In the United States, the American Association of State Highway and Transportation Officials (AASHTO) procures Standard specifications for structural supports for highway signs, luminaires and traffic signals. These specifications are also widely used in Canada. In terms of wind dynamic effects, it covers the natural wind gust effects, the wind gusts caused by traffic and flutter/galloping. Vortex shedding was accounted for in the fatigue provisions of the 2009 Standard, but later removed in 2013 to only keep the aforementioned phenomena. This decision of disregarding vortex shedding came from a number of researches which concluded that flutter/galloping was attributed to be the main cause of wind-induced vibrations (NCHRP Report 494 (2003)). Nevertheless, many

other studies revealed that those vibrations came from vortex shedding and not galloping (Wieghaus, 2015). Such disparity proves that there is still no certainty about the true cause of those wind-induced vibrations on flexible structures like transportation signals and luminaires and that further development should be carried out on combinations of those effects.

The Load and Resistance Factor Design (LRFD) Specifications for Structural Supports for Highway Signs, Luminaires, and Traffic Signals, 1st Edition, 2015 with 2019 Interims is the most up to date version of this work and Section 11 covers Fatigue Design. Only the following structures need be considered for fatigue design:

- Overhead sign structures ,
- Overhead traffic signal structures, and
- High-mast lighting towers (HMLT),

The Standard recommends using an infinite life approach when designing new structures for fatigue, which should ensure that it performs satisfactorily for its design life to an acceptable level of reliability without significant fatigue damage. However, the Standard also recognizes a finite life methodology for existing structures, which necessitates an accurate assessment of the lifetime wind induced stress range histogram.

The National Cooperative Highway Research Program (NCHRP) Report 412 (1998) and NCHRP Web Only Document 176 (2011) are the basis for fatigue design provisions for cantilevered structures whereas NCHRP Report 494 (2003) is the basis for non-cantilevered support structures.

Importance categories and fatigue importance factors have been introduced in the standard after the NCHRP Reports 469 (2002) and 494 (2003). They classify the structures in accordance to their hazard in the event of failure. More recently, the NCHRP 718 (2012) also provided fatigue loads and the associated importance factors for HMLTs.

Loads

NCHRP Report 412 (1998) identified galloping, vortex shedding, natural wind gusts and truck-induced gusts as wind-loading mechanisms that can induce large-amplitude vibrations and/or fatigue damage in cantilevered structures. On the other hand, in noncantilevered structures, NCHRP 494 (2003) identified only natural wind gusts and truck-induced gusts as wind-loading mechanisms that can induce large-amplitude vibrations and/or fatigue damage.

Flutter/Galloping

Flutter/galloping is observed on structures such as sign and traffic signals with attachments to the horizontal cantilevered arm with nonsymmetrical cross-sections. This observation was confirmed in wind tunnel tests from Kaczinski et al. (1998). In order to account for the phenomenon in design, the AASHTO proposes to apply an equivalent vertical static shear force per unit area, as viewed in normal elevation, of all sign panels and/or traffic signal heads and back plates rigidly mounted to the cantilevered horizontal support. It shall be equal to the following:

$$P_G = 21\, I_F \text{ (psf)} \qquad (22)$$

where

I_F = fatigue importance factor

21 = pressure (psf)

The equivalent static vertical shear of 21 psf was determined based on wind tunnel tests and analytical calibrations. In lieu of designing to resist those galloping forces, cantilevered sign structures may use effective vibration mitigation devices based on historical or research data. Some examples are discussed in NCHRP Reports 412, 469 and 718. The device can alter the dynamic properties of the structure or the aerodynamic properties of the attachments to mitigate galloping or provide positive aerodynamic damping to alter the structure's response from aerodynamic effects on the attachments.

For example, installing a sign blank mounted horizontally and directly above the traffic signal attachment closest to the tip of the mast arm provides positive aerodynamic damping to the structure and mitigates galloping-induced vibrations (McDonald et al., 1995).

Natural wind gust

Natural wind gusts are the most obvious wind phenomena that may induce vibrations on any structure since they basically are always present. They arise from naturally occurring variability in the velocity and direction of air flow. These changes of air flow produce fluctuating pressures on the sign structure, which can cause it to vibrate. In the long term, these random vibrations may cause fatigue damage (Hajali, 2012). These repeated cycles are therefore very important in fatigue design. For both the cantilevered and noncantilivered overhead sign and traffic signal supports, AASHTO proposes an equivalent static natural wind gust pressure of:

$$P_{NW} = 5.2 C_d I_F \text{ (psf)} \qquad (23)$$

where

I_F = fatigue importance factor

5.2 = pressure (psf)

C_d = the appropriate drag coefficient based on the yearly mean wind velocity of 11.2 mph for the considered element to which the pressure range is to be applied.

The natural wind gust pressure shall be applied in the horizontal direction to the exposed area of all support structure members, signs, traffic signals and/or miscellaneous attachments. It should be considered for any direction of wind.

Truck induced gust

The high-speed passage of trucks beneath support structures may induce gust loads on attachments mounted on the horizontal support of cantilevered and noncantilevered overhead sign support structures. Loads are produced in both vertical and horizontal directions, but the horizontal support vibrations caused by forces in the vertical direction are the most critical. Therefore, AASHTO developed another empirical formula defining an equivalent static truck gust pressure to be applied in the vertical direction to the horizontal support as well as the area of all signs and attachments. It is found from:

$$P_{TG} = 18.8 C_d I_F \text{ (psf)} \qquad (24)$$

where

I_F = fatigue importance factor

18.8 = pressure (psf)

C_d = the drag coefficient based on the truck speed of 65 mph for the considered element to which the pressure range is to be applied.

This pressure shall be applied along any 12-ft length located directly above traffic lane to create the maximum stress range. Full pressure shall be applied for heights up to 20 ft, and may be linearly reduced to a value of zero at 33 ft. Another formula is presented in the Standard for lower truck speeds. However, it is clearly stated that the given truck-induced gust loading obtained with the aforementioned formula ''should be excluded unless required by the Owner for the fatigue design of overhead traffic signal structures.'' It was found that the actual response of traffic signal structures to truck-induced gusts is greatly overestimated by the design procedures proposed by AASHTO (Albert et al, 2007).

2.4 Wind Tunnel Tests

Lupi et al. (2017) have conducted wind tunnel experiments at the University of Bochum (Germany) to investigate the aerodynamic damping of a circular cylinder in vortex-induced vibrations. The data collected evidenced a behaviour of the aerodynamic

damping with positive curvature, which is in contrast with the negative curvature of the Rayleigh formulation, used in many international standards such as the Eurocode. The best fit curve on the data is shown in Figure 7 in which the symbols were previously defined in section 2.2.1.

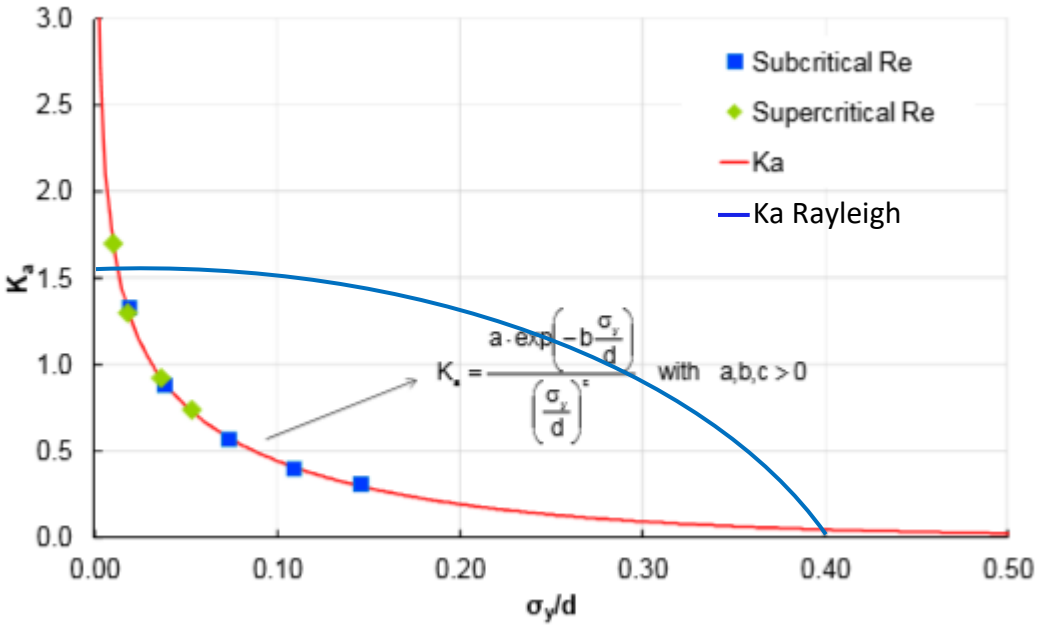

Figure 7: Aerodynamic damping parameter K_a from wind tunnel tests (Lupi et al, 2017)

The mathematical model developed exhibits a curve approaching infinity for ever smaller oscillations and tends to zero for increasingly large oscillations. In the case of the Rayleigh model, the aerodynamic damping K_a (in percentage) is represented as a negative parabola centered at zero, as seen in Figure 5 from section 2.2.1 and reported here on Figure 7. The initial value of K_{a0} may slightly vary in function of Reynolds number and turbulence intensity of the air flow, but the overall shape will remain the same. Therefore, the theoretical Rayleigh model underestimates the aeroelastic dissipation of energy for small oscillations and furthermore requires large oscillations before a significant reduction of aerodynamic damping is observed. Hence, predictions from the Eurocode and other

international standards based on Rayleigh's formulation are usually very conservative (Lupi et al., 2017).

2.5 Fatigue Resistance

Fatigue is a localized, progressive and permanent phenomenon that causes structural changes in a material subjected to repeated strains at a nominal stress that has maximum value less than the ultimate tensile strength of the material. After a number of such fluctuations, fatigue may lead to cracks and fracture. According to Boardman and Deere (1990), the process of fatigue in metals consists of the following three stages:

- Initial fatigue damage leading to crack initiation
- Crack propagation
- Final, sudden fracture of the affected cross section

Crack initiation results from the plastic strain caused by the cyclic stress. At a microscopic level, plastic strains can appear at low levels of stress. Furthermore, manufacturing procedures such as forming, treatment and welding may cause residual stresses in the material. Then, tensile stresses promote crack growth (opening mode I), and as soon as the remaining uncracked cross section becomes too weak to carry the imposed loads, fracture may occur.

A fluctuating stress is represented by two main components: a mean stress, σ_m, and an alternating stress, σ_a. The stress range, σ_r, is the difference between the maximum and minimum value of stress in a cycle.

$$\sigma_r = \sigma_{max} - \sigma_{min} \tag{25}$$

$$\sigma_a = \frac{\sigma_r}{2} = \frac{\sigma_{max} - \sigma_{min}}{2} \tag{26}$$

$$\sigma_m = \frac{\sigma_{max} + \sigma_{min}}{2} \tag{27}$$

Furthermore, the stress ratio R is frequently used in presenting fatigue data.

$$R = \frac{\sigma_{min}}{\sigma_{max}} \tag{28}$$

Most of the data available in literature treats cases of fully reversed cycles in which the mean stress is zero and the tensile stress is equal to the compressive stress, as illustrated in Figure 8a. However, cases where the mean stress σ_m is not equal to zero are frequent in practice, considering the common presence of dead loads. Figure 8b shows a case where the mean stress is in tension. Finally, the random stress cycle can be encountered when the material is subjected to random loads during service, as shown in Figure 8c.

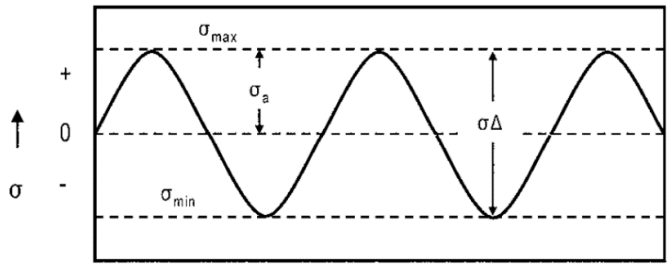

a) Fully Reversed Loading

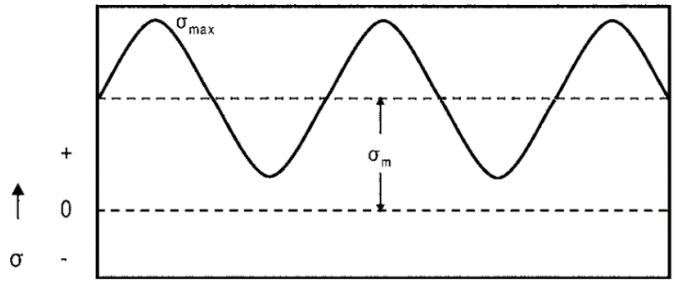

b) Tension-Tension with Applied Stress

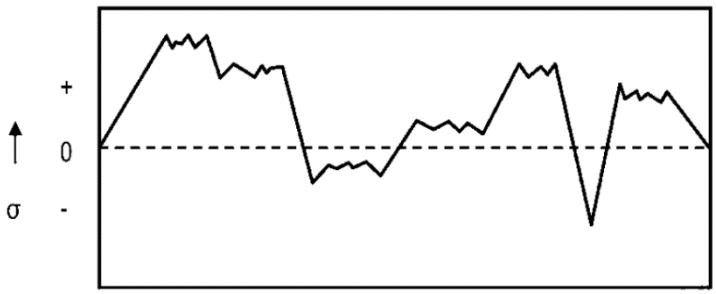

c) Random or Spectrum Loading

Figure 8: Typical loading cycles (ASM International, 2008)

Predicting the fatigue life of a material is not an easy task because materials are sensitive to manufacturing procedures, small changes in loading conditions, overall size effect, surface roughness and exposition conditions. A widespread method to estimate the fatigue life of a specified material is the use of S-N curves. They present high-cycle fatigue tests results as a plot of stress, S, versus the number of cycles to failure, N, for a large number of cycles ($N \geq 10^5$ cycles). Those curves are usually determined for a specified mean stress, σ_m, or the ratio, R. The fatigue life of a material is defined as the number of cycles to failure at a specified stress level, while the fatigue strength, sometimes referred to as the endurance limit, is defined as the stress below which fatigue failure does not occur. (ASM International, 2008).

Some materials exhibit a great endurance limit, whereas some others do not. For example, steels present an endurance limit in the range of 0.35 to 0.60, while aluminum has no endurance limit (ASM International, 2008). This implies that for any stress level, aluminum will fail after a finite number of cycles. On the other hand, for steels, if the applied cyclic stress is lower than the endurance limit of the alloy, they will withstand a theoretical infinite life.

Even though most of the fatigue data found in literature look at completely reversed bending with a mean stress of zero, as previously mentioned, mean stress effects are

important and an increase in mean stress will always cause a reduction in fatigue life, as shown in Figure 9.

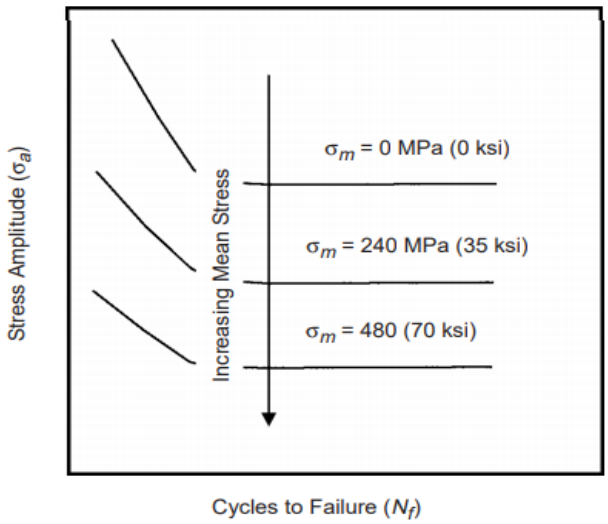

Figure 9: Effect of mean stress on fatigue life (ASM International, 2008)

The first researchers to investigate this phenomenon were Gerber (1874), Goodman (1899), Haigh (1917) and Soderberg (1930). They developed relationships to predict the effects of mean stress on stress amplitude from fully-reversed stress data as depicted in Figure 10. The Gerber parabolic curve usually gives a better estimate for ductile metals; however, because of the scatter in fatigue data, the more conservative Goodman relationship is often used in practice (ASM International, 2008).

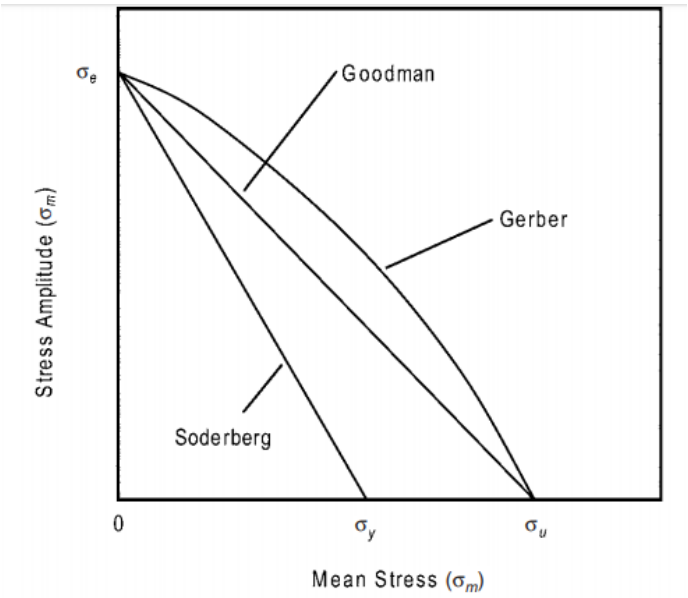

Goodman $\sigma_a = \sigma_e \left[1 - \left(\frac{\sigma_m}{\sigma_u}\right)\right]$

Soderberg $\sigma_a = \sigma_e \left[1 - \left(\frac{\sigma_m}{\sigma_y}\right)\right]$

Gerber $\sigma_a = \sigma_e \left[1 - \left(\frac{\sigma_m}{\sigma_u}\right)^2\right]$

where

σ_e = Fatigue strength for N cycles under zero mean stress
σ_a = Fatigue strength for N cycles under mean stress of σ_m
σ_u = Ultimate tensile strength
σ_y = Yield strength

Figure 10: Comparison of Goodman, Gerber and Soderberg models for relating mean stress to stress amplitude

Many researches have been done to evaluate the fatigue life of cantilevered sign structures (Johns and Dexter (1998), Dexter and Ricker (2002), Li et al. (2005), Kacin et al. (2010), Ding et al. (2016)), which led designers to stiffer designs privileging steel over aluminum due to its greater fatigue resistance.

As for monopole towers, much less data are available, and they are generally a product of computer simulations. Kumar et al. (2017) have looked into the structural behaviour of monopoles and self-supporting telecommunication towers under different wind speeds. They analysed tower heights of 30 m, 40 m and 50 m under winds of 33 m/s, 47 m/s and 55 m/s using the STAAD(X) Tower software (2019). They observed lateral displacements up to 6 times greater for monopoles in opposition to self-supporting towers. They concluded that during higher wind speed events, the lower stiffness of monopoles may lead to damages necessiting repairs. Giaccu and Caracoglia (2018) have developed a novel numerical algorithm for the simulation of along-wind dynamic response of slender towers under turbulent winds using a Stochastic Approximation Monte Carlo algorithm. Their proposed methodology estimates structural fragility curves under extreme wind loads. The objective of a fragility analysis is to determine the conditional probability of exceedance of representative limit states through the assessment of indicators, such as maximum lateral drift of the tower. After 10000 samples of wind loads applied, they did not get a probability of exceedance of the maximum lateral drift of the tower of more than 1%. However, fatigue was not taken into account.

3. Analysis of Monopole Structures

3.1 Modeling

Two existing telecommunications monopoles (designated as M1 and M2) were modeled for analysis. As indicated in Table 1, M1 is composed of two different circular cross-section diameters to reach a total height of 29.7 meters whereas M2 uses three different circular cross-section diameters to reach a total height of 38.1 meters. The technical drawings provided are presented in Figure 11 and a photograph of the actual structure can be seen on Figure 29 in section 3.4.

Table 1: Telecommunications monopole dimensions

Steel Monopole	Section	Height (m)	Diameter (mm)	Thickness (mm)
M1	1	15	610	7.9
	2	14.7	457	7.9
M2	1	12.8	914	8
	2	12.8	762	8
	3	12.5	610	6

The towers were analysed using commercial software ADINA 9.4.3. Shell elements were used for the masts with steel linear properties reported in Table 2. The antennas, also modelled with 9-nodes shell elements to capture wind effects, are attached to the masts with rigid beams. However, the antennas have been initially given a high rigidity for simplicity which can be easily modified if needed in further analysis. Details regarding antennas are listed in Table 3. The connections at cross-sectional changes are assumed to be fully rigid. The masts are assumed to be fixed at the base, on rigid foundation. Finally,

point masses of 8.5 kg have been added every 1,5 meters along the height of the monopoles to account for the attached ladder.

Table 2: Steel properties

Modulus of Elasticity, E (MPa)	**Density (kg/m^3)**	**Poisson's ratio**
200000	7800	0.3

Table 3: Antenna Specifications

Tower	**Antenna model**	**Number of units**	**Dimensions (mm)**	**Weight (kg)**	**Installation radius (m)**
M1	A1	6	2058 x 262 x 149	29	1
M2	A2	12	1302 x 155 x 69	7.5	2.5

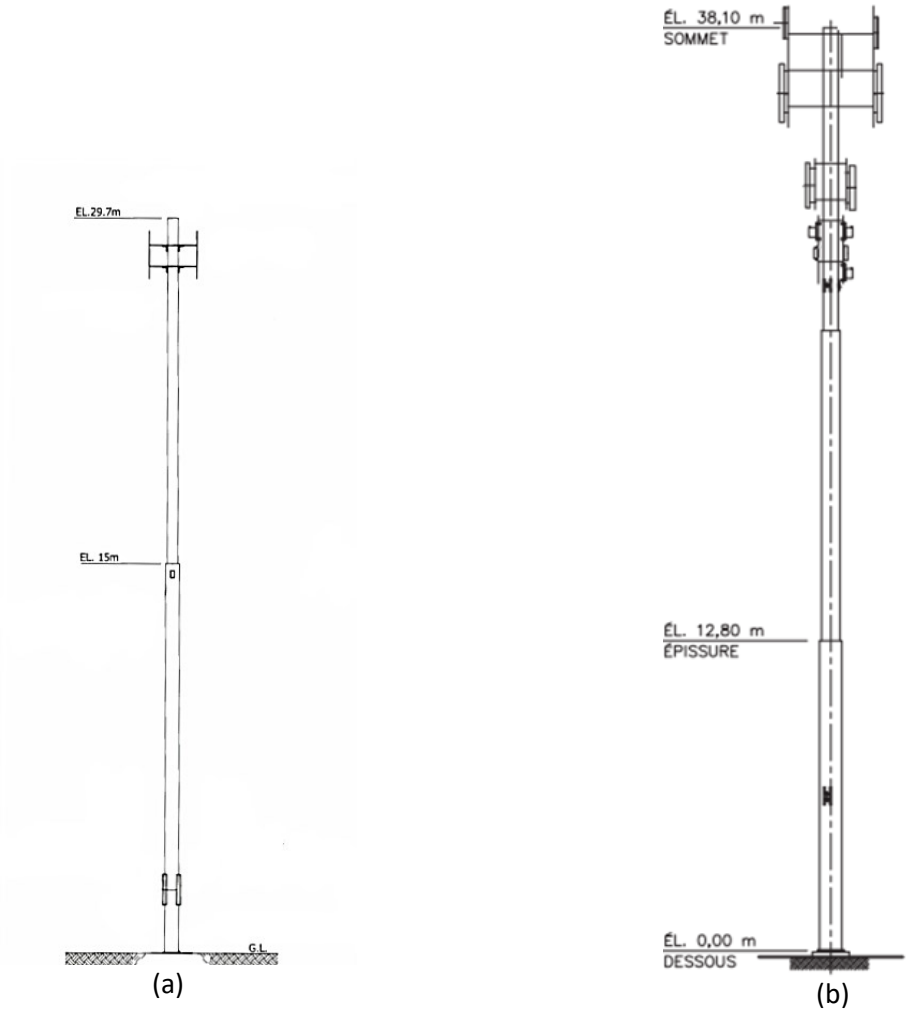

Figure 11: Industry drawings for (a) Monopole M1 and (b) Monopole M2

The resulting finite element models have more than 3000 9-nodes shell elements with realistic antenna layouts. Figure 12 features elevation views of the two models.

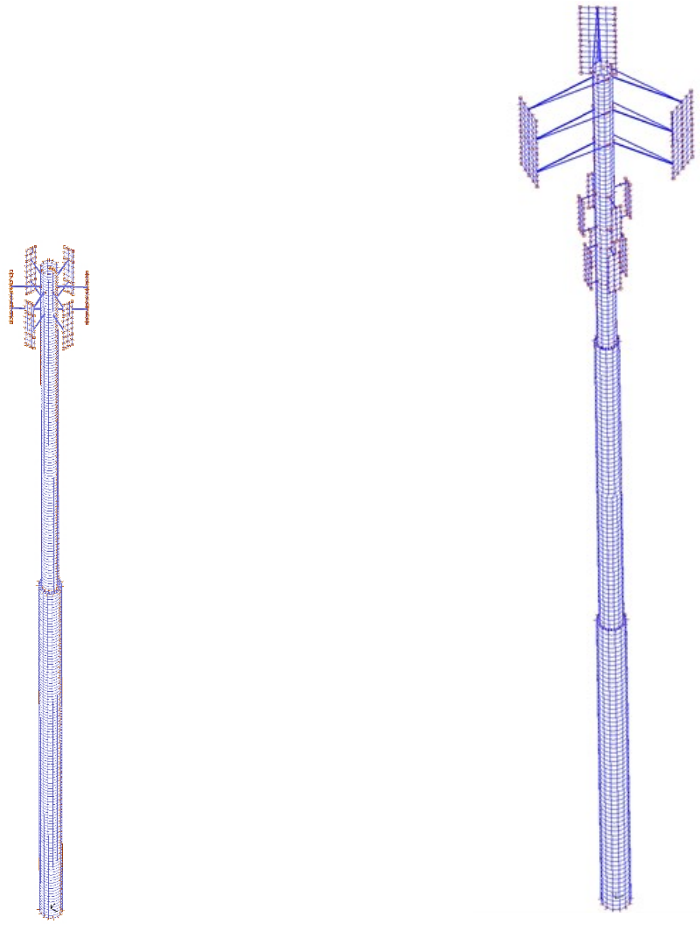

(a) (b)

Figure 12: Elevation views of Finite Element Models of (a) Monopole M1 and (b) Monopole M2

3.2 Eigenvalue analysis

With completed models, the eigenvalue analysis yielding the natural frequencies and mode shapes can be undertaken using ADINA, which utilizes the Subspace Iteration Method (Bathe, 1996) searching for modal frequencies within a specified range. In this case, the range was chosen to be under 50 Hz since wind does not contain a considerable amount of energy at higher frequencies. ADINA outputs the frequencies as well as a depiction of the corresponding mode shapes. In the analysis, it was found that the three

lowest frequency modes were sufficient to catch the probable frequencies to be excited by wind. The illustration of the three lowest-frequency mode shapes of each tower can be seen in Figures 13 and 14 with their corresponding natural frequencies.

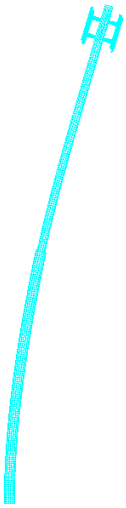

Mode 1 : 0,81 Hz

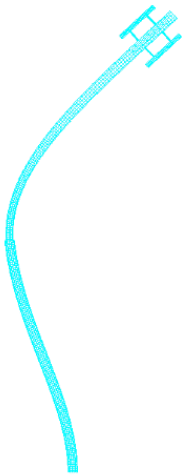

Mode 2 : 3,61 Hz

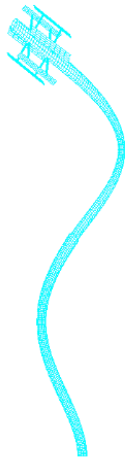

Mode 3 : 10,50 Hz

Figure 13: Natural Frequencies of Tower M1

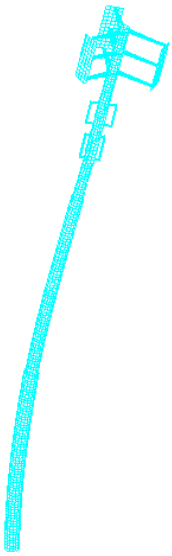

Mode 1 : 0,40 Hz

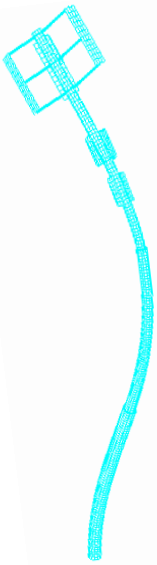

Mode 2 : 2,32 Hz

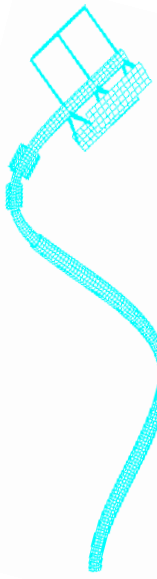

Mode 3 : 5,56 Hz

Figure 14: Natural Frequencies of Tower M2

To validate the accuracy of these frequency values, two 2-D beam models with the same dimensions of the 3-D shell models were created. The values obtained with those beam elements were within 2% of the ones obtained with the detailed models. However, the use of detailed models is privileged since they can accurately take wind loads as pressures whereas beams need an idealized line load. Furthermore, in the optic of future research, these detailed models can be re-used for more detailed wind-structure interaction analysis.

In addition to the beam models, Ambient Vibration Measurements (AVM) were taken on site for Tower M2. All the results are presented and discussed in section 3.4 where the main outcome was that the numerical model is about 10% stiffer than the real structure. Therefore, by using equation 34 of the same section, the model was adjusted using a modified modulus of elasticity to match the measured values of natural frequencies. In the absence of data for Tower M1, a similar adjustment of 10% was assumed to add flexibility in the model. Thus, the modified models were used for all the following wind analysis.

3.3 Load application

3.3.1 Static load

The static wind load calculations were carried out on both monopoles in accordance with CAN/CSA S37-18. In the calculation, antennas and other attachments were not taken into account for simplification. For pole structures, the wind load was determined as follows:

$$W = qC_eC_gC_aC_dA_s \tag{29}$$

where

q = the reference velocity pressure,

C_e = the height factor,

C_g = the gust effect factor,

C_a = the speed-up factor,

C_d = the drag factor,

A_s = the net projected area exposed to wind.

The values of q can be obtained from Appendix C of the National Building Code of Canada for the site. Alternatively, they can be approximated from Figure 15.

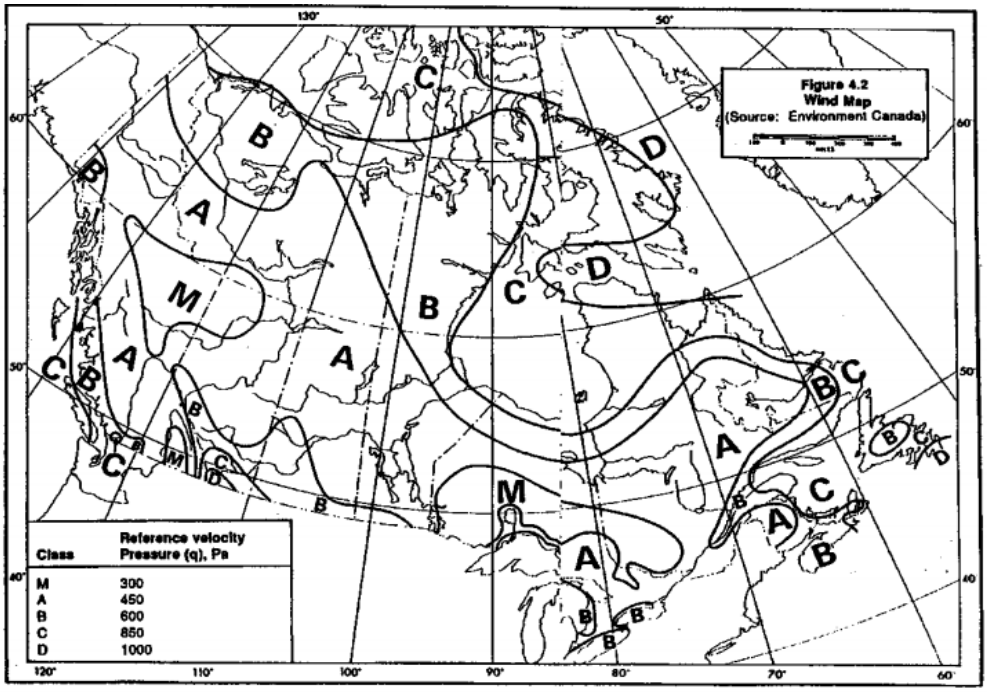

Figure 15: Wind Map for Canada (Source : NBC 2015).

For both structures, q = 370 Pa.

In the analysis for pole structures, we have used the following factors:

C_g = 1.0

$$C_e = \left(\frac{H_x}{10}\right)^{0.2} \qquad 0.9 \leq C_e \leq 2.0 \qquad (30)$$

$C_a = 1.0$

$C_d = 1.2$

where H_x is the height in meters above grade.

$$q_{wg} = \sqrt{\frac{0.005}{\zeta_s}} \frac{q_{10}}{2} \quad (31)$$

where

q_{wg} = Natural wind gust pressure

q_{10} = 10-year return period mean hourly wind pressure at 10 m above ground,

ζ_s = structural damping ratio, use 0.3% (0.003) when no experimental values available.

The total static wind pressure profile applied to the monopoles is shown in Figure 16.

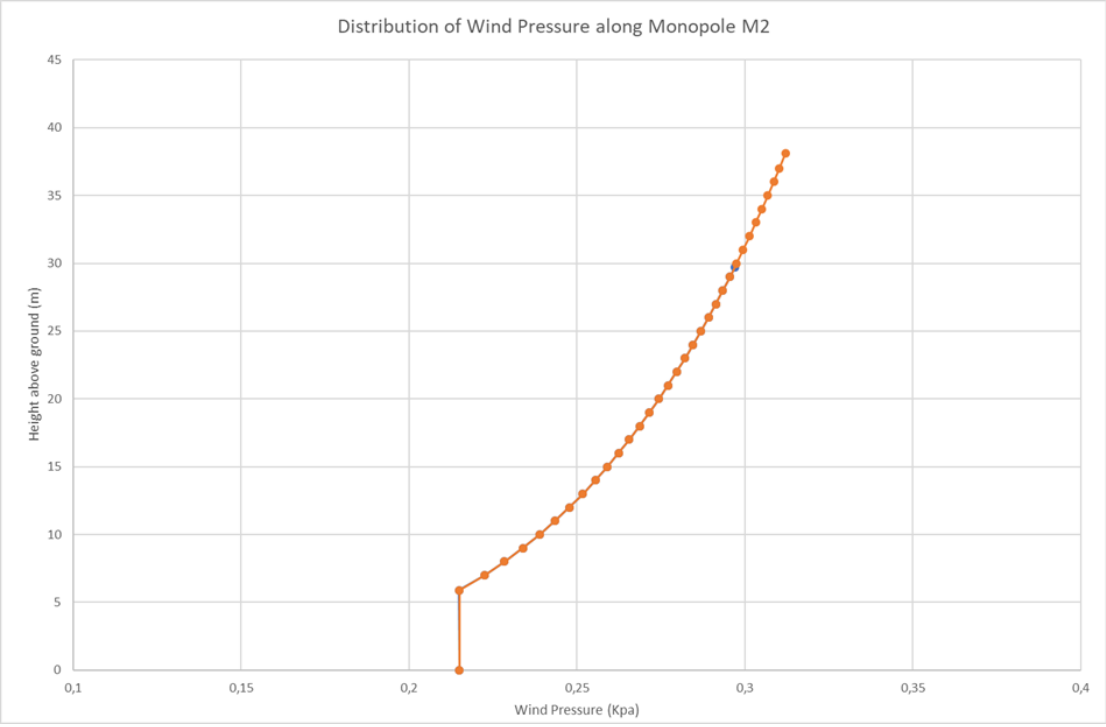

Figure 16: Total static wind pressure applied to Monopoles M1 and M2

These static wind pressures were then applied to the models in ADINA Statics to determine the maximum horizontal displacements at the top of the masts, summarized in Table 4.

Table 4: Maximum Displacement of the Monopoles under Static Wind Pressure

Monopole	**Static Displacement at top (m)**
M1	0.099
M2	0.111

These values represent respectively 0.35% and 0.29% of the M1 and M2 total heights. Once again, the amplitude of displacement for both monopoles was verified using the previously mentioned 2-D beam models and there was agreement.

3.3.2 Periodic load

The periodic load is of interest since it may trigger dynamic amplifications if tuned with the natural frequencies of the monopoles. The periodic load is modeled as a sinusoidal function with different turbulence intensities to mimic the effects of repeated wind gusts on the structure and its response in the along-wind direction. Each sinusoidal function is defined such that its maximum value corresponds to the static wind load defined in section 3.3.1, as depicted in Figure 17 and 18 for tower M1. Since the natural frequencies are known from the previous frequency/mode analysis for both towers, the sinusoidal functions will be developed such that the natural frequencies will be triggered, and resonance or quasi-resonance will be observed. Tower M1's natural frequencies are 0.80 Hz and 3.60 Hz for the first two modes, corresponding to periods of approximately 1.25 s and 0.28 s respectively. Similarly, for tower M2, the first two natural frequencies are at a magnitude of 0.36 Hz and 2.10 Hz, leading to periods of 2.80 s and 0.48 s.

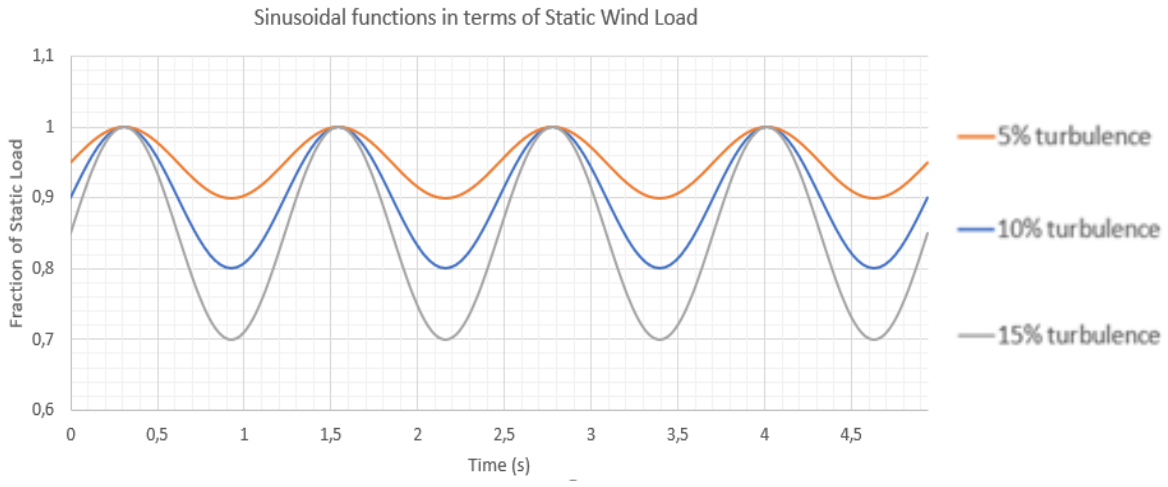

Figure 17: Sinusoidal Functions for M1's first mode in terms of Static Wind Load

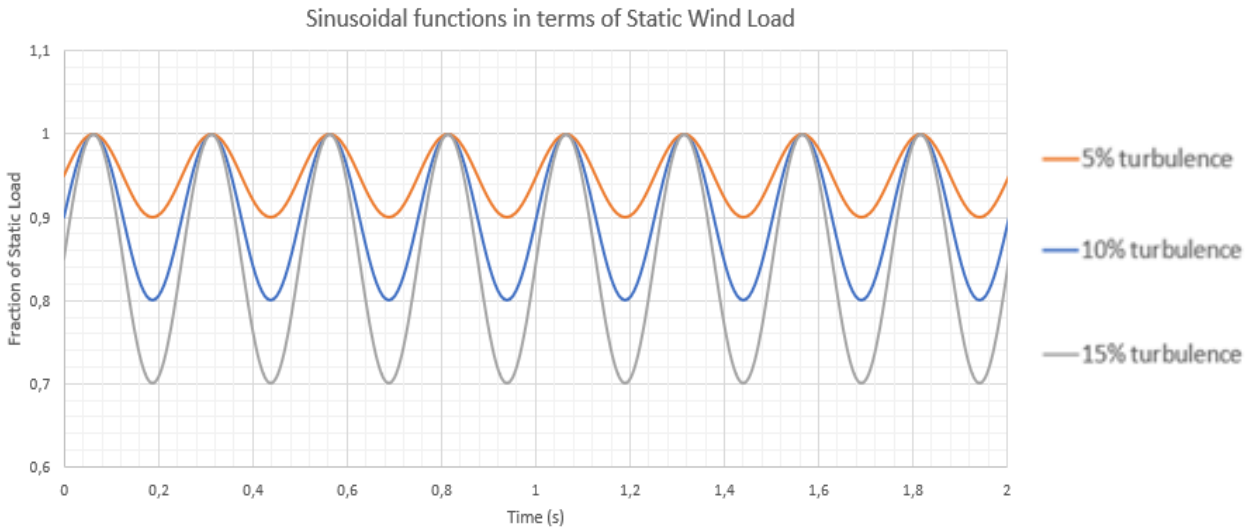

Figure 18: Sinusoidal Functions for M1's second mode in terms of Static Wind Load

These periodic functions are then applied to the Static wind load profile to produce a varying intensity wind and therefore trigger dynamic response in the structures. The resulting time histories of tip displacements for tuning with the first mode for towers M1 and M2 are reported in Figures 19 and 20. Similarly, the resulting time histories for tuning with the second mode of the towers are presented in Figures 21 and 22.

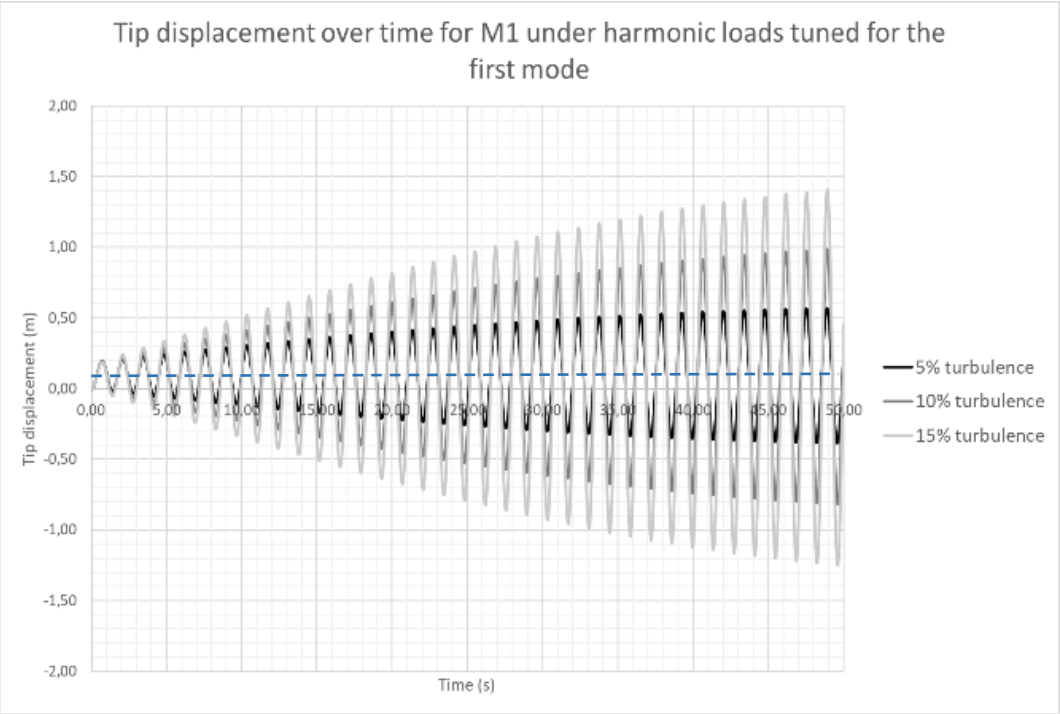

Figure 19: Tip displacement of M1 under harmonic loads of the first mode of different turbulence intensities

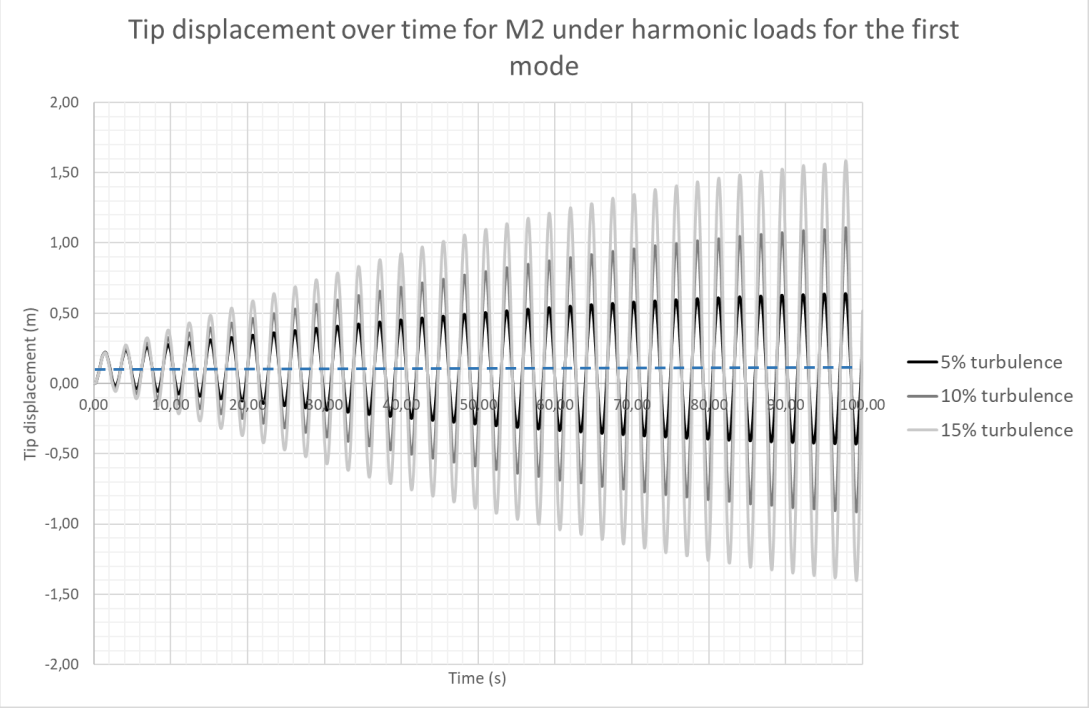

Figure 20: Tip displacement of M2 under harmonic loads of the first mode of different turbulence intensities

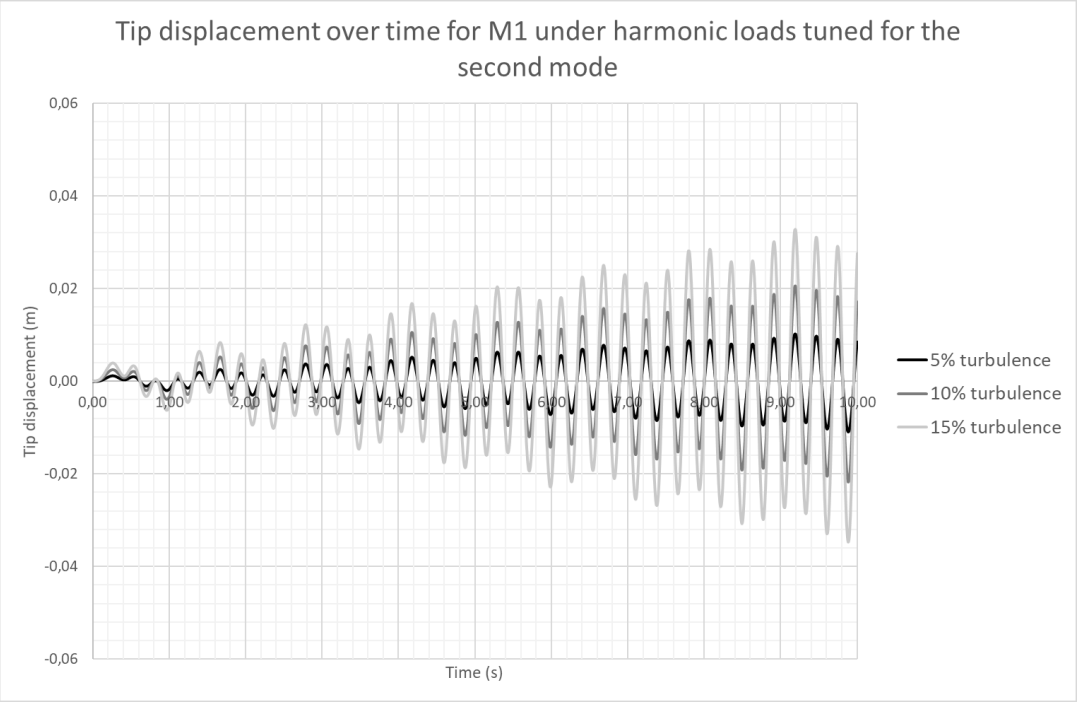

Figure 21: Tip displacement of M1 under harmonic loads of the second mode of different turbulence intensities

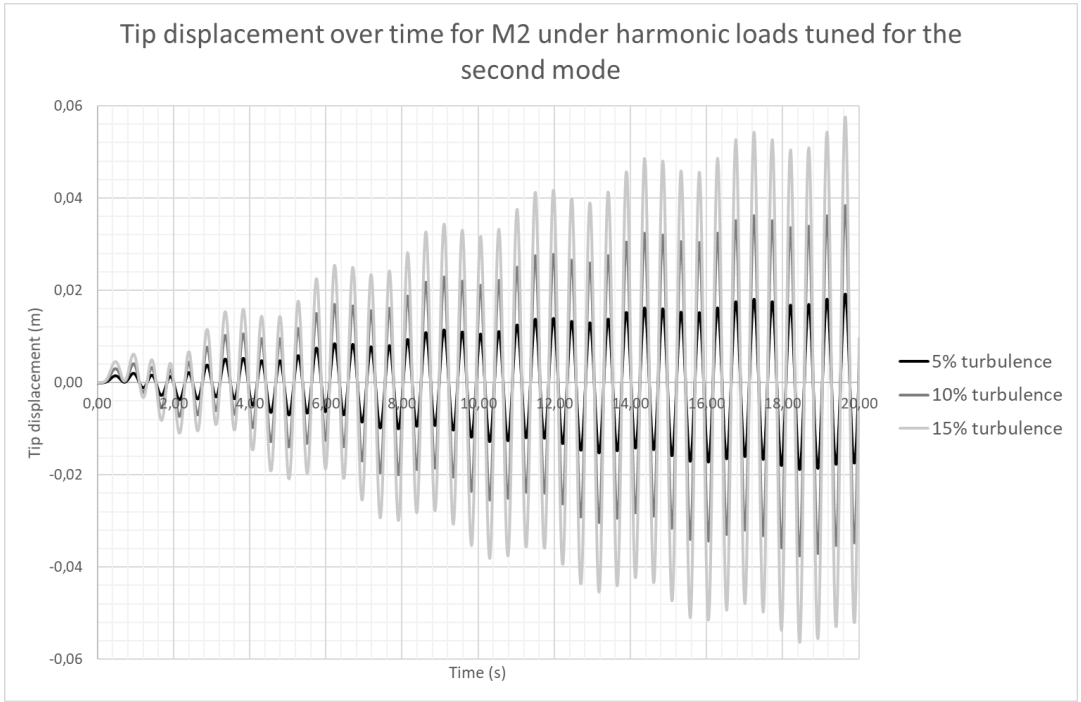

Figure 22: Tip displacement of M2 under harmonic loads of the second mode of different turbulence intensities

The tip displacement time history tuned for the first mode of vibration spans 50 seconds for tower M1 and 100 seconds for tower M2, resulting in a similar number of displacement cycles. Resonance is reached since the displacement keeps growing with time for both structures. The mean value of displacement is shown with a dashed line. As expected, the displacement is greater with growing turbulence intensity. Under 15% turbulence intensity, tower M1 reaches a displacement of approximately 1.40 m after 36 cycles whereas tower M2 reaches nearly 1.60 m. These values represent a value of more than 14 times greater than their respective maximum static displacement, which is only equal to 0.099 m and 0.111 m for tower M1 and M2, respectively, as presented in the previous section 3.3.1. Clearly, under a perfectly harmonic resonance scenario, and assuming a linear elastic response of the structure, both towers will demonstrate much higher vibration amplitudes than expected during design using the equavalent static load. At any given number of cycles, for both towers, the maximum tip displacement seems to follow a linear relationship in terms of turbulence intensity. In other words, the difference of maximum displacement between 5% and 10% turbulence intensities appears to be the same as the difference between 10% and 15%, at a given time. Therefore, it would be possible to predict the maximum tip displacement of both towers under resonance after a specific time elapsed in perfect resonance at any wind turbulence intensity. For instance, for tower M2 after 100 seconds of resonance, considering that all 3 profiles have the same mean value of x, as shown with a dashed line, and adding a value y which corresponds to the increased amplitude for each additional 5% turbulence, it can be written that:

$$0.60 = x + y$$

$$1.10 = x + 2y$$

$$1.60 = x + 3y$$

Solving this simple set of equations yields a value of 0.1 m for the mean x and of 0.5 m for each additional 5% turbulence y. Therefore, an estimate of the maximum tip displacement after 100 s for any turbulence intensity with a maximum value equal to the

maximum static wind load for this particular structure can be made using the following formula:

$$d_{max} = x + 0.1t_i \qquad (32)$$

where

d_{max} = Maximum tip displacement in a pure harmonic case

t_i = Turbulence intensity of the periodic function

x = Mean value of displacement

Thus, this formula allows to theoretically predict the maximum tip displacement after 100 s of tower M2 under a perfectly harmonic load of any turbulence intensity assuming elastic deformation. Table 5 presents the value for a turbulence intensity up to 50% with the same mean value of 0.1 m.

Table 5: Tip displacement of Tower M2 under perfectly harmonic wind loads of different turbulence intensities

Turbulence intensity (%)	**Maximum tip displacement (m)**
5	0.6
10	1.1
15	1.6
20	2.1
25	2.6
30	3.1
35	3.6
40	4.1
45	4.6
50	5.1

Once again, these values are purely theoritical assuming a perfectly linear elastic response of the structure under large displacement analysis, which would not be the case with such high displacement values in reality. However, it illustrates that under a perfectly harmonic load, these monopoles can exhibit large displacements.

With sinusoidal functions tuned for the second mode of both structures, the response is different. The time history spans 10 seconds for tower M1 and 20 seconds for tower M2. Resonance in the second mode is reached once again in both cases after approximately 5 cycles of adjustment. However, the presence of the fundamental mode of vibration is displayed by some lower frequency signature present in all 3 responses of both monopoles. After more than 30 cycles, both towers display a maximum tip displacement lower than the maximum static displacement, with a value of only 0.03 m for tower M1 and 0.06 m for tower M2. Once again, there seems to be a linear relationship between displacement and turbulence intensity that will not be developed in this case due to smaller displacements.

3.3.3 Random load

Once the models have been verified to respond correctly to static and harmonic wind loads, random wind loads can be applied. Those random wind load profiles are generated using a random number generator algorithm within a specified range of amplitude and time. The generated profiles were then plotted and inspected to ensure that their frequency content correspond to the frequency content of naturally occurring wind. 100 profiles with different characteristics were chosen to cover most part of the natural wind spectrum and to generate different model responses. The controlled variables were the mean amplitude of the wind history, its turbulence intensity and frequency content.

Firstly, 10 random wind histories were generated for each 10% step of the maximum static load. In other words, 10 profiles were generated with a mean value of 10% of the maximum static load, 10 different profiles were generated with a mean value of 20% of the maximum static load, and so on. Secondly, within each group of 10 random wind

profiles, 5 of them were given a turbulence intensity of 10%, while the other 5 were given a turbulence intensity of 20%. The objective of such methodology is to observe the effect of changing a variable with others being held constant and therefore evaluate the importance of each one individually and conjointly.

Before undertaking the analysis of the behavior of both monopoles under the 100 random wind profiles, the adequacy of the frequency content of these profiles must be verified, using the Davenport theoretical wind spectrum for boundary layer natural wind (Davenport, 1961) as a reference. By applying a Fast Fourier Transform to all the generated random wind time histories, individual wind spectra are obtained and normalized with respect to their maximum value. They can then be superimposed and compared to the Davenport wind spectrum. The result is shown in Figure 23 with 5 individual wind spectra, named r1.1 to r1.5.

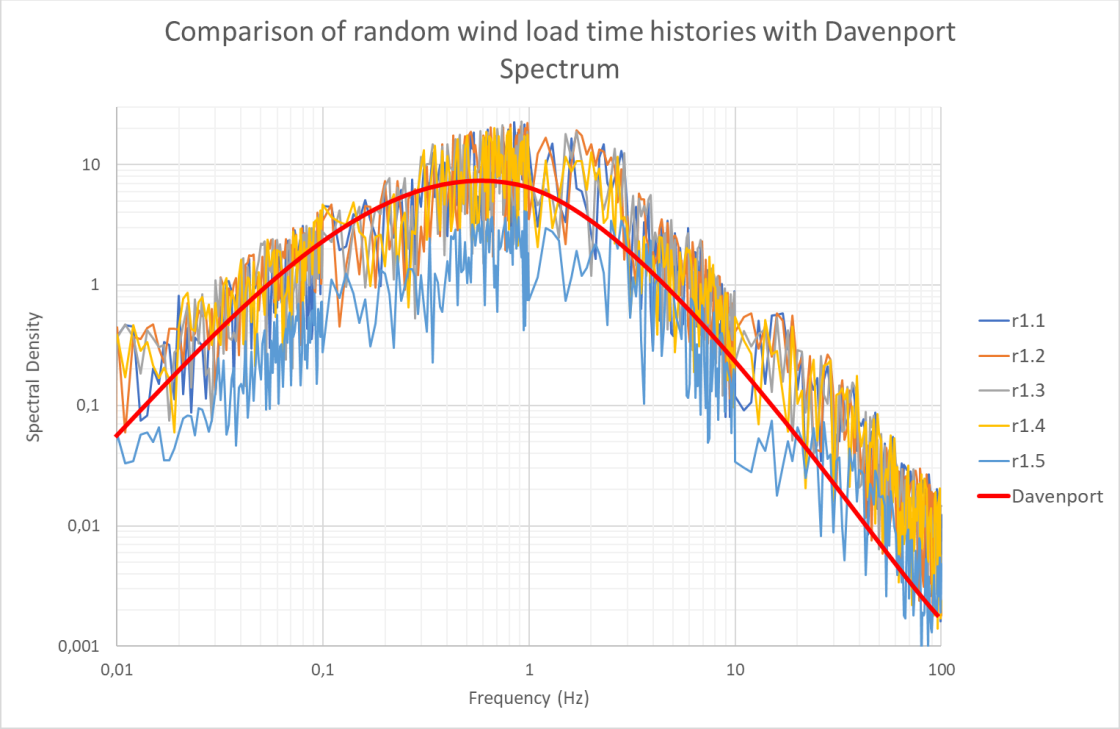

Figure 23: Comparison of Randomly generated wind spectra and theoretical Davenport Spectrum for boundary layer wind

With only five random wind time histories, the theoretical Davenport wind spectrum is contained by the envelope of minimum and maximum value for more than 96% of the frequency range. In locations where it is not contained, it does not differ by more than 8% from the envelope. Ten other random wind time histories have been checked and displayed similar frequency content as the theoretical Davenport wind spectrum. In the extent of this research, the results were deemed to be appropriate. Therefore, the 100 dynamic analyses for each monopole can be undertaken using ADINA's linear Dynamic Analysis Tools. Each tip displacement time history was calculated with a time step of 0.01 s to accurately identify the response of the structures. For practical purposes, the time histories must be limited in duration in the extent of this research. A 4.8 s duration has been selected for tower M1 and a 10 s duration has been selected for M2, which gives approximately the same number of cycles of fundamental period of vibratrion for both towers. All the resulting displacement histories are presented in Annex A.

We first discuss the results for the 10 random wind profiles at 10% of the maximum static load on M1 as depicted in Figure 24. The first five profiles (r1.1 to r1.5) have a turbulence intensity of 10% whereas the last five (1.6 to 1.10) have a turbulence intensity of 20%. The first observation is that turbulence intensity does not increase the displacement automatically by itself, even though all these profiles display different frequency content: The five profiles with higher turbulence intensity do not yield larger displacements than the profiles with lower turbulence intensity. Secondly, it can be observed that some profiles only trigger the fundamental mode of vibration of the monopole, such as r1.5, whereas others contain some higher modes of vibration in the response, as in the analysis of case 1.7. However, the fundamental mode of vibration is still dominant. Such different responses can be explained by looking at the frequency content of the concerned wind profiles, as shown in Figure 25. As expected, the random profile 1.5 displays a small peak around and below 1.0 Hz, which coincides with the fundamental frequency of the tower, whereas 1.7 has two peaks around 3.0 and 4.0 Hz, which now corresponds to the second mode of vibration of the tower. Therefore, the frequency content of the applied wind has a certain influence on the dynamic response of the structure at low mean wind speeds.

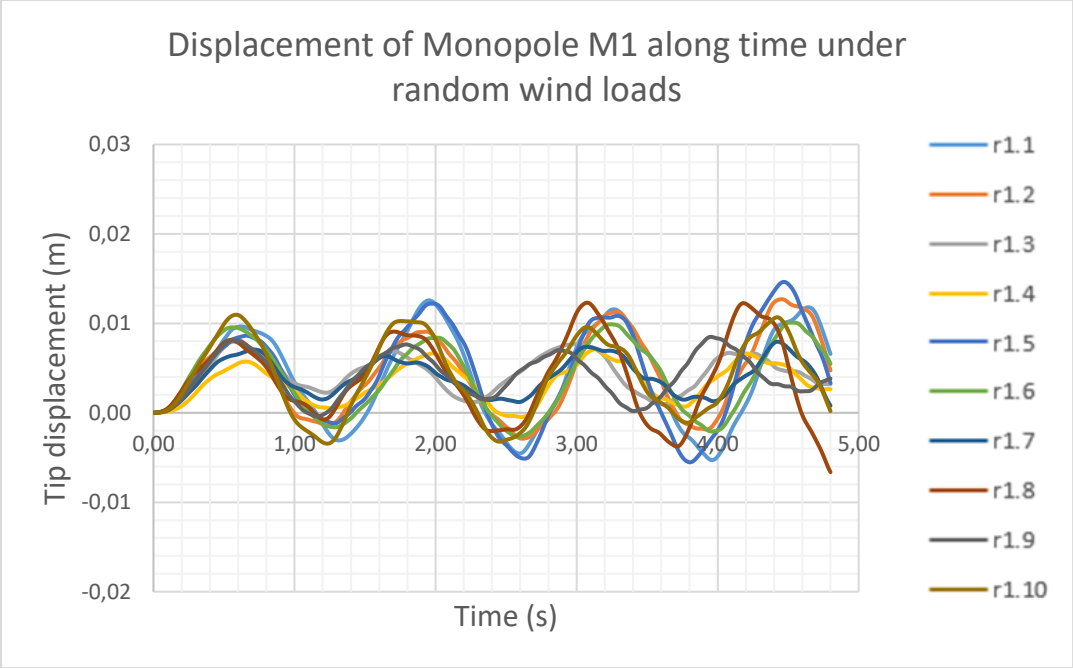

Figure 24: Tip Displacement of M1 under random wind loads of 10% of maximum static load

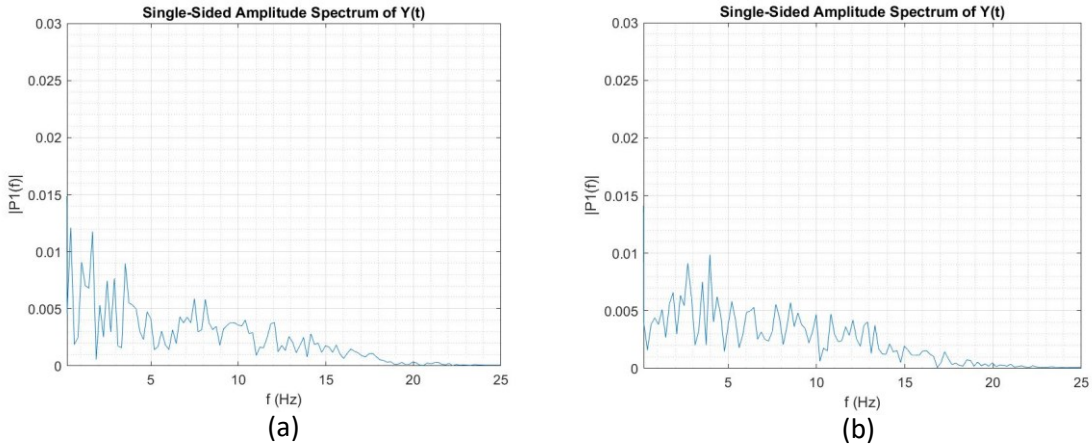

Figure 25: Frequency content of synthetic wind profile (a) r1.5 and (b) r1.7

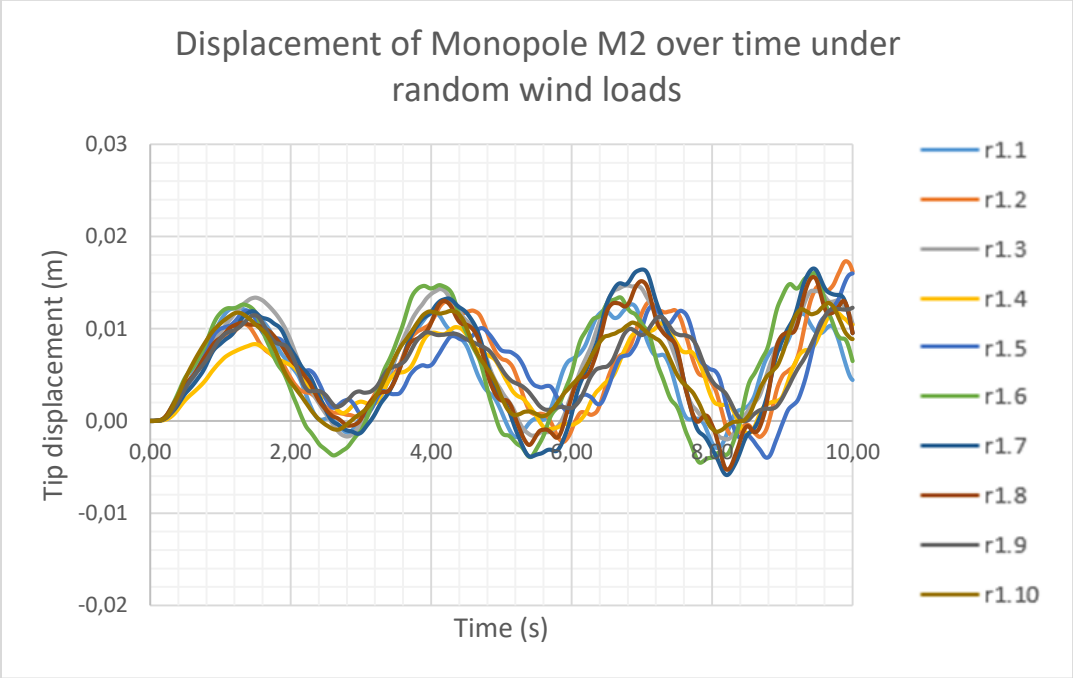

Figure 26: Tip Displacement of Tower M2 under random wind loads of 10% of maximum static load

The same random wind profiles were applied to monopole M2, and the results for the mean wind pressure equal to 10% of the static wind load are reported in Figure 26. Once again, similar observations as for M1 can be made due to the relative closeness of the tower's frequencies present in the spectra of 1.5 and 1.7. It can be noticed that the maximum tip displacement reached by tower M1 and M2 is of 1.5 cm and 1.7 cm respectively. The average displacement value for both towers falls short of 1 cm, which is just under the 10% value of maximum static displacement presented in section 3.3.1. Once again, the fundamental mode of vibration seems to be dominant for that structure in its reponse under random wind loads.

Now looking at profiles with greater mean wind values, such as 80% of the maximum static load, the results are different than at lower amplitudes for both towers M1 and M2, as depicted in Figures 27 and 28, respectively. The resulting tip displacements are much smoother, practically displaying solely the fundamental mode in a stable harmonic response. In this analysis scenario, the first five random wind profiles (r8.1 to r8.5) have a 10% turbulence intensity while the last five random wind profiles (r8.6 to r8.10) have a

20% turbulence intensity. However, higher turbulence intensity does not automatically imply a greater displacement. Also, now that the mean value approaches the maximum static load, the influence of frequency content of the wind history appears to be fairly diminished in comparison to lower mean value loads. Figure 29 shows the frequency content of profiles 8.4 and 8.10, which respectively display a concentration of frequencies around 1.0 Hz and 3.0 Hz, corresponding to close values of the first two modes of vibration of the structures. However, these differences do not clearly appear on the resulting displacement curves that remain mostly influenced by the structures' fundamental mode, due to the distributed mass of the structure. Since there is a concentration of mass on top of both monopoles due to the presence of antennas, the fundamental mode is expected to be dominant in the response, approaching a single degree of freedom system. However, the total antenna mass does not exceed 4.8% of the total mass for M1 and 6.1% for M2. Therefore, the continuous behaviour of the pole remains dominant and still responds with a dominant fundamental mode. The displacement reaches slightly above 10 cm for the 29.7 m M1 while it nearly reaches 14 cm for the 38.1 m M2, which represents a 25% dynamic amplification from an equivalent 80% static load for M1 and a 27% dynamic amplification for M2.

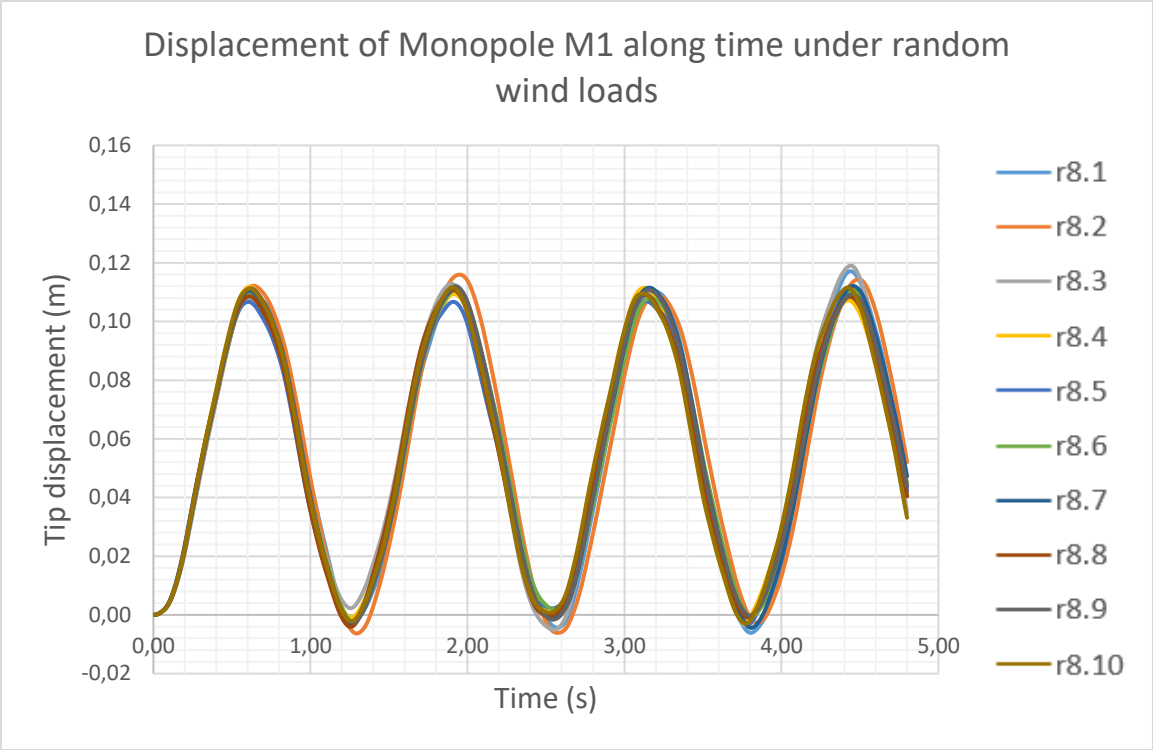

Figure 27: Tip Displacement of Tower M1 under random wind loads of 80% of maximum static load

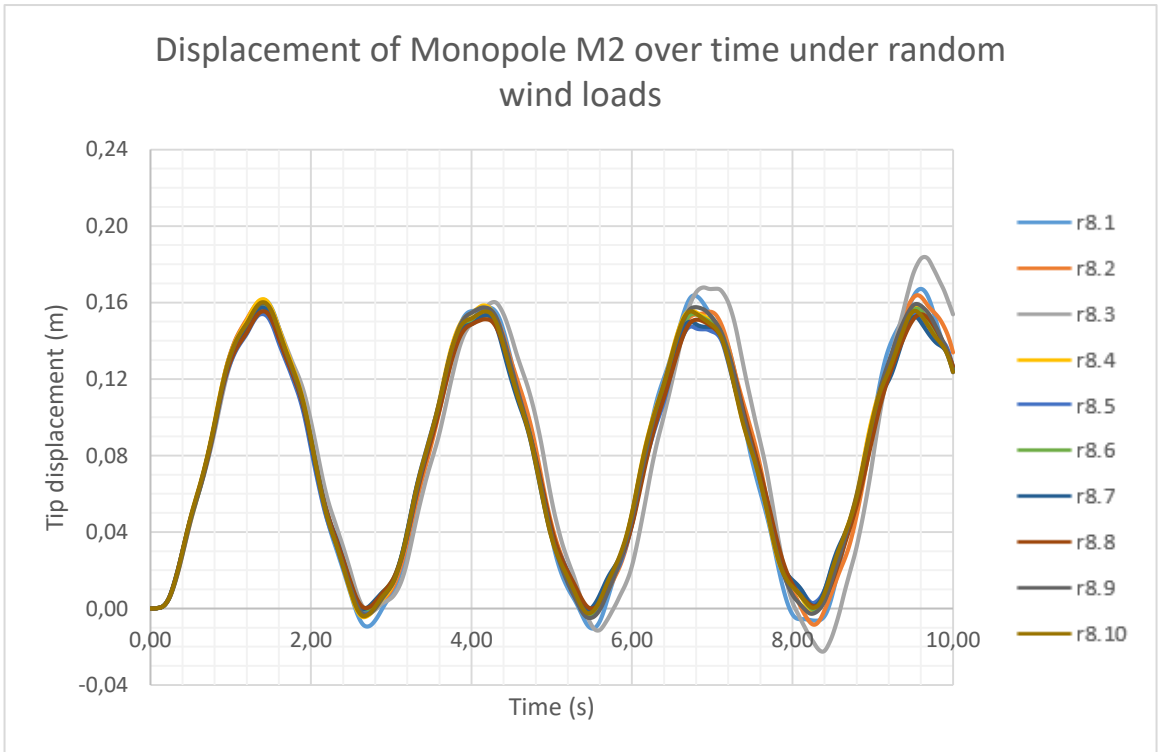

Figure 28: Tip Displacement of Tower M2 under random wind loads of 80% of maximum static load

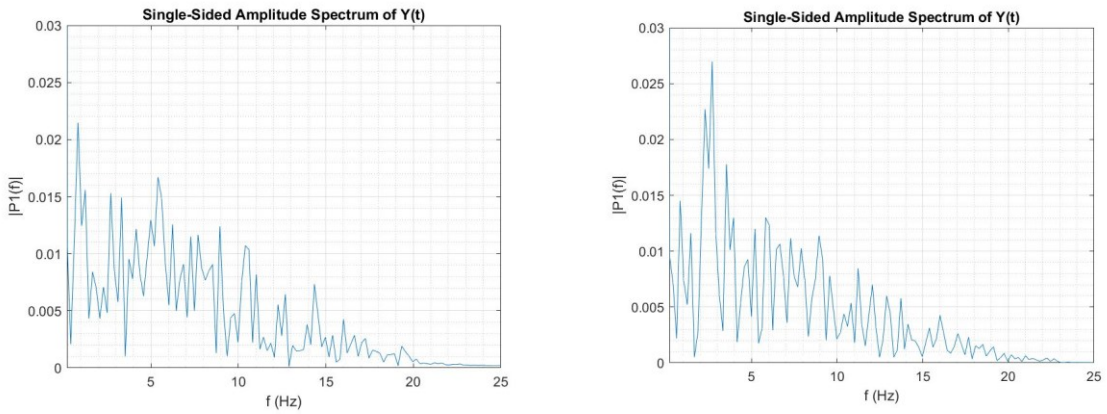

(a) (b)

Figure 29: Frequency content of profile (a) r8.4 and (b) r8.10

As the mean load value keeps increasing towards 100% of the maximum static load, the response keeps getting smoother and the maximum displacement increases to reach approximately 15 cm for M1 and 22 cm for M2. These values represent an increase from the maximum equivalent static load of 51% for M1 and 98% for M2. In CAN/CSA-S37 (2018), the basic gust factor suggested is 2.0, which shows to be conservative for tower M1 and satisfactory for M2. However, Annex N suggests the use of a gust factor of 1.0 to assess the response of pole structures to static and fluctuating wind components for the fatigue/vortex shedding calculation only, which would yield unconservative force and displacement results for both monopoles.

Figure 30 shows the response of monopole M2 under the 90% random wind profiles superimposed to a corresponding amplitude harmonic load with 10% turbulence intensity which induces resonance in the structure. It can be observed that the displacement amplitude does not grow as significantly in the random wind case as it does in the perfectly harmonic case when the structure reaches resonance. However, some other random wind profiles with frequencies mostly around the fundamental frequency may exhibit a resonance-like response in the structure with growing displacement amplitude

and longer periods. As such, the pure harmonic case will remain a theoretical limiting case in terms of force and displacement in the structure.

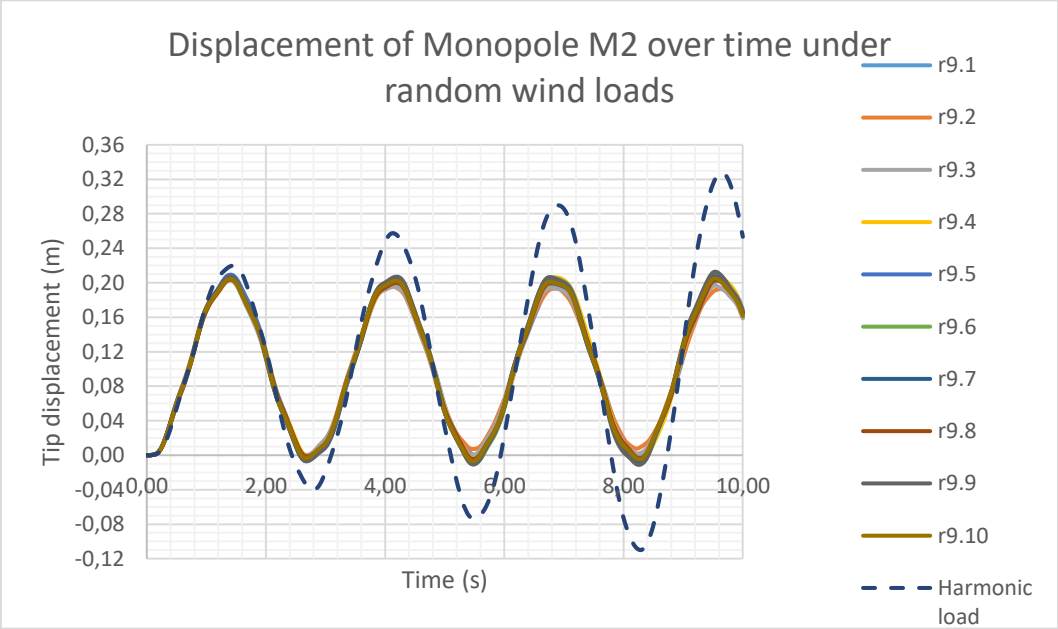

Figure 30: Comparison of response to pure harmonic load on M2

The maximum tip displacement is not the only result of interest in the analysis. In terms of fatigue design, it is important to quantify the number and amplitude of reversed loading cycles that a structure may undergo in its life span. What is observed here is that the amplitude of displacement in the direction opposed to the wind does not necessarily grow with a growing mean wind amplitude. Therefore, stronger winds may not be critical for fatigue design of telecommunication towers, with the exception of resonance.

3.4 Field data

In order to validate the numerical model previously built with ADINA, field measurements on the actual structure must be taken. With the collaboration of the owner, it was possible to acquire data on monopole M2 in-situ, as shown in Figure 31. Two Tromino 3G ENGY velocimeters (2002) were used to measure the velocity of the structure to an accuracy of 10e-6 m/s (µm/s). Two 30-minute tests were conducted with a different configuration of the instruments for each test, as illustrated in Figure 32. In configuration

1, one instrument was strapped to the monopole to a height of 90 cm while the other was placed on its foundation. In configuration 2, the strapped instrument was raised to a height of 200 cm on the monopole whereas the second one was left on the concrete foundation. Those two setups were chosen for their ease to be made from the ground and to identify if a small change in height would affect the gathered data.

Figure 31: General view of Tower M2

(a) (b)

Figure 32: Data acquisition (a) configuration 1 and (b) configuration 2.

During both tests, the wind speed was observed in 3-minutes intervals using an EXTECH Mini Thermo-Anemometer 45158. Results of mean wind speed, maximum wind speed and minimum wind speed over 3-minute periods are reported in Table 6 for both configurations.

Table 6: Wind speed data measured for each test configuration

Configuration 1	m/s	km/h	**Configuration 2**	m/s	km/h
Mean Wind Speed	2,45	8,81	Mean Wind Speed	3,02	10,88
Max. Wind Speed	3,99	14,35	Max. Wind Speed	5,25	18,89
Min. Wind Speed	0,62	2,22	Min. Wind Speed	1,26	4,54

The test was conducted at 7:00 am on June 11th 2019 at a temperature of 18°C with cloudy sky. The rain had stopped just prior to the tests.

Once the in-situ data acquisition is completed, results can be extracted to the ARTeMIS Modal Standard Software (SVS, 2019). This software allows the identification of the modal frequencies of the structure using the Enhanced Frequency Domain Decomposition (EFDD) method (Jacobsen et al., 2006) as well as the approximate structural damping for the first mode. Both the natural frequencies and damping values are reported as a mean value with corresponding standard deviation. For each configuration, the sample size (n) considered is 5 records of 6 minutes each (for a total of 30 minutes) for the sensor strapped to the monopole and 15 for the one on the foundation. Thus, by combining both configurations, 10 samples are considered on the monopole whereas 30 samples are considered on the foundation, for a total of 40 samples all positions combined.

After extraction of the results for Monopole M2, the three lowest-frequency modes could be clearly identified. The following tables present the values extracted from the records taken on the foundation and on the monopole separately (Tables 7 and 8) and then all combined (Table 9).

Table 7: Frequencies obtained with the captors on the foundation (n=30)

Natural Frequencies (Hz), f					
Mode 1		Mode 2		Mode 3	
Mean	Std. Deviation	Mean	Std. Deviation	Mean	Std. Deviation
0,358	0,005	2,14	0,03	5,04	0,07

Table 8: Frequencies obtained with the captors on the monopole (n=10)

Natural Frequencies (Hz), f					
Mode 1		Mode 2		Mode 3	
Mean	Std. Deviation	Mean	Std. Deviation	Mean	Std. Deviation
0,357	0,006	2,11	0,02	4,94	0,01

Table 9: Frequencies obtained with the captors on all positions (n=40)

Natural Frequencies (Hz), f					
Mode 1		Mode 2		Mode 3	
Mean	Std. Deviation	Mean	Std. Deviation	Mean	Std. Deviation
0,358	0,005	2,13	0,03	5,02	0,07

Meanwhile, damping values are extracted although only included for the first mode only due to uncertainties in the evaluation of higher mode shapes limited by the sensor set-ups. Values for the whole 30 minutes record are presented with the same format in Tables 10 to 11.

Table 10: Damping obtained with the captors on the foundation (n=30)

Damping (%)	
Mode 1	
Mean	Std. Deviation
2,15	0,77

Table 11: Damping obtained with the captors on the monopole (n=10)

Damping (%)	
Mode 1	
Mean	Std. Deviation
2,08	0,58

In brief, the natural frequency and damping values can be summarized as follows:

The mean values of the first 3 natural frequencies of the monopole based on the 40 samples are:

Mode 1: 0.36 ± 0.01 Hz

Mode 2: 2.13 ± 0.03 Hz

Mode 3: 5.02 ± 0.08 Hz

The mean value of damping based only on the monopole samples is:

Mode 1: 2.1 ± 0.6 %

As those in-situ values are compared to the numerical model values previously determined, it can be noticed that the model is about 10% stiffer than its real-life structure. Such disparity was expected and can be explained by a number a factors, such as the fact that the numerical model is perfectly fixed at the base and at its connections, which is not the case in practice. The foundation always has a certain flexibility just like the bolted connections which are not perfectly rigid either. Furthermore, the ground composition, temperature and water content can all influence its rigidity. Finally, material defects and fabrication and construction tolerances can also lead to disparities between the model and the structure.

In order to account for these small differences between the model and reality, calibration of the model is required. Many techniques are available to achieve this purpose, such as manually introducing stiffnesses at the base and at the connections to avoid perfectly rigid connections and tuning those stiffnesses until the model matches reality. However, a much simpler technique consists in reducing the Modulus of Elasticity of steel to reduce the overall stiffness of the monopole and therefore reach the same objective. Thus, this straight forward technique was selected. From dynamics principles, it is known that for a single-degree-of-freedom system:

$$f = \frac{\omega}{2\pi} = \frac{\sqrt{\frac{k}{m}}}{2\pi} = \frac{\sqrt{\frac{f(E)}{m}}}{2\pi} \qquad (33)$$

Where

f = The natural frequency of the structure (Hz)

ω = The angular frequency of the structure (Hz)

k = The stiffness of the structure (N/m)

m = The mass of the structure (kg)

E = The modulus of elasticity of the structure (N/m^2).

Assuming that the second moment of area and length of the structure is constant for M2, the stiffness only becomes a function of E. Furthermore, keeping the mass as constant, the frequency only becomes function of the square root of E. Therefore, the adjustment of the modulus of elasticity E can be made as follows:

$$E_{adj} = E_i \left(\frac{f_m}{f_n}\right)^2 \qquad (34)$$

Where

E_{adj} = The adjusted Modulus of Elasticity (N/m^2)

E_i = The initial Modulus of Elasticity (N/m^2)

f_m = The natural frequency measured in-situ (Hz)

f_n = The natural frequency initially found with the computer model (Hz)

With this simple formula, the numerical model can be quickly adjusted to correspond to the measured natural frequencies of the monopole. All the numerical values presented in section 3 have been obtained with a modified model according to equation 34 to render a better estimate of the real response of the monopole under wind loads.

3.5 Fatigue Considerations

In order to determine the vulnerability of each monopole to fatigue, the random wind load time history which caused the greatest displacement for each structure was selected. In both cases, the selected scenario had a mean value of 100% of the maximum static wind load. Fatigue is characterised as a number of cycles at a given stress amplitude, therefore the stress amplitude must be found. ADINA can display both the stress and strain throughout the structure. Thus, for both critical random cases, the maximum stress amplitude at the base of the monopole was found accordingly. Superimposing those stress values to the G40.21 350W Steel SN Curve as shown in Figure 33, the following result is observed.

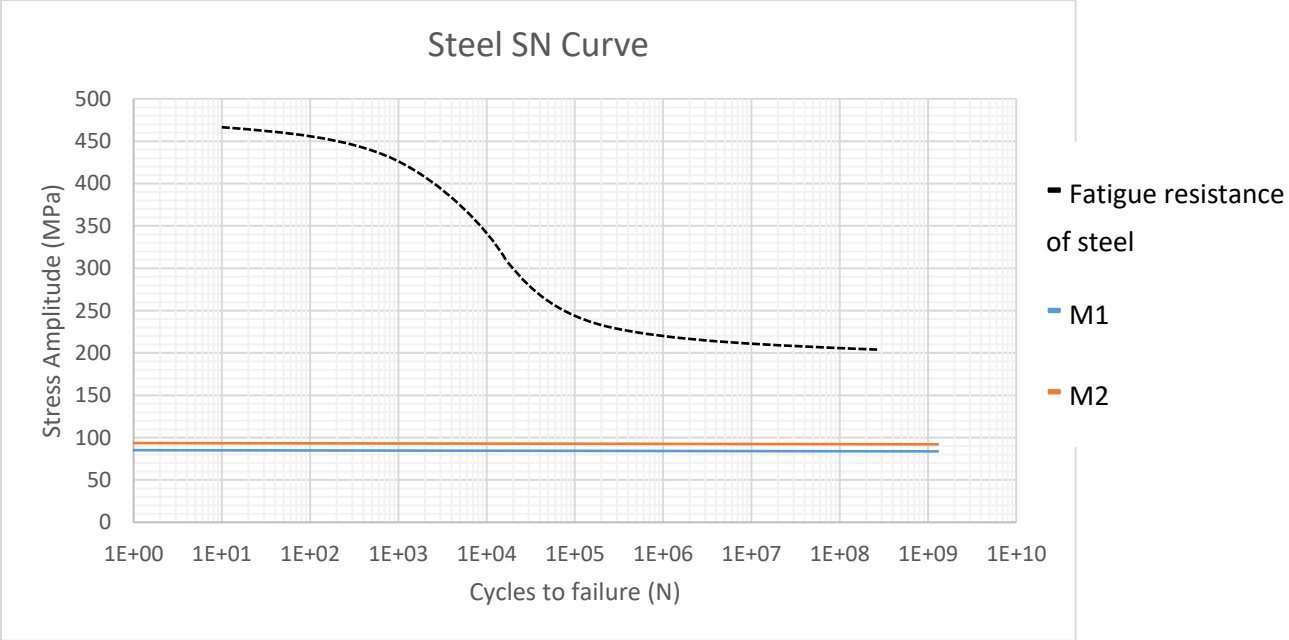

Figure 33: Comparison of fatigue resistance of steel with maximum stress amplitude of M1 and M2

Clearly, under normal conditions of random wind loads, both monopoles are far from suffering any fatigue damages after 10^8 cycles with a maximum stress amplitude less than half of the endurance limit of steel. Therefore, under normal environmental conditions,

excluding high resonance phenomena and extreme icing conditions, both monopoles will not be affected by fatigue according to the S-N method.

4. Sign Structure

4.1 Modeling

One cantilevered sign structure on the Ministry of Transportation of Quebec's (MTQ) network was used for modelling. This particular structure is a recent design for MTQ and pending confirmation of good performance, it might become a new standard for many similar ones installed on overpasses. It was designed with the intention to build a very robust structure that does no suffer from fatigue damage in its expected lifespan. As shown in Figure 34, its design is an inverted L cantilever. The vertical support component is slightly tapered and reaches a height of 5.2 m whereas the horizontal cantilevered beam is joined to the vertical support at an angle of 91.5 degrees. The detailed dimensions are listed in Table 12.

Table 12: Dimensions of the Cantilevered Sign Structure

Structure	Section	Length (m)	Base 1 (mm)	Base 2 (mm)	Thickness (mm)
S1	Vertical	5.20	930 x 540	550 x 540	9.5
	Horizontal	3.96	550 x 500	550 x 392	9.5

The structure was modeled using ADINA 9.4.3 9-node thin shell elements for the whole structure, as shown in Figure 35. Note that the sign panel is made out of aluminum whereas the main structure is made out of steel. The panel was assumed to be rigid (this can be adjusted in future work when looking at wind-structure interactions). The material properties are reported in Table 13. Details regarding the panel are listed in Table 14. Finally, the overall structure has been imposed boundary conditions of perfect fixity at its base. In reality, the structure is standing on an elevated highway section, which is more

flexible than the total fixity assumption. This consideration will be discussed in the following section when we compare eigenvalue analysis results with the measured dynamic properties.

Table 13: Material properties

Material	**Modulus of Elasticity, E (MPa)**	**Density (kg/m^3)**	**Poisson's ratio**
Steel	200000	7800	0.3

Table 14: Panel dimensions

Panel	**Material**	**Number of units**	**Dimensions (mm)**
P1	Aluminum	1	2743 x 2000 x 3

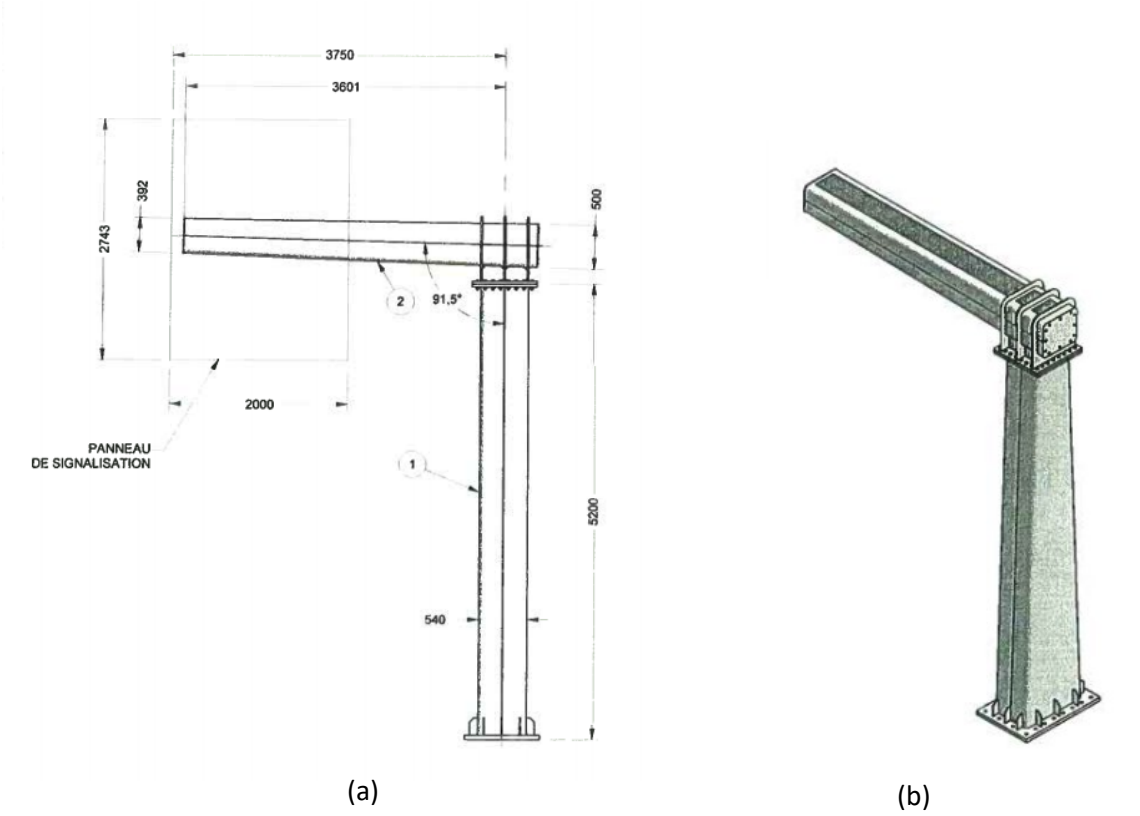

Figure 34: Drawings of the (a) elevation view and (b) 3-D view of the cantilevered sign structure

The resulting model has more than 3070 9-nodes shell elements with realistic configuration to mimic the existing structure as accurately as possible for eventual more in-depth analysis of wind-structure interaction effects (out of scope in this work). The optimal meshing density of the model has been determined with the asymptotic convergence of natural frequencies, which will be presented in section 4.2. Figure 35 features an elevation view of the finite element mesh as well as a close-up of the connection between the vertical and horizontal tubular components.

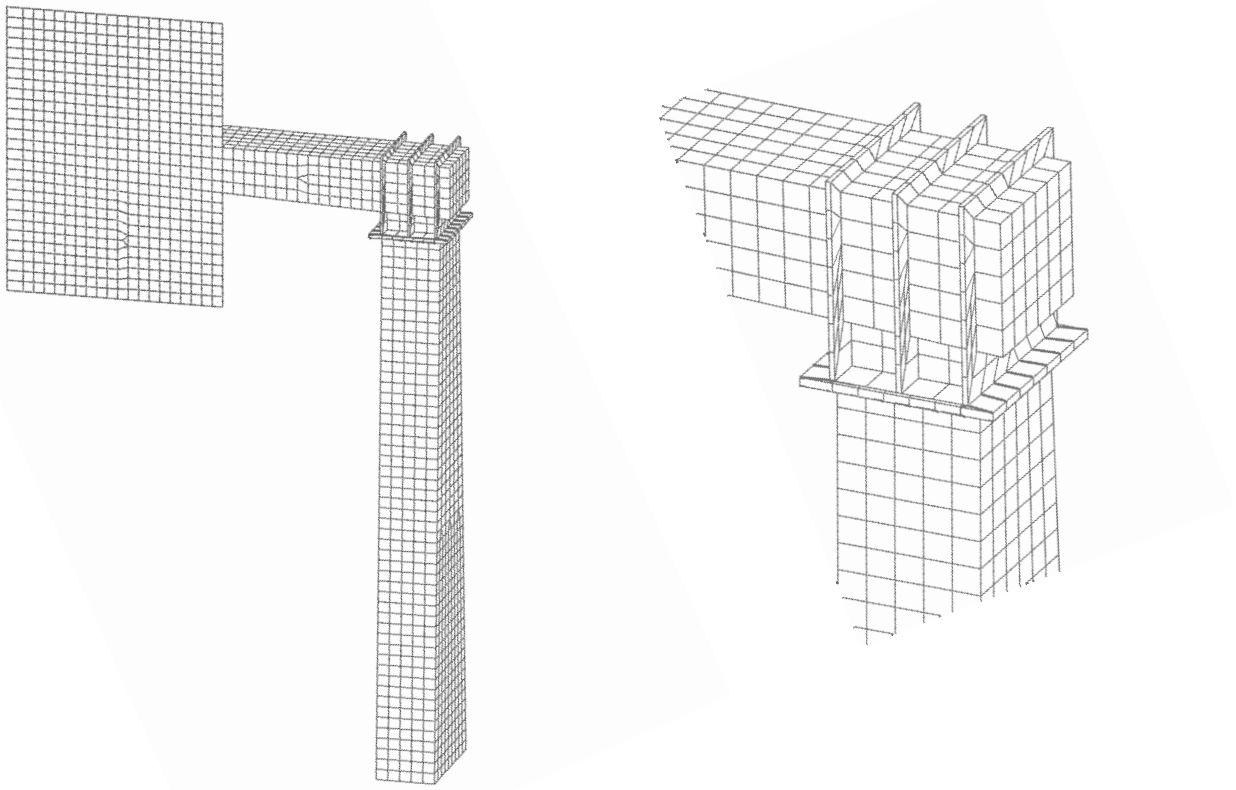

(a) (b)

Figure 35: Elevation view of (a) The overall sign structure and (b) The detailed beam-column connection

4.2 Eigenvalue analysis

With the completed model, the eigenvalue analysis can be undertaken with ADINA using the Subspace Iteration Method for a frequency range of under 50 Hz. Four modes of vibration were retained and analysed, as shown in Figure 36. Frequency values for each of the corresponding modes are reported in the same Figure with corresponding elevation, plan, and isometric views.

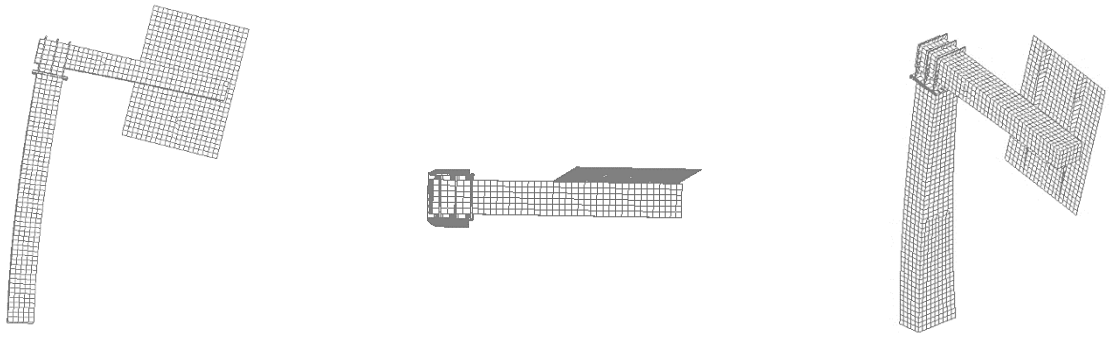

a) Mode 1 : 8,50 Hz Transverse (in-plane) bending of the column

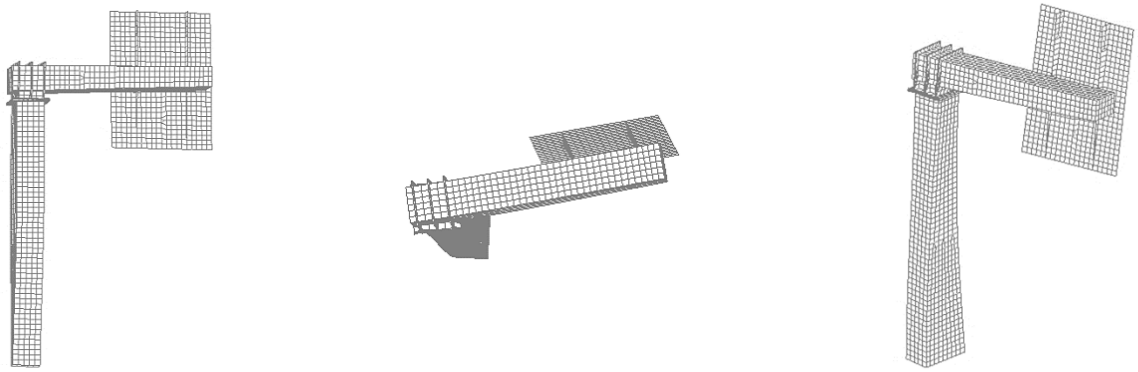

b) Mode 2 : 10,70 Hz Lateral (out-of-plane) bending of the cantilever beam with column torsion

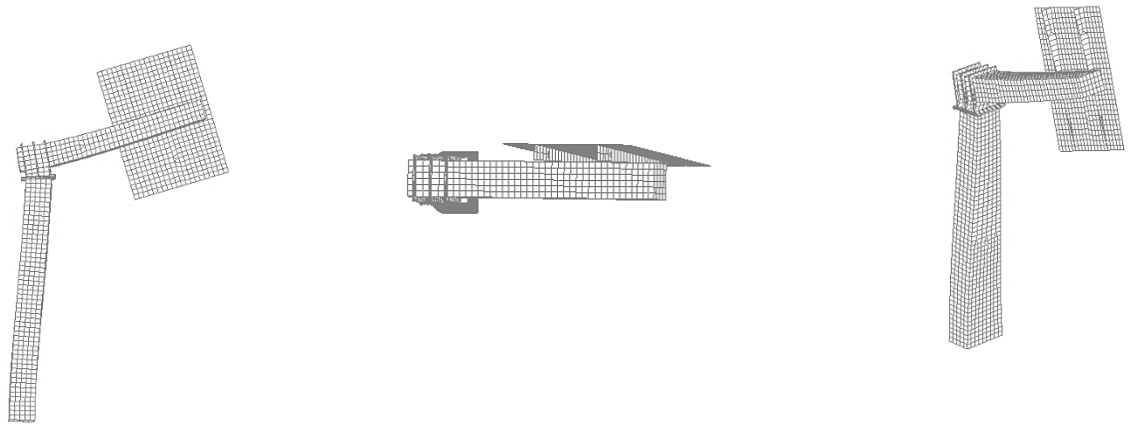

c) Mode 3 : 22,40 Hz Combined transverse (in-plane) bending of both the column and the cantilever

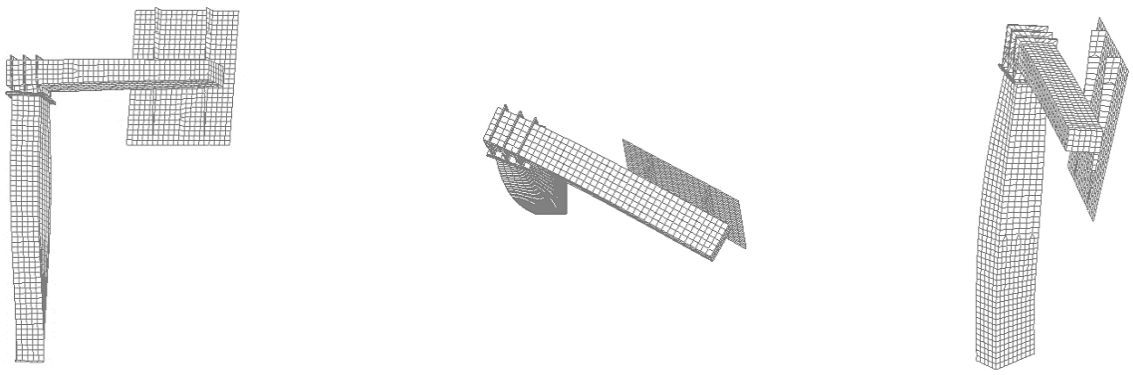

d) Mode 4 : 24,20 Hz Combined lateral (out-of-plane) bending and torsion in the column

Figure 36: Representation of the first four modes of the sign structure

Modes 1 and 3 are vertical (in-plane) modes, whereas modes 2 and 4 are horizontal (out-of-plane) modes, which contain some torsion in the column. Mode 1 presents the fundamental sway in the column which induces vertical displacement. In the case of mode 3, a higher mode with one inflexion point is reached in the column causing once again vertical displacement in the cantilever while the cantilever is also bent in-plane. Mode 2 demonstrates sway in the cantilevered arm causing some torsion in the column. However, in mode 4, a combined mode is observed with sway in the cantilever and twist in the column. To validate the accuracy of these frequency values, a 2-D beam model with the same dimensions of the 3-D shell model was created. The values obtained with this beam element model were within 3% of the ones obtained with the more detailed shell model. Once again, the more detailed models are chosen for further analysis due to their ability to receive pressures and not only line loads, and potential future work on fluid-structure interactions.

In addition to the beam models, Ambient Vibration Measurements (AVM) were taken by the Québec MTQ team on this sign structure. All the results are presented and discussed

in section 4.4: the main outcome was that the numerical model is about 13% stiffer than the real structure. Therefore, by using equation 34 above, the model was adjusted to match the measured values of natural frequencies. Thus, the modified model was used for all the following wind analysis.

4.3 Load application

4.3.1 Static load

The static wind load calculations were carried out on the structure in accordance with CAN/CSA S6-18 for sign structures. The calculation also takes into account the sign panel with different variables as will be seen below. Therefore, the wind pressure shall be determined as follows:

$$p = qC_eC_gC_p \tag{35}$$

where

q = the reference velocity pressure,

C_e = the height factor,

C_g = the gust effect factor,

C_p = the speed-up factor,

The values of q can be obtained from Appendix C of the National Building Code of Canada (NBC 2015).

In the analysis, the following factors were used:

q = 0,585 kPa, for a 50-year wind return period

C_e = 1,0 as the structure's height above ground is less than 10 m

C_g = 2,5

C_p = 1,7 for steel, 1,2 for aluminum panel.

The resulting pressures are 2,50 kPa for steel and 1,8 kPa for aluminum. Both values will be constant through the height of the structure since the height factor is constant in this case. Therefore, by simply applying those pressures on the numerical model, the equilibrium results in a horizontal displacement at the tip of the cantilevered arm of 9,2 mm and a corresponding angle of rotation of 0,16 degrees, which corresponds to the rounded value of 10 mm considered in design.

4.3.2 Periodic load

Once again, periodic loads are modeled as sinusoidal functions with different turbulence intensities to trigger resonance in the structure in the along-wind direction to represent a theoretical limiting case for situations when the natural wind gusts frequency correspond to the natural frequency of the structure. The two horizontal modes of the structure are of 10.4 Hz and 23.6 Hz, corresponding to periods of approximately 0.096 s and 0.042 s. Since we assume that natural wind acts horizontally, these are the two modes that will be triggered. The two remaining vertical modes may be useful for the analysis of truck induced gusts even though AASHTO does not require such investigation for regular overhead sign support structures.

Three sinusoidal functions, as depicted in Figure 37, are produced with a turbulence intensity of 5%, 10% and 15% to observe the impact of this variable. These periodic functions are then applied to the static wind load profile as a time function in ADINA to produce a varying intensity wind to trigger dynamic amplifications in the sign structure. For this structure, an analysis duration of 4.8 s is sufficient to show more than 40 cycles of the fundamental mode of vibration. The resulting time histories of horizontal transverse tip displacements of the structure under these 3 periodic functions are presented in Figure 38.

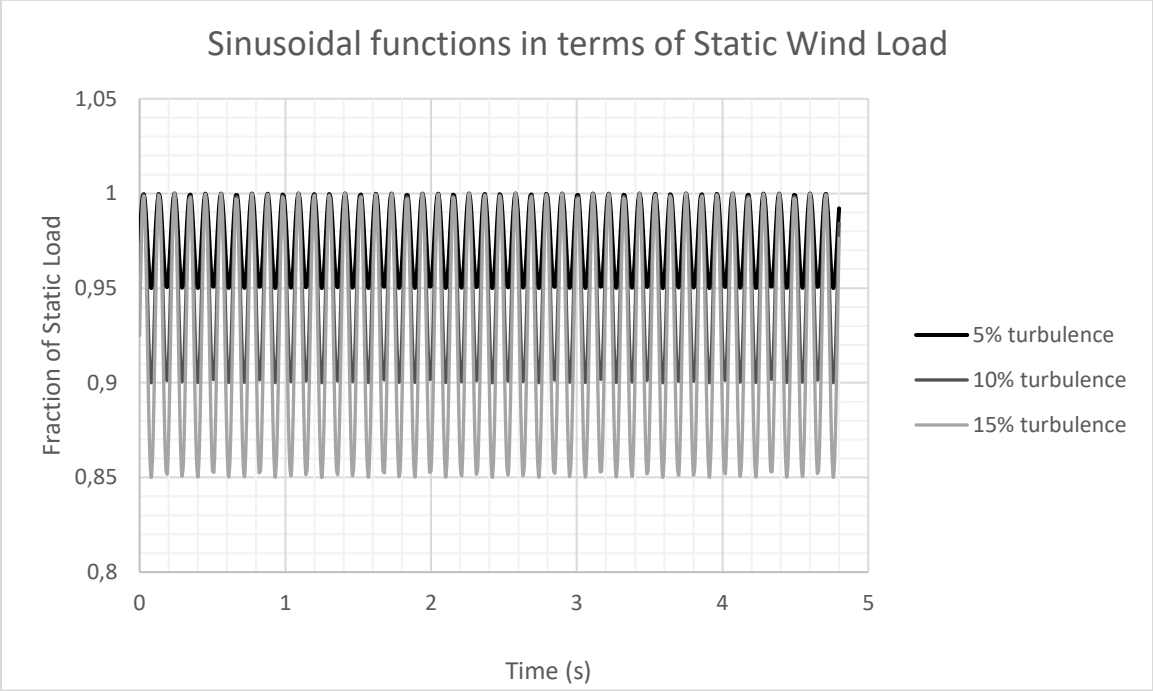

Figure 37: Sinusoidal functions for the sign structure's first mode in terms of Static Wind Load

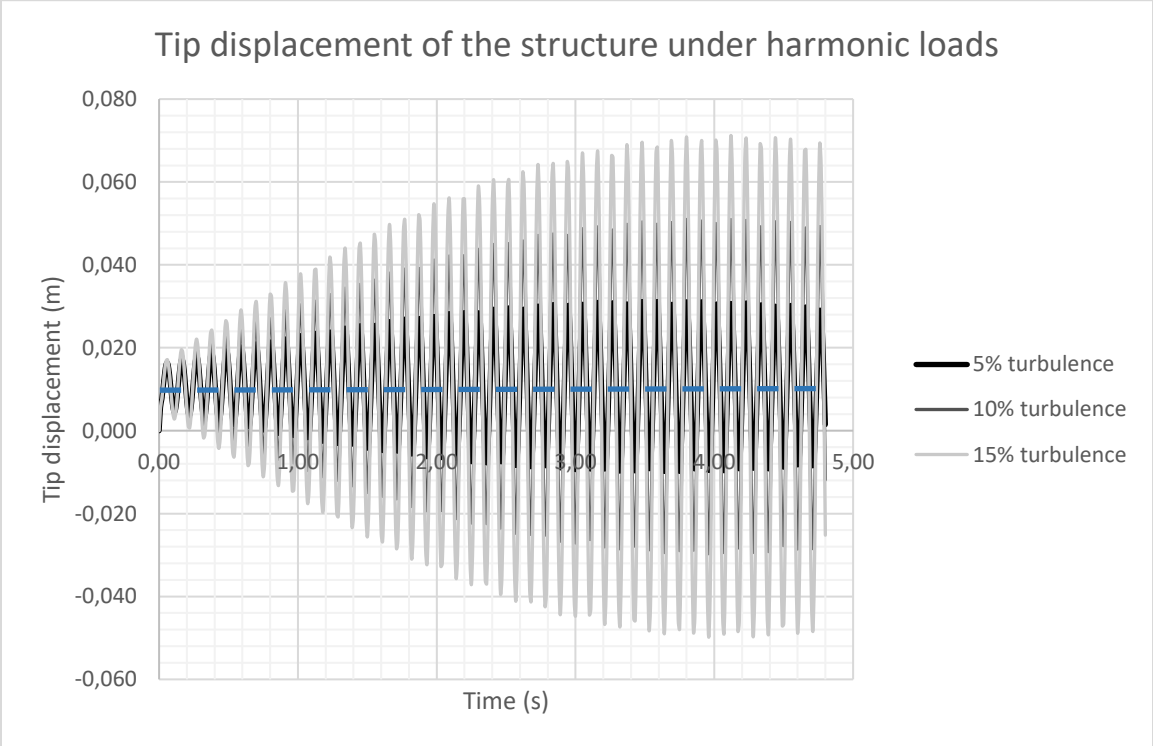

Figure 38: Tip displacement of the sign structure under harmonic loads of different turbulence intensities.

As observed, resonance is present in each turbulence intensity case with a tip displacement that keeps growing initially. However, the resonance ends as the response is reaching a steady-state after 3.5 seconds for each turbulence intensity. The tip displacement reaches a maximum of approximately 3.0 cm for 5% turbulence, 5.0 cm for 10% turbulence and 7.0 cm for 15% turbulence after 3.5 s. Considering that all three profiles have the same mean value of x, as shown with a dashed line on Figure 38, a linear relationship seems to exist between them. Adding a value y which corresponds to the increased amplitude for each additional 5% turbulence, it can be written that:

$$3.0 = x + y$$

$$5.0 = x + 2y$$

$$7.0 = x + 3y$$

Solving this simple set of equations yields a value of 1.0 cm for the mean x and of 2.0 cm for each additional 5% turbulence y. Therefore, an estimate of the maximum tip displacement after 3.5 s for any turbulence intensity with a maximum value equal to the maximum static wind load for this particular structure can be made using the following formula:

$$d_{max} = x + 0.4t_i \quad (36)$$

where

d_{max} = Maximum tip displacement in a pure harmonic case

t_i = Turbulence intensity of the periodic function

x = Mean value of displacement

Thus, this formula allows to theoretically predict the maximum steady-state tip displacement after 3.5 s of the sign structure under a perfectly harmonic load of any turbulence intensity assuming elastic deformations. Table 15 presents the value for a turbulence intensity up to 50% with the same mean value of 1.0 cm.

Table 15: Tip displacement of the sign structure under perfectly harmonic wind loads of different turbulence intensities

Turbulence intensity (%)	Maximum tip displacement (cm)
5	3.0
10	5.0
15	7.0
20	9.0
25	11.0
30	13.0
35	15.0
40	17.0
45	19.0
50	21.0

Therefore, with a harmonic load of the same mean value with 50% turbulence intensity, the maximum out-of-plane horizontal displacement at the tip of the cantilevered arm can reach 21 cm after 3.5 s assuming a linear elastic response, which represents more than 21 times the maximum static displacement predicted of just under 1 cm. However, a perfectly harmonic scenario with such a high frequency and turbulence intensity is extremely unlikely to occur naturally.

4.3.3 Random loads

Similarly, once the model has been responding correctly to static and harmonic wind loads, random wind load application can be undertaken. The same 100 random profiles randomly generated with the algorithm presented in section 3.3.3 are reutilized for the sign structure herein for a time history of 4.8 seconds, which results in more than 40 cycles of vibration in the fundamental mode.

The methodology remains unchanged from what was done for the monopoles. 10 random wind histories were generated for each 10% step of the maximum static load. In other

words, 10 profiles were generated with a mean value of 10% of the maximum static load, 10 different profiles were generated with a mean value of 20% of the maximum static load, and so on. Also, within each group of 10 random wind profiles, 5 of them were given a turbulence intensity of 10%, while the other 5 were given a turbulence intensity of 20%.

Once again, horizontal displacement time history at the tip of the cantilever was calculated with a time step of 0.01 s for a total of 480 steps computed. All the results are presented in Annex B.

We first discuss the results for the two random wind profiles at 30% of the maximum static load as depicted in Figures 39 and 40. The first profile (3.3) has a turbulence intensity of 10% whereas the second profile (3.8) has a turbulence intensity of 20%. In 3.3, the response remains relatively flat with a maximum displacement of about 8 mm, whereas 3.8 displays a quasi-resonance phenomenon with a maximum displacement of approximately 17 mm. Such different responses can be explained by looking at the frequency content of the concerned wind profiles, as shown in Figure 41. As expected, the random profile 3.8 displays a peak of frequency content around and below 10 Hz, which coincides with the fundamental frequency of the sign structure, whereas 3.3 does not display any peak in frequency content near 10 Hz, leading to a flat response with no trace of resonance. Furthermore, frequencies over 20 Hz have negligible effects, thus there is no presence of higher modes in the response of the sign structure. Once again, the frequency content of the applied wind has a great influence on the dynamic response of the structure.

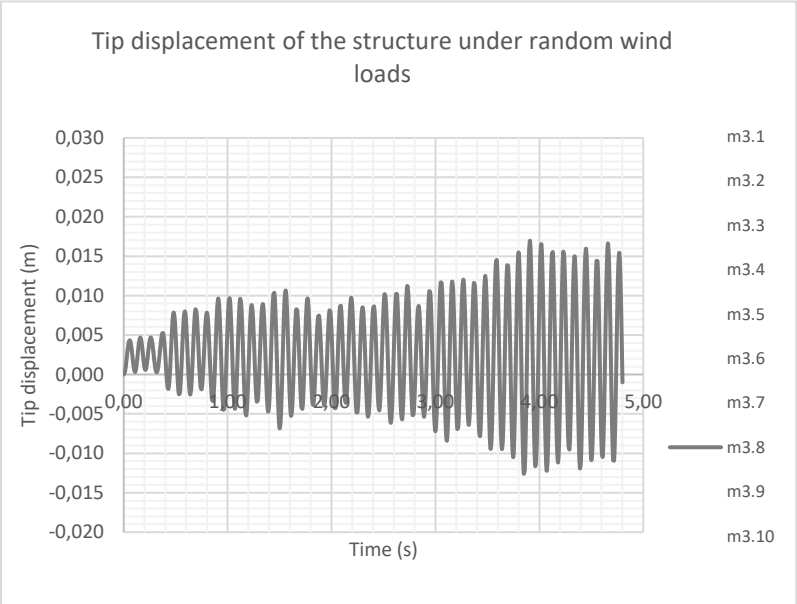

Figure 39: Horizontal tip displacement of the cantilevered sign structure under random wind time history 3.8

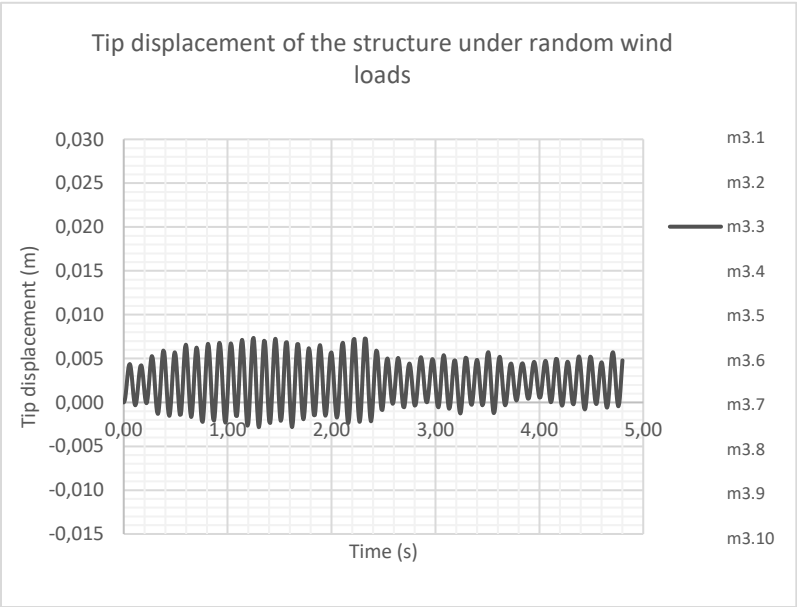

Figure 40: Horizontal tip displacement of the cantilevered sign structure under random wind time history 3.3

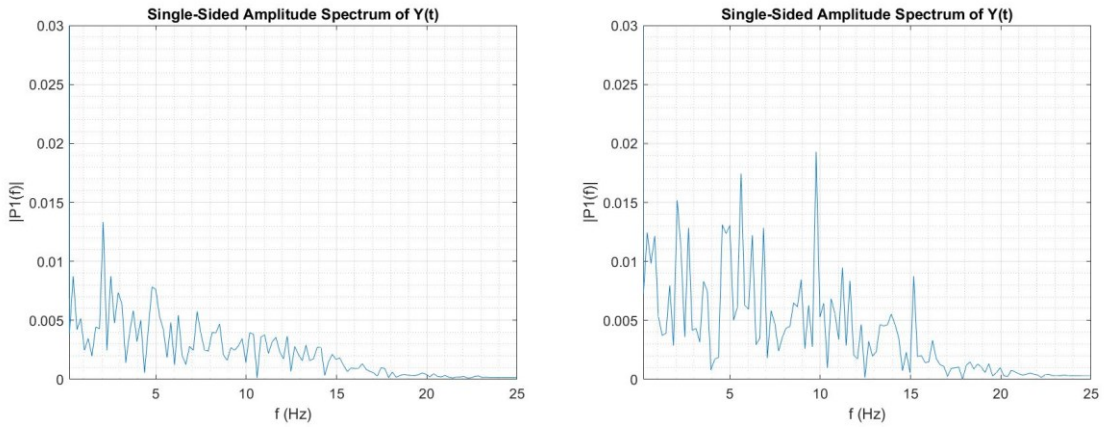

(a) (b)

Figure 41: Frequency content of random wind time history a) 3.3 and b) 3.8

Now looking at profiles with greater mean values, such as 90% of the maximum static load, the results are different than at lower amplitudes. As shown in Figures 42 and 43, the resulting tip displacements are greater but much smoother, as the responses under two different random wind time histories look similar. Also, now that the mean value approaches the maximum static load, the influence of frequency content of the wind history appears to be fairly diminished in comparison to lower mean value loads with no clear presence of resonance for both cases. Figure 44 shows the frequency content of profiles 9.2 and 9.3, which display different frequency contents. However, these differences do not clearly appear on the resulting displacement time histories. Since natural wind does not contain a high concentration of frequencies above 20 Hz, which corresponds to the second horizontal mode of vibration of the structure, the fundamental mode is dominant in the response of this cantilevered sign structure. The displacement reaches slightly above 22 mm for the 9.2 loading case and nearly reaches 24 mm under 9.3. The maximum displacement reached under 100% of the maximum static load is 25 mm. As a comparison, the maximum displacement under static load is just under 10 mm, which is about 2.5 times smaller than what is reached by the critical random wind time history. Therefore, the gust factor of 2.5 used in CSA S6-18 Standard as presented in

Section 4.3.1 is accurate in representing an equivalent static load applied on the cantilevered sign structure.

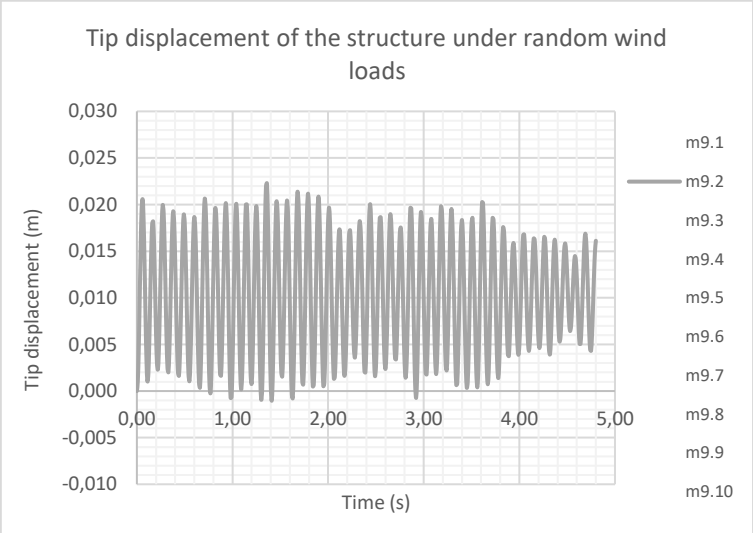

Figure 42: Horizontal tip displacement of the cantilevered sign structure under random wind time history 9.2

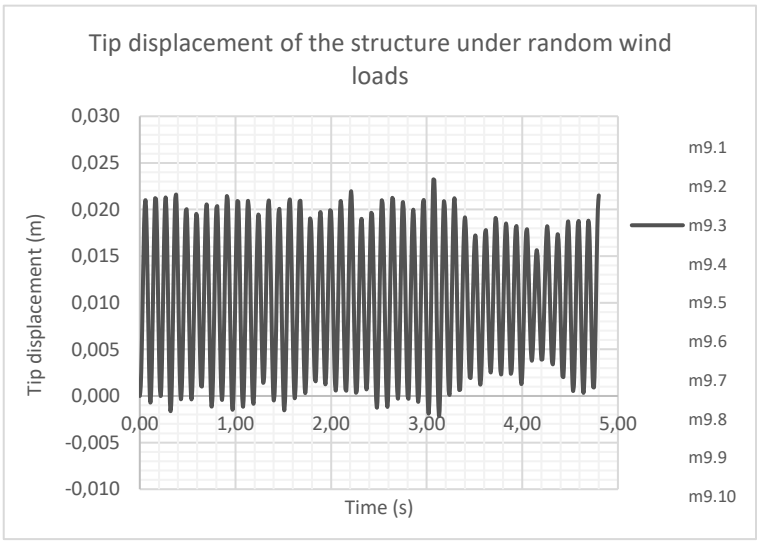

Figure 43: Horizontal tip displacement of the cantilevered sign structure under random wind time history 9.3

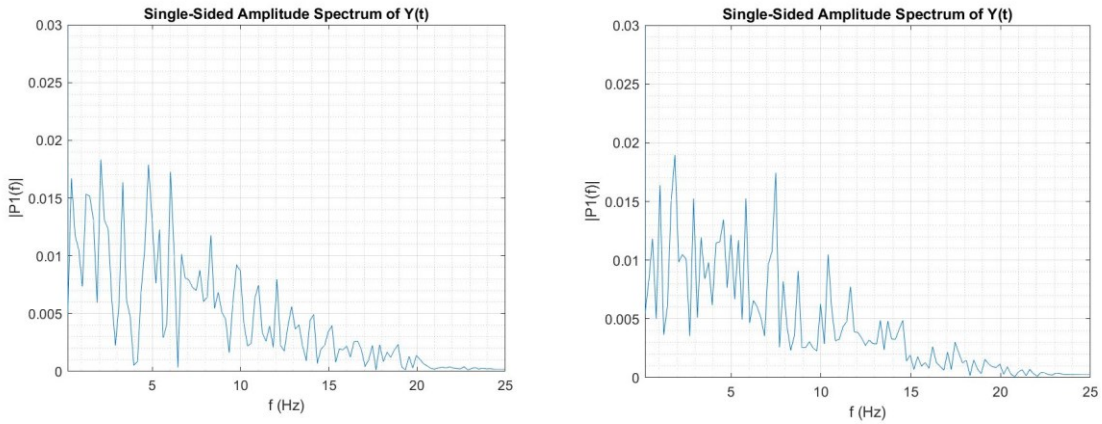

(a) (b)

Figure 44: Frequency content of random wind time history a) 9.2 and b) 9.3

Another interesting aspect to look at is the resonance in the structure under random wind loads. To create even more resonance than what is seen throughout all the random wind load scenarios, the time history 6.6 was chosen to be added and averaged with a perfectly harmonic case. This particular wind time history was selected due to its very flat resulting response by itself. The resulting displacements for the initial random wind time history, the averaged spectrum and the perfectly harmonic case are shown in Figure 45.

(a)

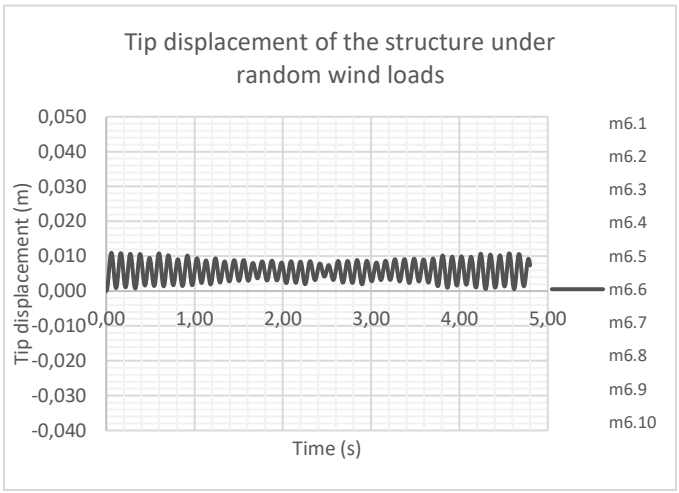

(b)

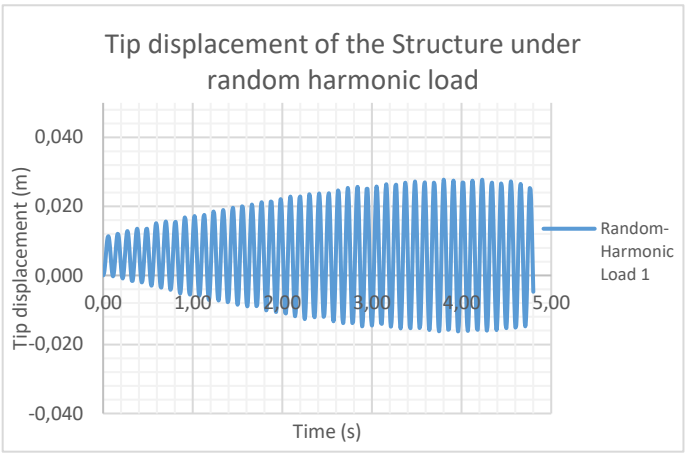

(c)

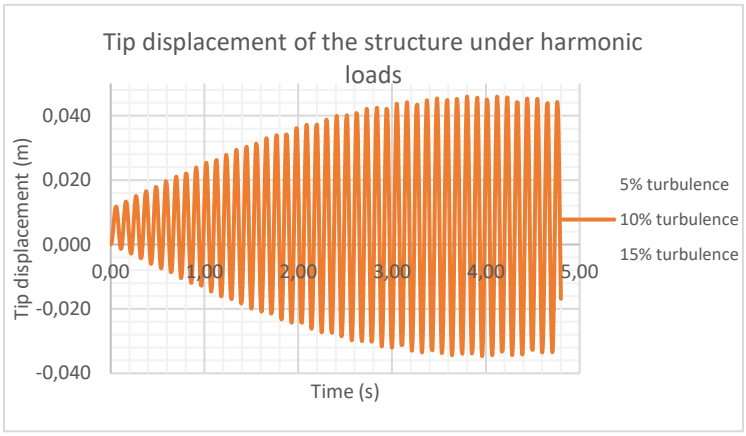

Figure 45: Horizontal tip displacement of the cantilevered sign structure under a) random wind time history 6.6, b) averaged time history and c) perfectly harmonic case

As the random wind time history 6.6 only reaches approximately 12 mm by itself, the averaged scenario displays a maximum displacement of about 28 mm whereas the perfectly harmonic case goes to 46 mm. The value obtained with the averaged time history approximately corresponds to the average maximum displacement value of the random wind time history 6.6 and the perfectly harmonic case. The averaged scenario produces a maximum displacement of 2.8 times greater than the maximum equivalent static load, which surpasses the gust effect factor of 2.5 by 12 %. Therefore, in a random wind time history with a high frequency content corresponding to the fundamental

frequency of the cantilevered sign structure, the equivalent static predictions yield slightly unconservative values of maximum displacement.

As the resulting displacements under random wind loads are looked through, some scenarios seem to display a pulsing/beating effect, which corresponds to a lower frequency in the response of the structure, as shown in Figures 46 and 47. In Figure 46, the resulting displacement of 3.7 shows a beating of approximately 2 seconds, whereas in Figure 47, there seems to be a beating of 1,7 seconds from 5.6.

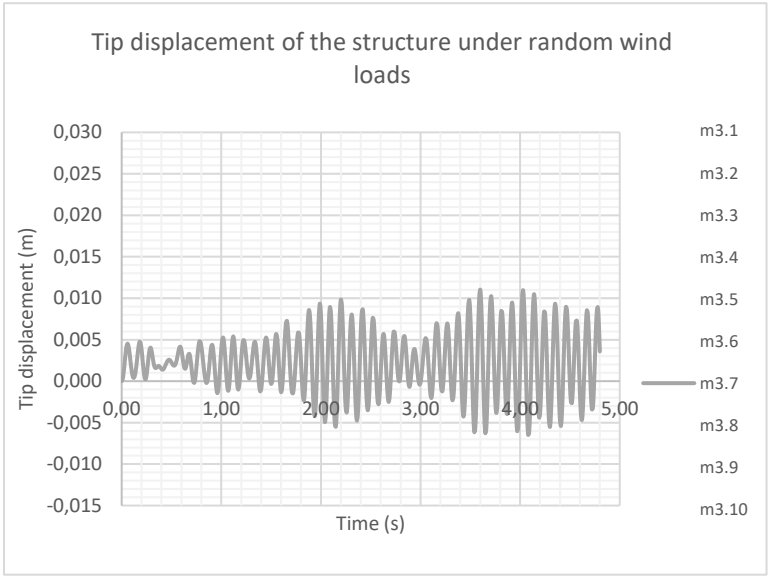

Figure 46: Beating in the displacement of the sign structure under random wind time history 3.7

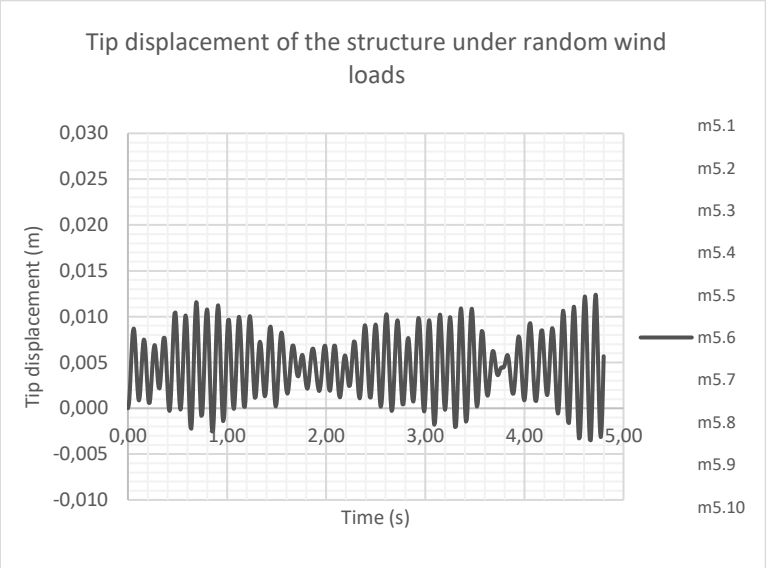

Figure 47: Beating in the displacement of the sign structure under random wind time history 5.6

Beating in the vibration of structures is often present and can be a result of factors such as inherent structural properties or signature in the frequency content of the applied load. After investigation, beating in this cantilevered sign structure appears to be a result of the frequency content of the applied random wind time histories. Looking at the frequency content of 3.7 in Figure 48a, there is a peak of density around 0,5 Hz, which corresponds to the beating period of 2 seconds. On the other hand, for 5.6 in Figure 48b, a peak of density appears just around 0,6 Hz, which once again corresponds to the beating period of 1,7 seconds present in the response of the structure. The fact that this structure is fixed on an elevated highway segment might also contribute to the lower frequency beating, but since the natural frequency of the elevated highway is unknown, it was not included in the numerical analysis. Thus, the beating observed in the numerical analysis is most likely due to the frequency content of the applied wind history rather than the inherent structural characteristics of the cantilevered sign structure.

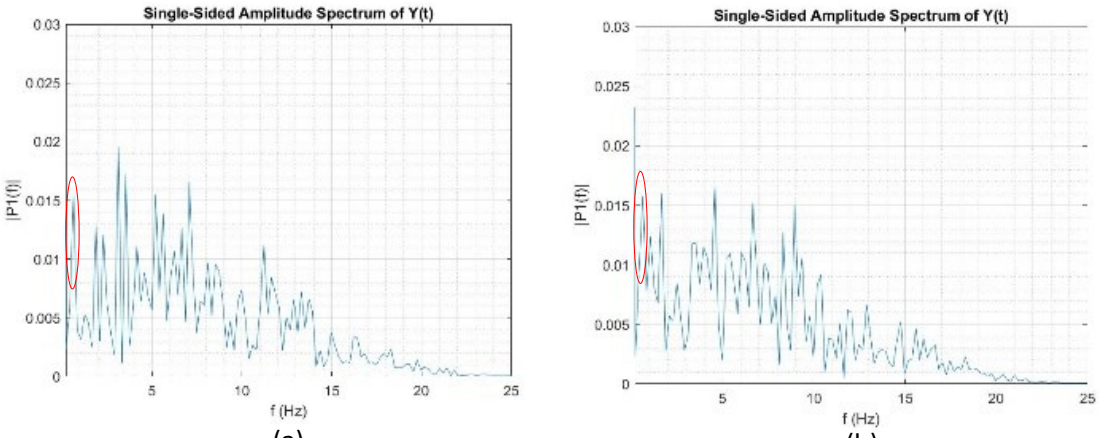

(a) (b)

Figure 48: Frequency content of random wind time history a) 3.7 and b) 5.6

4.4 Field data

In-situ measurements have been provided by the Ministry of Transportation of Québec (MTQ). Their field team has deployed on the site, taken measurements and directly provided the resulting frequencies of the first four modes of the sign structure. They are listed in Table 16 below.

Table 16: Natural frequencies of the sign structure as measured in-situ

Natural frequencies (Hz)							
Mode 1		Mode 2		Mode 3		Mode 4	
Mean	Std. Dev.	Mean	Std. Dev.	Mean	Std. Dev.	Mean	Std. Dev.
7.48	0.01	9.40	0.01	19.78	0.01	21.25	0.01

The values obtained on site differed by approximately 13% from the values found via numerical analysis. The difference can be accounted to the perfectly rigid base and connection modeled with ADINA, whereas the actual structure is not perfectly rigid and is mounted on an elevated highway portion, which also has some inherent stiffness, damping and dynamic properties.

Recalling equation 34 from section 3.4, the reduced Modulus of Elasticity technique can be used to adjust the numerical model in the same manner as the exercise conducted with tower M2.

4.5 Fatigue considerations

In order to determine the vulnerability of the cantilevered sign structure to fatigue, the random wind load time history which caused the greatest displacement was selected. Once again, the selected scenario had a mean value of 100% of the maximum static wind load. Fatigue is characterised as a number of cycles at a given stress amplitude, therefore the stress amplitude must be found. ADINA can display both the stress and strain throughout the structure. Thus, for the critical random case, the maximum stress amplitude at the base of the structure was found to be 60 MPa. Superimposing this stress value to the G40.21 350W Steel SN Curve as shown in Figure 49, from which the structure is made of, the following result is observed.

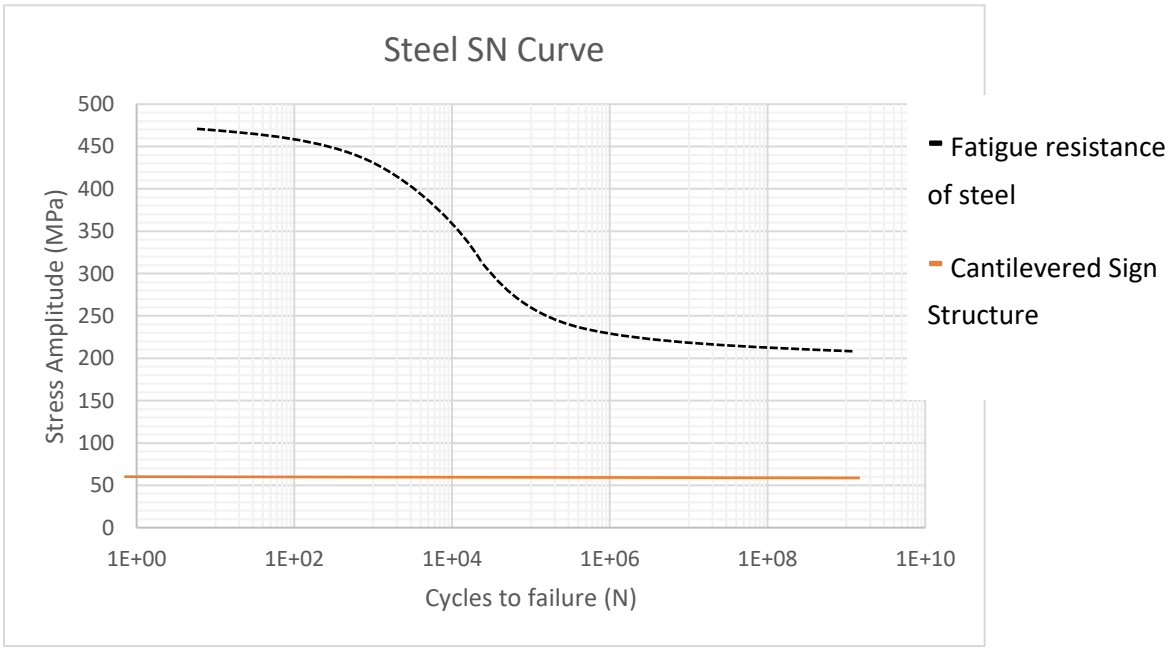

Figure 49: Comparison of fatigue resistance of steel with maximum stress amplitude of the cantilevered sign structure

Clearly, under normal conditions of random wind loads, this cantilevered sign structure is far from suffering any fatigue damages after 10^8 cycles. Such margin of safety was expected since this structure was designed to be very stiff and resistant to avoid any potential fatigue issues. Therefore, under normal environmental conditions, excluding high resonance phenomena and extreme icing conditions, this cantilevered sign structure will fill its performance requirements and will not be affected by fatigue.

5. Conclusions

In summary, the main conclusions emanating from this research can be stated as follows:

- For in-line oscillations, the response of the structures is greater with growing mean value of wind speed and growing turbulence intensity, as expected.
- For Telecommunication Monopoles, the fundamental mode of vibration is dominant for all types of loads, and this dominance becomes even more significant with increasing mean value of wind speed.
- Under perfectly harmonic loads tuned to the towers' fundamental mode, M1 and M2 reach resonance with an ever-growing tip displacement with time, assuming linear elastic response. Furthermore, the maximum displacement follows a linear relationship in terms of turbulence intensity of the applied wind function. An equation was developed to determine the theoretical maximum tip displacement of tower M2 under resonance after 100 seconds for a wind with maximum value corresponding to the maximum static load at any turbulence intensity. A similar derivation can be followed to obtain displacement values under resonance for winds of different mean amplitude and at any chosen time for tower M1 and M2
- The maximum tip displacement found throughout the 100 random wind load time histories applied to towers M1 and M2 was 15 cm and 22 cm respectively. These values represent a dynamic amplification of 51% and 98 % to their respective maximum equivalent static displacement. Considering that CAN/CSA S37-18 suggests a basic gust factor of 2.0, the values found remain on the conservative side. However, the value of 1.0 suggested by Annex N of the Standard to assess the response of pole structures to fluctuating wind components could lead to unconservative results.
- Under perfectly harmonic loads tuned to the cantilevered sign structure's fundamental mode, the tip displacement at the end of the cantilever initially grows but stabilizes after approximately 3.5 seconds for the three turbulence

intensities inspected. Once again, a linear relationship exists between the maximum displacement after stabilization and turbulence intensity of the applied wind function. An equation was developed to predict the maximum tip displacement of the sign structure once it stabilized for a wind with maximum value corresponding to the maximum static wind load at any chosen turbulence intensity.

- Throughout the 100 random wind load time histories applied to the cantilevered sign structure, the maximum displacement experienced by the tip of the cantilever was 25 mm. This displacement corresponds to 2.5 times the value of maximum static load displacement. Therefore, the 2.5 gust factor suggested in CAN/CSA S6-18 is accurate for this sign structure.
- The beating effect observed in the response of the cantilevered sign structure was attributed to the frequency content of the applied wind time history. However, the natural frequency associated with the elevated highway segment was not considered in the numerical analysis and may be a source of additional beating in the actual response of the structure.
- Both Telecommunication Monopoles will not suffer fatigue damages under normal operation conditions, according to the S-N curve method (Wohler, 1855).
- The Cantilevered Sign Structure will not suffer fatigue damages and will not be subjected to excessive vibrations that might distract motorists under normal operating conditions, according to the S-N curve method (Wohler, 1855).

6. Future Work

Following this research, many avenues can be taken to pursue further work in the area. Some of the paths include:

- Build a Computational Fluid Dynamics (CFD) model in order to take into account the Fluid-Structure Interactions (FSI) and have a more realistic response of the structures. This is not feasible at the moment due to heavy computational demands and limited capabilities available but it may become possible in future years.
- Analyze an important amount of structures of the same type, for example monopole towers, and develop simple relationships to determine the expected natural frequencies of a particular structure before taking any measurements or doing any numerical modelling.
- Returning on sites to measure the natural frequencies of the structures more precisely with more instruments installed along the height of the structure. In addition, this configuration would allow the determination of damping values for higher modes.
- Monitor real-time wind time histories with a precise instrument while taking measurements on the structure, and then compare its response by inputting this wind time history in the numerical model to obtain further validation of the model.
- Evaluate the effect of defects or damages on certain structures by considering them in the numerical models.

References

AASHTO, *Standard Specifications for Structural Supports for Highway Signs, Luminaires and Traffic Signals.* Americam Association of State Highway and Transportation Officials, Washington, D.C. (2015).

ADINA R&D Inc. *Automatic Dynamic Incremental Nonlinear Analysis (ADINA)*. Theory and Modelling Guide. Report ARD 00-7, Watertown, MA (2019).

Albert, M.N., Manuel, L., Frank, K.H., Wood, S.L., *Field Testing of Cantilevered Traffic Signal Structures under Truck-Induced Gust Loads.* Report FHWA/TX-08/0-4586-2, The University of Texas at Austin, (2007).

ARTeMIS Modal Software for Operational Modal Analysis, Structural Vibration Solutions A/S, Denmark (2018).

ASCE-7, *Minimum Design Loads for Buildings and Other Structures.* ANSI/ASCE-7, American Society of Civil Engineers, Reston, Virginia (2016).

ASM International, *Failure Analysis and Prevention, Chapter 14: Fatigue.* ASM Handbook, (2008).

Arya, S.P.S., and Plate, E.J., *Modeling of the stably stratified atmospheric boundary layer.* Journal of the Atmospheric Sciences, Vol. 26, (1969), pp.656-665.

Bathe, Klaus-J*ü*rgen. *Finite Element Method.* John Wiley & Sons, Inc., (2008).

Bearman, P.W., *Circular cylinder wakes and vortex-induced vibrations.* Journal of Fluids and Structures, Vol. 27(5), (2011), pp.648-658.

Besem, F., Thomas, J.P., Kielb, R.E., Dowell, E.H., *An aeroelastic model for vortex-induced vibrating cylinders subject to frequency lock-in.* Journal of Fluids and Structures, Vol. 61, (2016), pp.42-59.

Blevins, R.D., *Flow-induced vibration,* 2nd Edition, Van Nostrand Reinhold, (1990), 451 pp.

Boardman, B., Deere, C., *Fatigue Resistance of Steels.* ASM Handbook, Vol. 1, (1990), pp.673-688.

CAN/CSA S37-18, *Antennas, Towers and Antenna-Supporting Structures. Canadian Standards Association, Mississauga, Ontario, (2018).*

Caracoglia, L. and Jones, N.P., *Wind-Induced Failures of Highway Light Poles During Winter Storms.* ASME 2006 Pressure Vessels and Piping Conference, (2006), pp.197-206.

Chen, G., Wu, C., Yu, J., Dharani, L., Barker, M., *Fatigue Assessment of Traffic Signal Mast Arms based on Field Test Data Under Natural Wind Gusts.* Journal of the Transportation Research Board, Vol. 1770, (2001), pp.188-194.

Chien, C.W. and Jiang, J.J., *Case study of wind-resistant design and analysis of high mast structures based on different wind codes.* Journal of Marine Science and Technology, Vol. 16, (2008), pp.275-287).

Connor, R.J., Collicott, S.H., DeSchepper, A.M., Sherman, R.J., Ocampo, J.A., *NCHRP Report 718: Fatigue Loading and Design Methodology for High-Mast Lighting Towers.* Transportation Research Board of the National Academies, Washington, D.C. (2012).

Davenport, A.G., *The application of statistical concepts to the wind loading of structures.* Proc., Institution of Civil Engineers (U.K.), Vol. 28, (1964), pp.187-196.

Dexter, R.J., Ricker, M.J., *NCHRP Report 469: Fatigue-Resistant Design of Cantilevered Signal, Sign, and Light Supports.* Transportation Research Board of the National Academies, Washington, D.C. (2002).

Ding, J., Chen, X., Zuo, D., Hua, J., *Fatigue life assessment of traffic-signal support structures from an analytical approach and long-term vibration monitoring data.* Journal of Structural Engineering, Vol. 142(6), (2016).

EIA/TIA-222-H, *Structural Standard for Antenna Supporting Structures and Antennas.* Telecommunication Industry Association, (2018).

Euler, L., *Principes généraux du mouvement des fluides.* Mémoires de l'Académie des Sciences de Berlin, Vol. 11, (1757), pp.274-315.

Eurocode 8, *Design of Structures for Earthquake Resistance.* EU, (2016).

Fouad, F.H., Davidson, J.S., Delatte, N., Calvert, E.A., Chen, S.E., Nunez, E., Abdalla, R., *NCHRP Report 494 : Structural Supports for Highway Signs, Luminaires, and Traffic Signals.* Transportation Research Board of the National Academies, Washington, D.C. (2003).

Fung, Y.C., *An Introduction to the Theory of Aeroeslasticity.* Courier Corporation, (2002), 498 pp.

Garrett, J.L., *Flow-induced vibration of elastically supported rectangular cylinders.* Retrospective Theses and Dissertations, Iowa State University, (2003).

Giaccu, G., Caracoglia, L., *Wind-load fragility analysis of monopole towers by layered stochastic-approximation-Monte-Carlo method.* (2018).

Goodman, J. *Mechanics Applied to Engineering.* Longman, Green & Company, London, (1899).

Greenway, M.E., *An analytical approach to wind velocity gust factors.* Journal of Industrial Aerodynamics, Vol.5, (1979), pp.61-92.

Hajali, M., *Finite Element Evaluation of Modal Stresses in Cantilever Highway Sign Structures.* Advances in Hurricane Engineering Conference, ASCE, Miami, FL., (2012).

Harper, B.A., Kepert, J.D., Ginger, J.D., *Guidelines for converting between various wind averaging periods in tropical cyclone conditions.* World Meteorological Organization, WMO/TD-No. 1555, (2010), 62 pp.

Hémon, P., Amandolese, X. and Andrianne, T., *Galloping Oscillations of Prisms and Energy Harvesting in Wind Tunnel.* First International Symposium on Flutter and its Application, (2016), 10pp.

Institute for Research in Contruction (IRC), *National Building Code of Canada (NBC) 2015: Structural Commentaries (Part 4 of Division B)*. (2015).

Jacobsen, N.J., Andersen, P., Brincker, R., *Separating Structural Modes and Harmonic Components in Operational Modal Analysis.* IMAC XXIV Conference, (2006).

Johns, K.W., Dexter, R.J., *The development of fatigue design load ranges for cantilevered sign and signal support structures.* Journal of Wind Engineering and Industrial Aerodynamics, Vol. 77, pp.315-326.

Kacin, J., Rizzo, P., Tajari, M., *Fatigue analysis of overhead sign support structures.* Journal of Engineering Structures, Vol. 32(6), (2010), pp.1659-1670.

Kaczinski, M.R., Dexter, R.J., Van Dien, J.P., *NCHRP Report 412: Fatigue-Resistant Design of Cantilevered Signal, Sign and Light Supports.* Transportation Research Board of the National Academies, Washington, D.C. (1998).

Kalpakjian, S. *Manufacturing Engineering and Technology.* 3rd Edition, Addison-Wesley Publishing Co, Boston, (1995), 1271 pp.

Kumar, M.P., Raju, P., Navya, M., Naidu, G.T., *Effect of wind speed on structural behaviour of monopole and self-support telecommunication towers.* (2017).

Li, X., Whalen, T.M., Bowman, M.D., *Fatigue Strength and evaluation of double-mast arm cantilevered sign structures.* Journal of Transportation Research Record, Vol. 1928(1), (2005), pp.64-72.

Lupi, F., Niemann, H.J., Hoffer, R., *Limit Cycles in Vortex-Induced Vibrations: a Critical Analysis.* Procedia Engineering Journal, Vol. 199, (2017), pp.699-704.

McDonald, J.R., Mehta, K.C., Oler, W.W., Pulipaka, N., *Wind Load Effects on Signs, Luminaires and Traffic Signal Structures.* Report 1303-1F, Texas Department of Transportation, (1995).

Miller, C., *Defining the effective duration of a gust.* Proc. 12th International Conference Wind Engineering, ICWE12, (2007), pp.759-766.

MoHo s.r.l., *TROMINO Instrument,* ENGY 3G model, Venice, Italy (2002).

Panton, R.L., *Incompressible Flow.* 3rd Edition, Wiley Student Edition, (2005), 821 pp.

Parkinson, G.V., *Mathematical models of flow-induced vibrations of bluff bodies.* Springer, (1974), 81 pp.

Peil, U. and Behrens, M., *Fatigue of tubular steel lightning columns under wind load.* Journal of Wind and Structures, Vol. 5, (2002), pp.463-478.

Placzek, A., Sigrist, J.F., Hamdouni, A., *Numerical Simulation of an Oscillating Cylinder in a Cross-Flow at Low Reynolds Number: Forced and Free Oscillations.* Journal of Computers and Fluids, Vol. 38(1), (2009).

Rice, J.A., LaFave, J.M., Mehuys, C.H., *End Connection Effects on Vortex Shedding Susceptibility of Welded Aluminum Truss Tubular Web Members.* Journal of Performance of Constructed Facilities, Vol. 22, (2008).

Roy, S., Park, Y.C., Sause, R., Fisher, J.W., Kaufmann, E.J., *NCHRP Web-Only Document 176: Cost-Effective Connection Details for Highway Sign, Luminaire, and Traffic Signal Structures.* Transportation Research Board of the National Academies, Washington, D.C. (2011).

Samali, B., *Effects of Higher Modes on Response of Wind-Excited Tall Buildings.* In: Beedle L.S. (eds) Second Century of the Skyscraper, Springer, (1998), pp.697-703.

Sarpkaya, T., *A critical review of the intrinsic nature of vortex-induced vibrations.* Journal of Fluids and Structures, Vol. 19(4), (2004), pp.389-447.

Solari, G. and Pagnini, L.C., *Gust Buffeting and Aeroelastic Behaviour of Poles and Monotubular Towers.* Journal of Fluids and Structures, Vol. 13, (1999), pp.877-905.

Strouhal, V., *Ueber eine besondere Art der Tonerregung*. Annalen der Physik und Chemie, 3rd series, **5** (10) pp.216-251.

Vickery, B.J. and Basu, R.I., *Simplified Approaches to the Evaluation of the Across-Wind Response of Chimneys.* Journal of Wind Engineering and Industrial Aerodynamics, Vol. 14, (1983), pp.153-166.

Wieghaus, K.T., *Mitigating Wind-Induced Fatigue in Steel Traffic Signal Support Structures.* Doctoral dissertation, Texas A&M University, (2015).

Williamson, C.H.K. and Govardhan, R., *Vortex-Induced Vibrations.* Journal of Annual Review of Fluid Mechanics, Vol. 36(1), (2004), pp.413-455.

Wöhler, A. *Theorie rechteckiger eisemer Brückenbalken mit Gitterwänden und mit Blechwände.* Zeitschrift für Bauwesen, Vol 5, (1855), pp.121-166.

Zhou, Y., Kim, S., Alam, M., Sakamoto, H., *Flow-induced vibrations of two circular cylinders in tandem arrangement. Part 1: Characteristics of vibration.* Journal of Wind Engineering and Industrial Aerodynamics, Vol. 97, (2009), pp.304-311.

Zuo, D. and Letchford, C., *Investigation of Wind-Induced Highway Lightning Pole Vibration Using Full-Scale Measurement.* Texas Tech University, Multidisciplinary Research in Transportation, (2008).

Annex A: Results of Tower M1 under random wind time histories

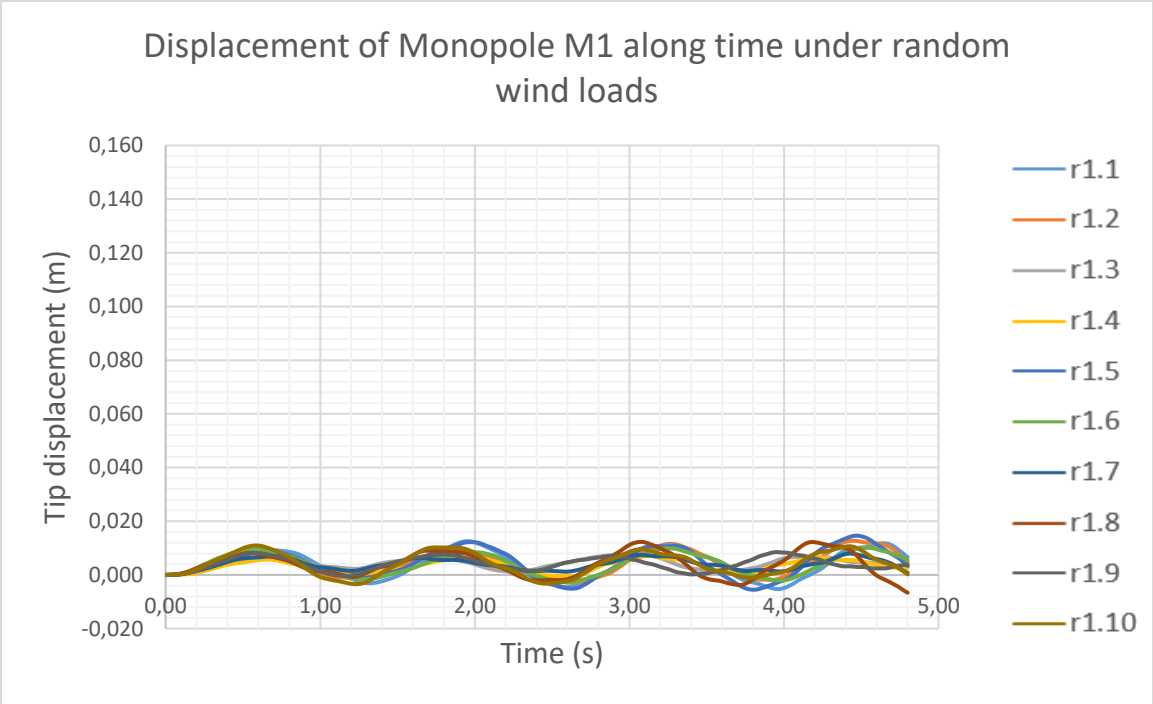

Figure A1: Horizontal tip displacement of Monopole M1 under random wind load time histories of mean value of 10% of maximum static load

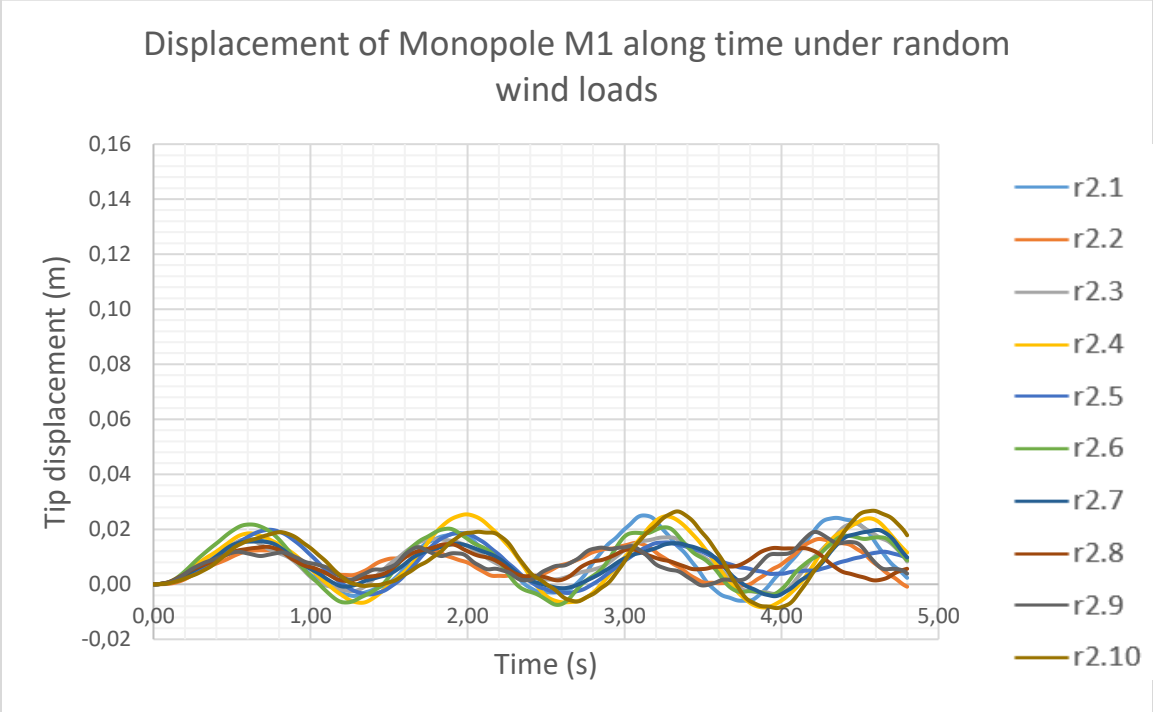

Figure A2: Horizontal tip displacement of Monopole M1 under random wind load time histories of mean value of 20% of maximum static load

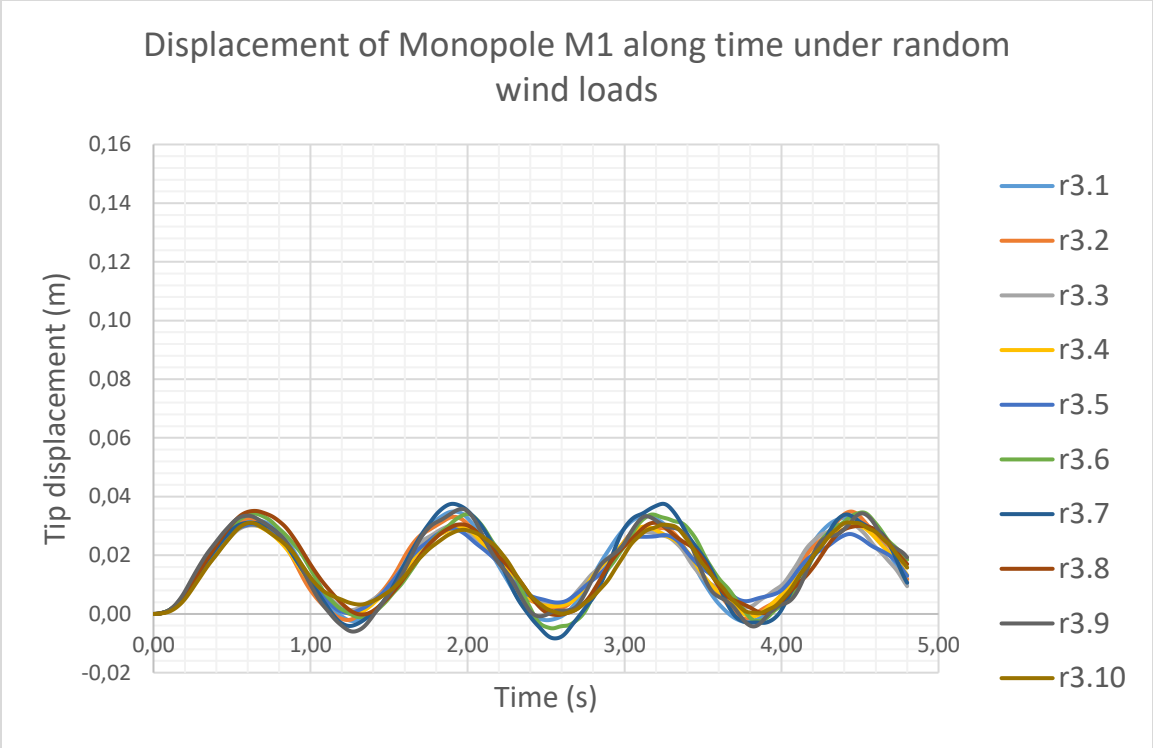

Figure A3: Horizontal tip displacement of Monopole M1 under random wind load time histories of mean value of 30% of maximum static load

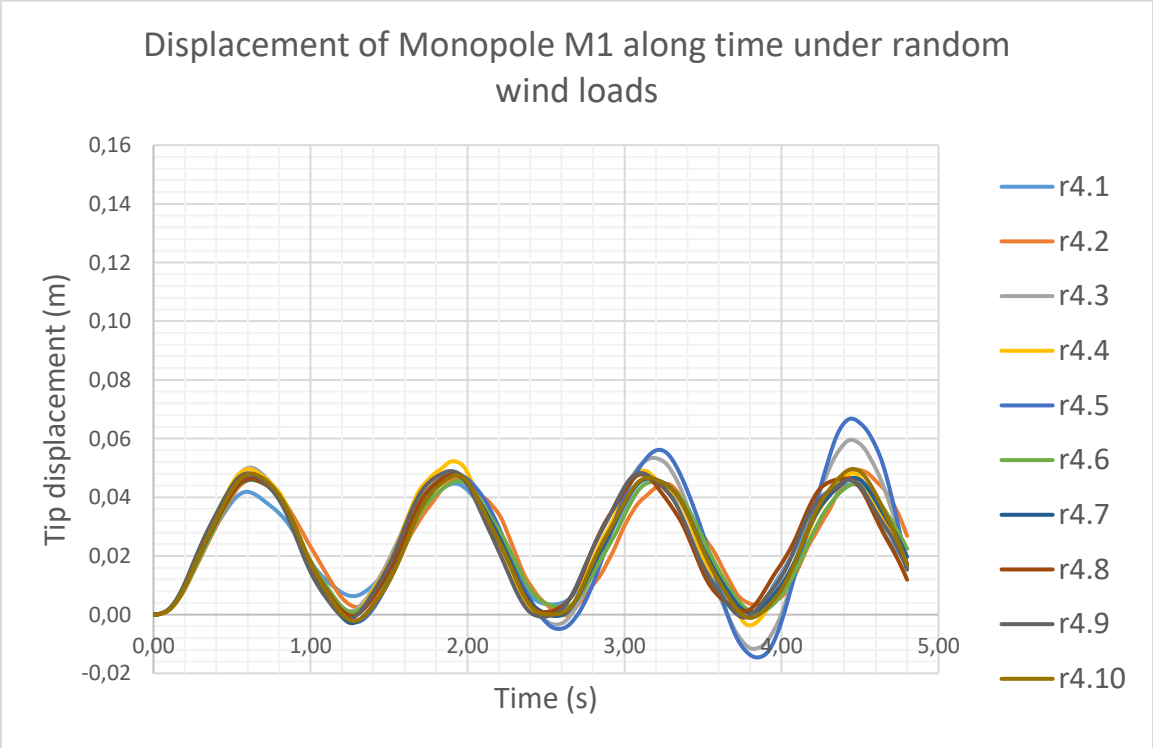

Figure A4: Horizontal tip displacement of Monopole M1 under random wind load time histories of mean value of 40% of maximum static load

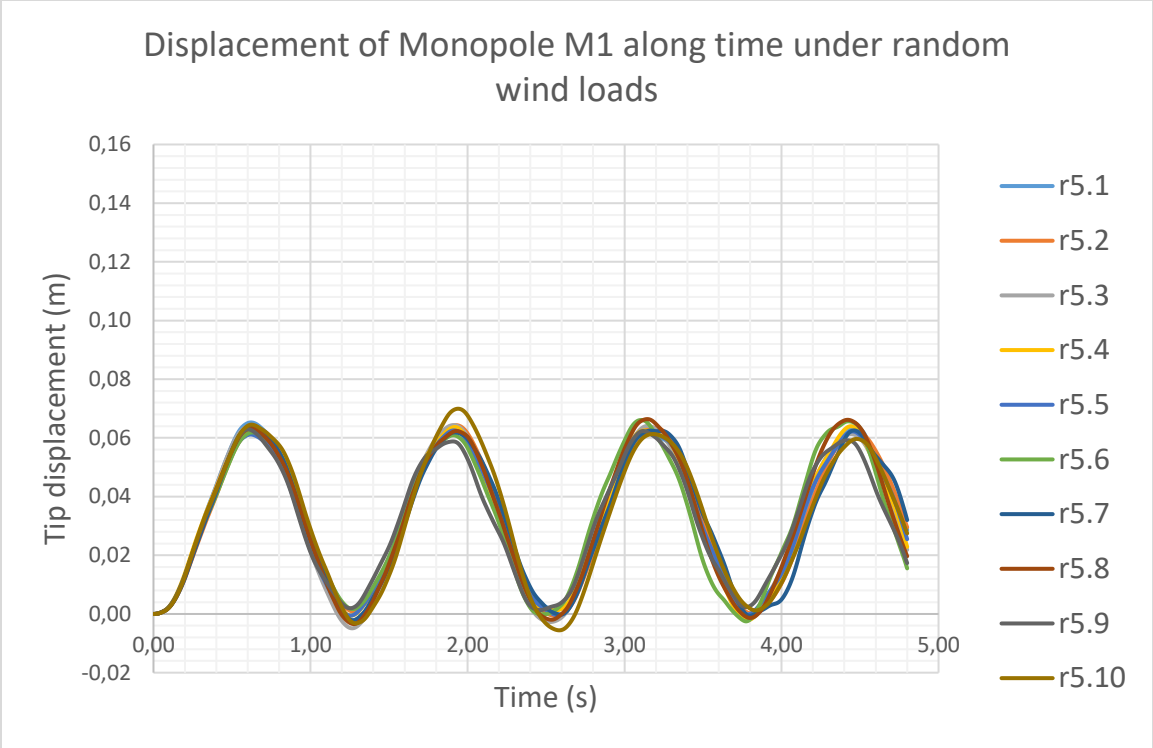

Figure A5: Horizontal tip displacement of Monopole M1 under random wind load time histories of mean value of 50% of maximum static load

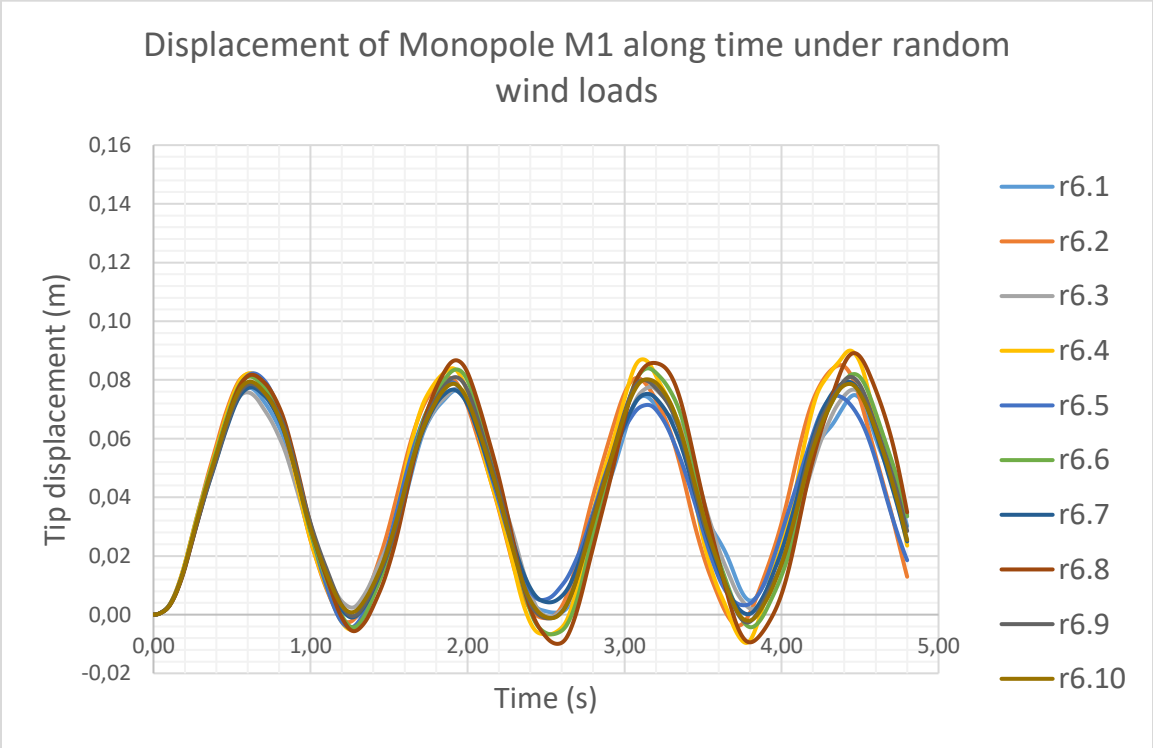

Figure A6: Horizontal tip displacement of Monopole M1 under random wind load time histories of mean value of 60% of maximum static load

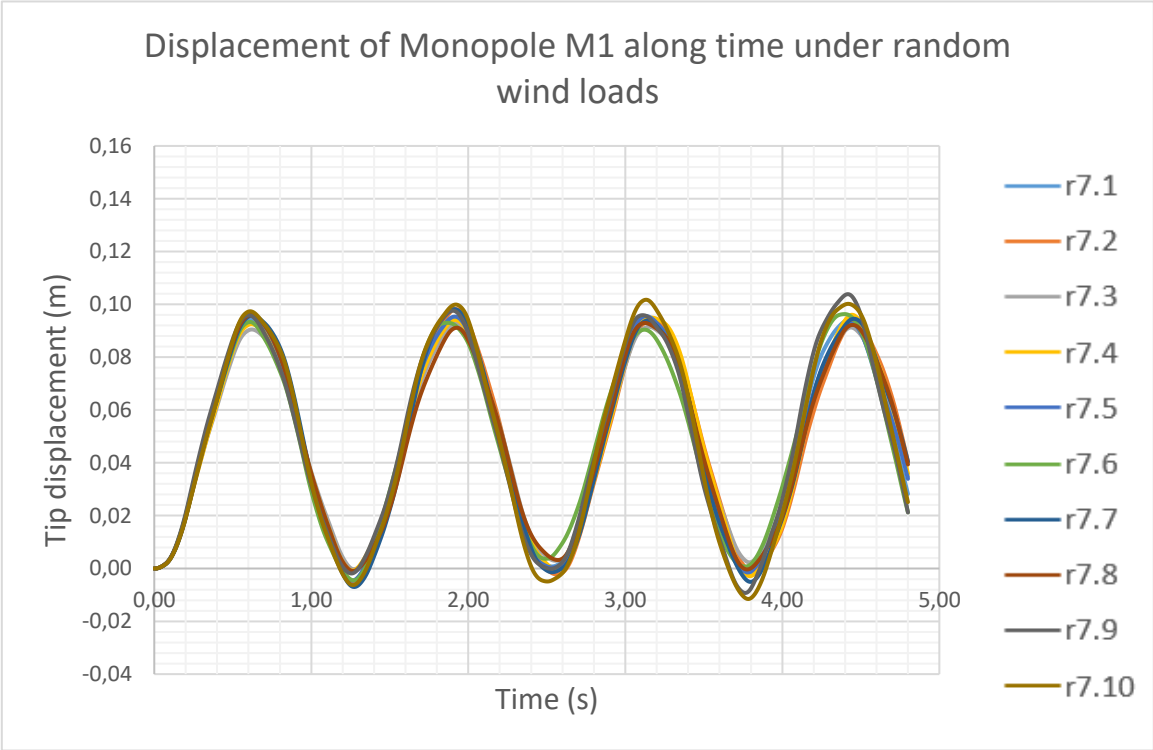

Figure A7: Horizontal tip displacement of Monopole M1 under random wind load time histories of mean value of 70% of maximum static load

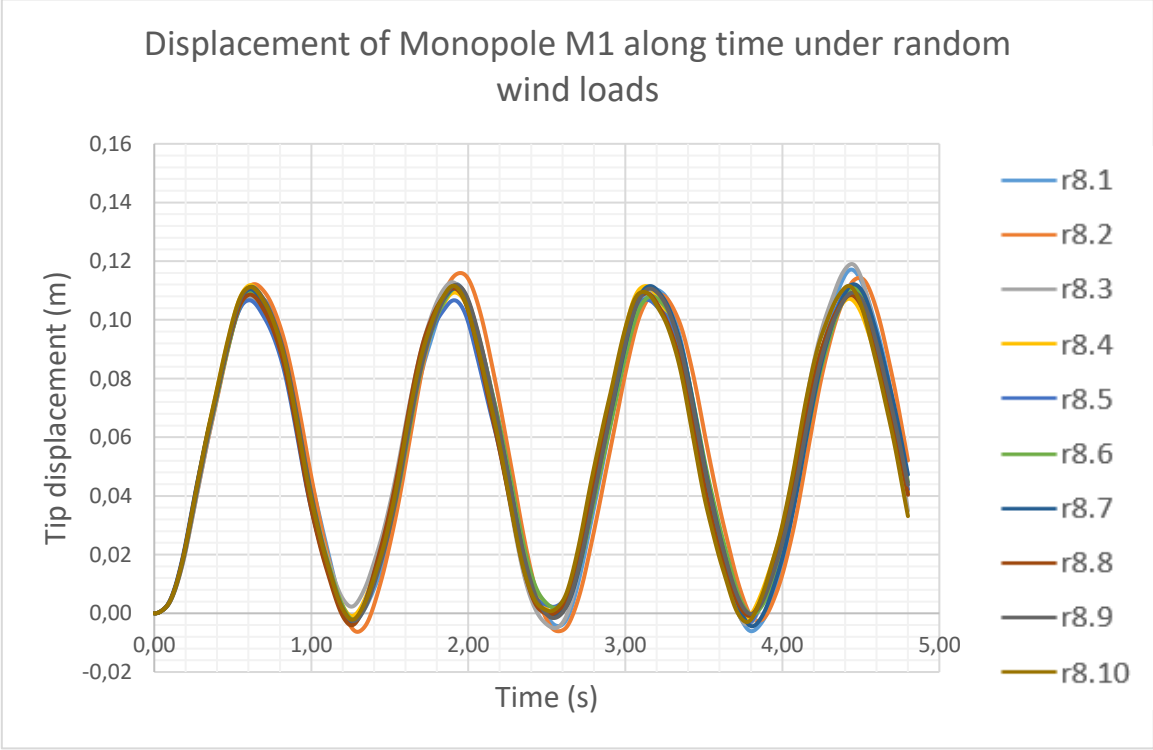

Figure A8: Horizontal tip displacement of Monopole M1 under random wind load time histories of mean value of 80% of maximum static load

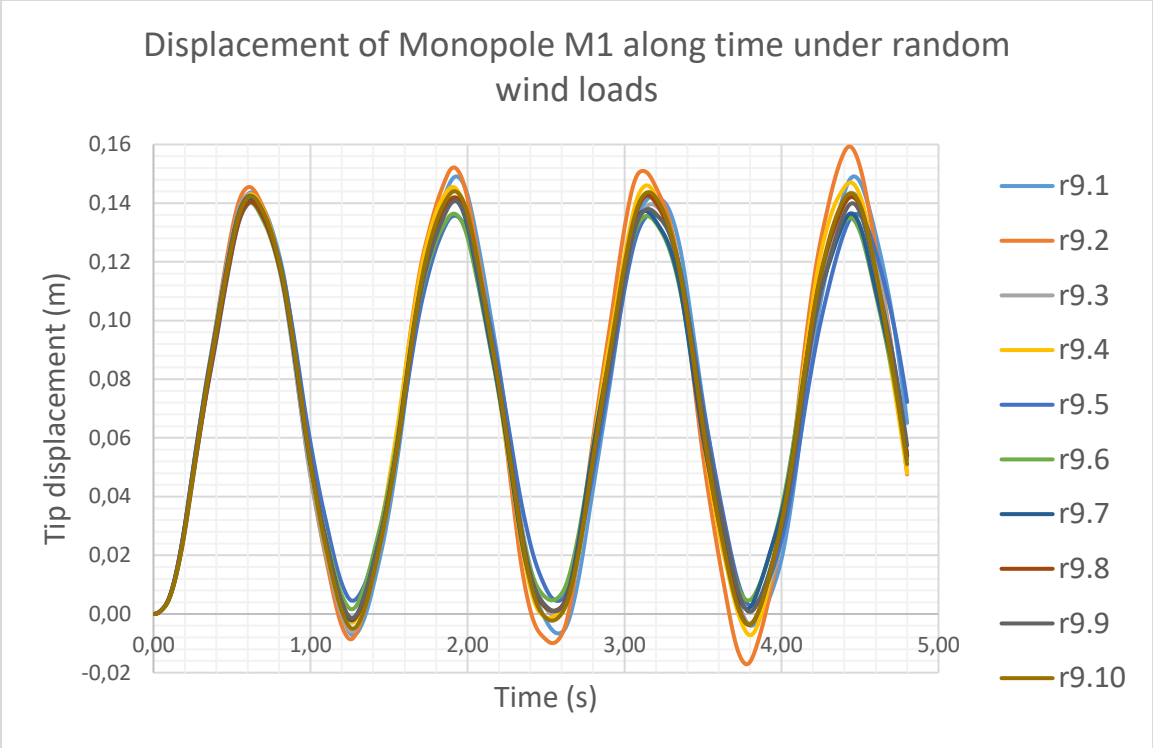

Figure A9: Horizontal tip displacement of Monopole M1 under random wind load time histories of mean value of 90% of maximum static load

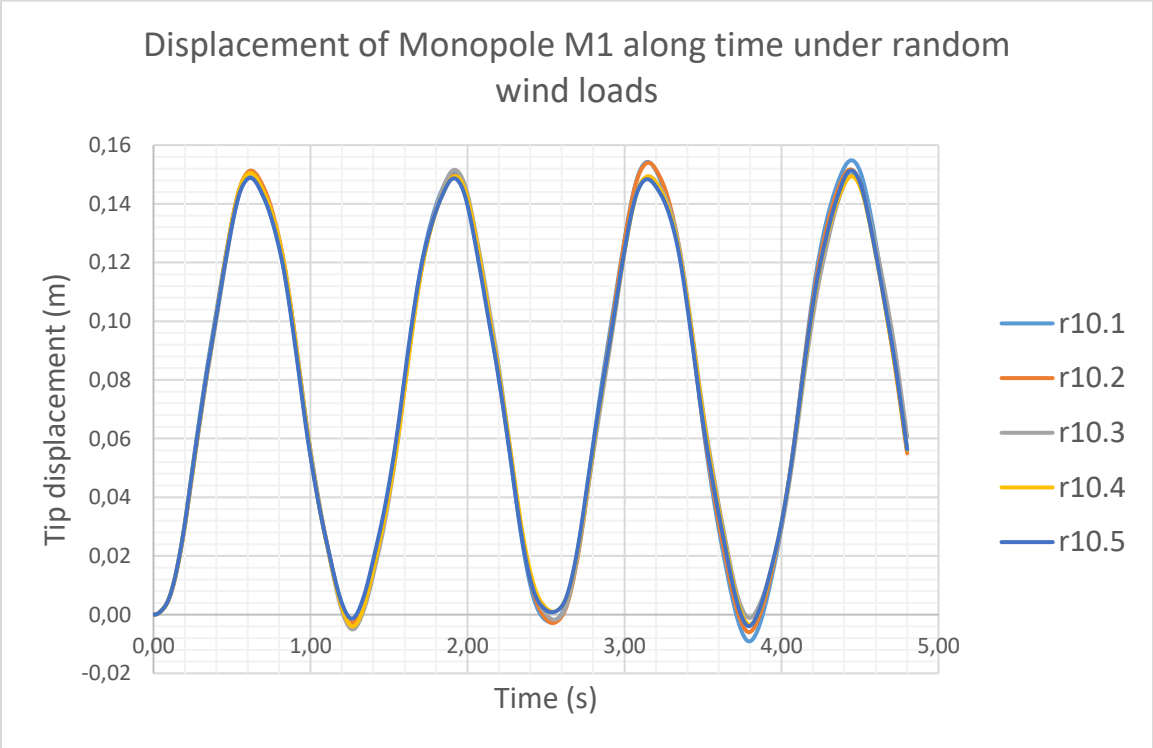

Figure A10: Horizontal tip displacement of Monopole M1 under random wind load time histories of mean value of 100% of maximum static load

Annex B: Results of Tower M2 under random wind time histories

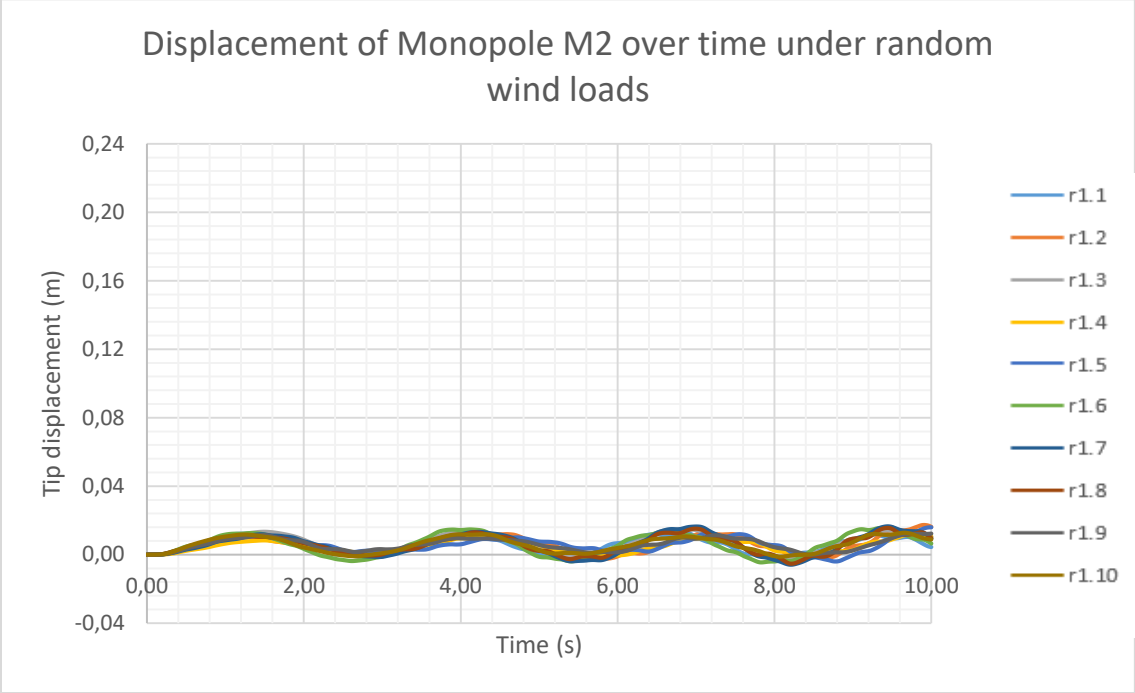

Figure B1: Horizontal tip displacement of Monopole M2 under random wind load time histories of mean value of 10% of maximum static load

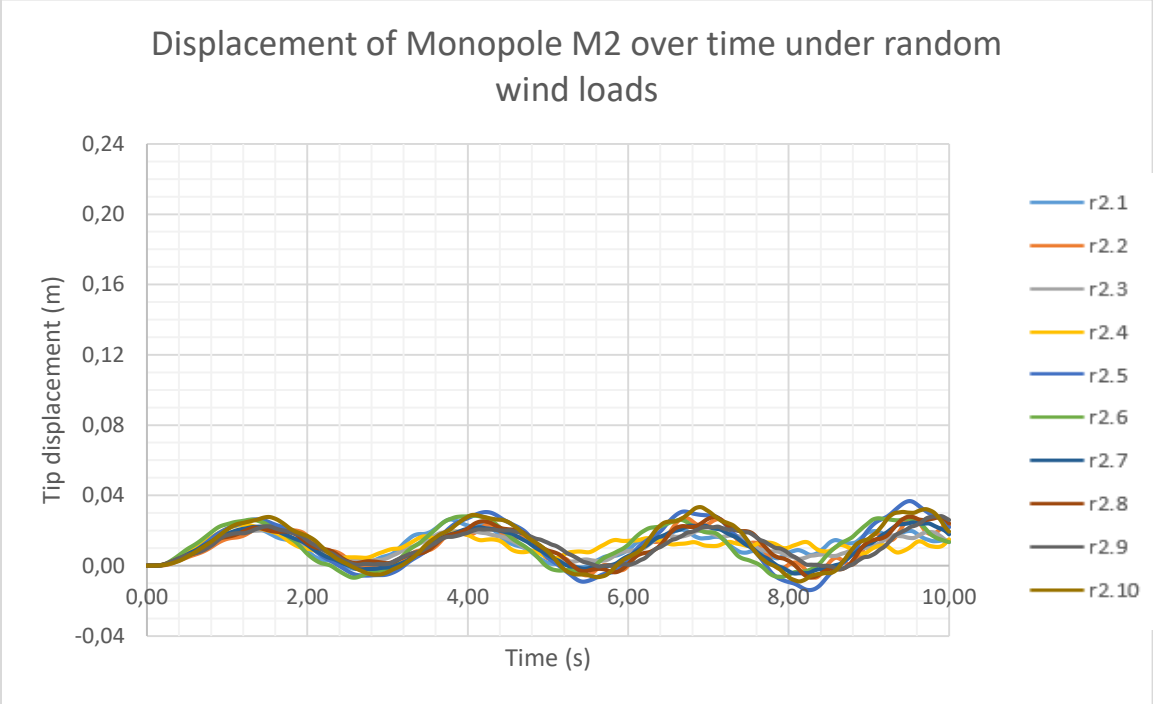

Figure B2: Horizontal tip displacement of Monopole M2 under random wind load time histories of mean value of 20% of maximum static load

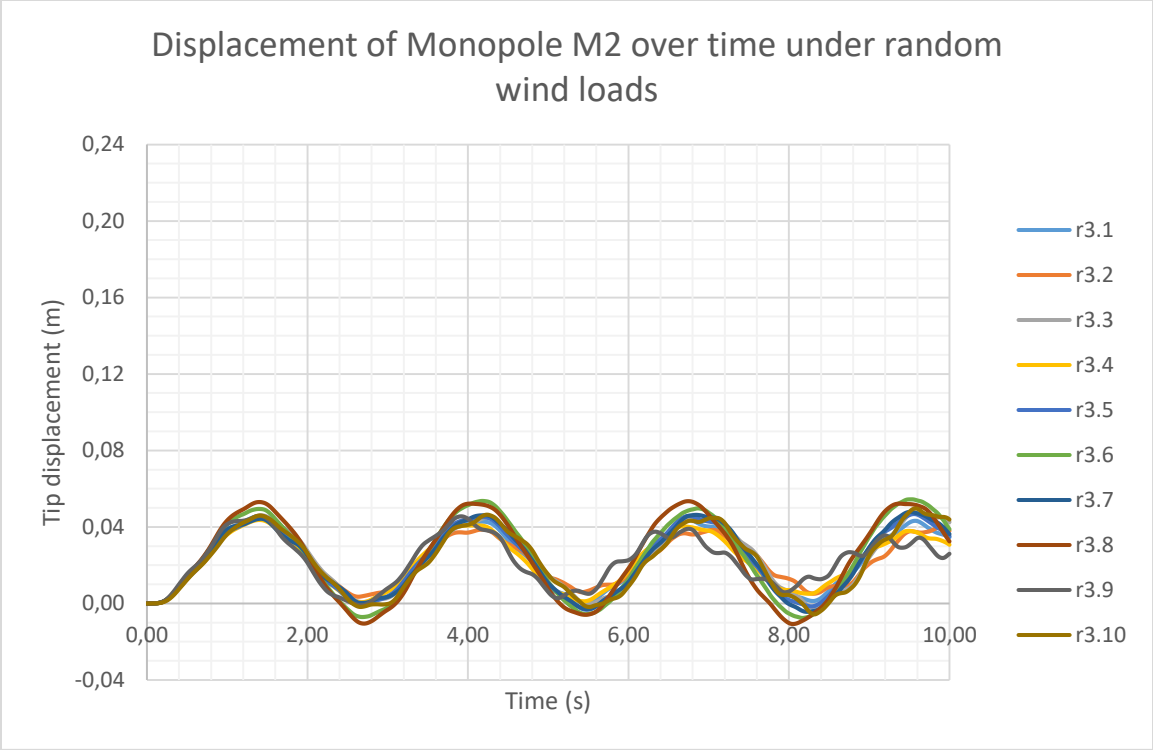

Figure B3: Horizontal tip displacement of Monopole M2 under random wind load time histories of mean value of 30% of maximum static load

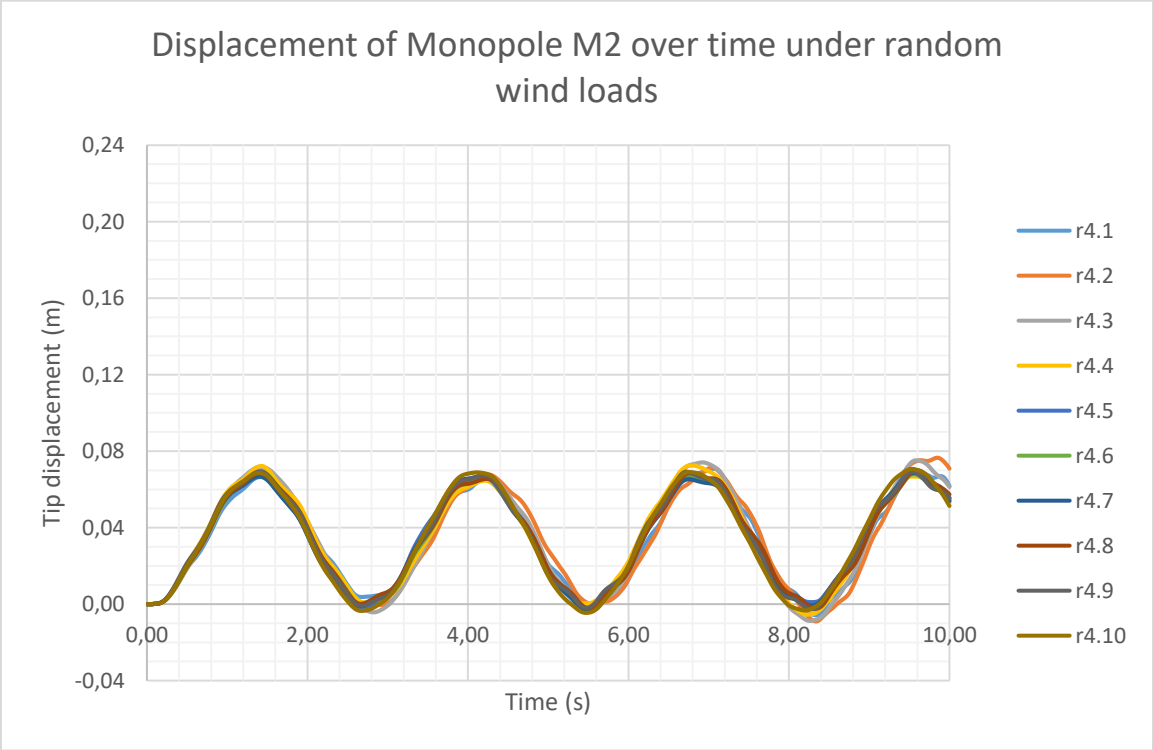

Figure B4: Horizontal tip displacement of Monopole M2 under random wind load time histories of mean value of 40% of maximum static load

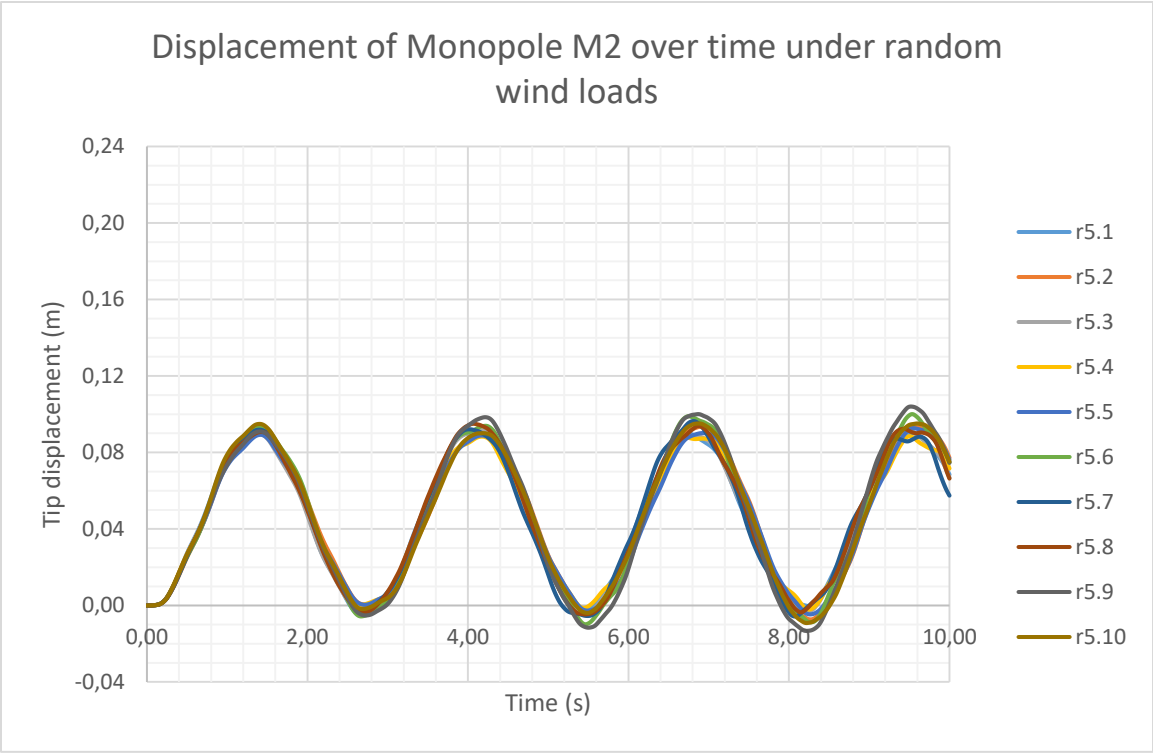

Figure B5: Horizontal tip displacement of Monopole M2 under random wind load time histories of mean value of 50% of maximum static load

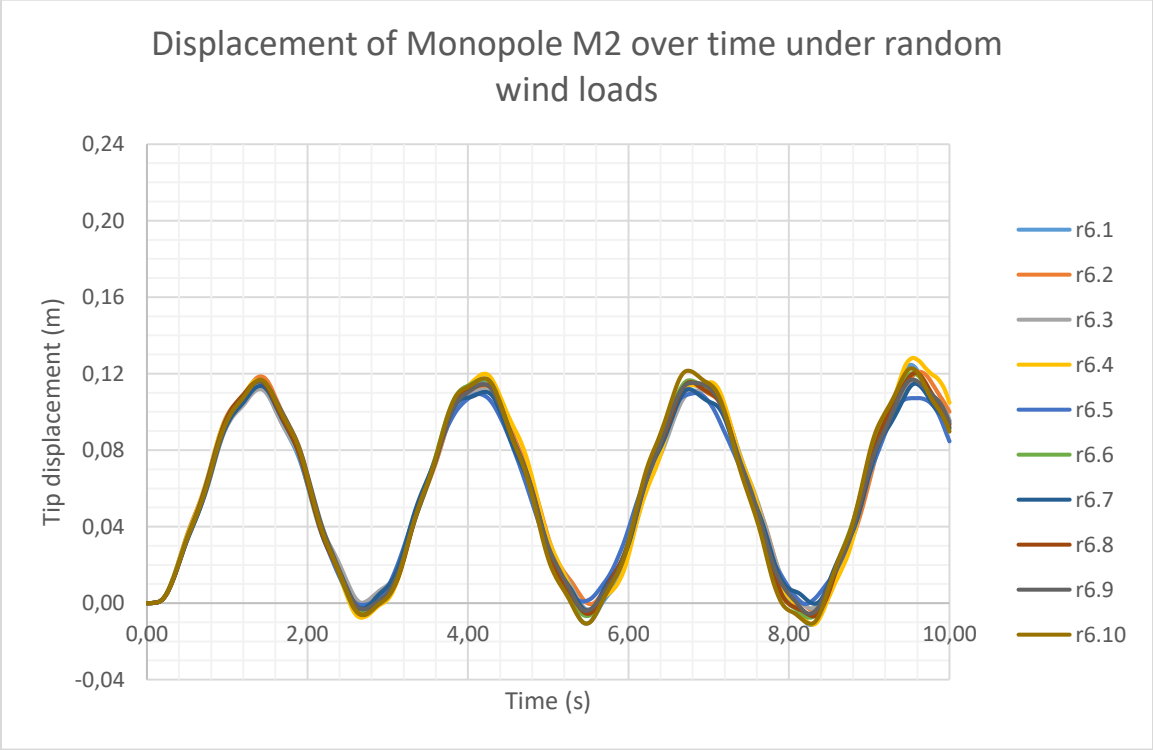

Figure B6: Horizontal tip displacement of Monopole M2 under random wind load time histories of mean value of 60% of maximum static load

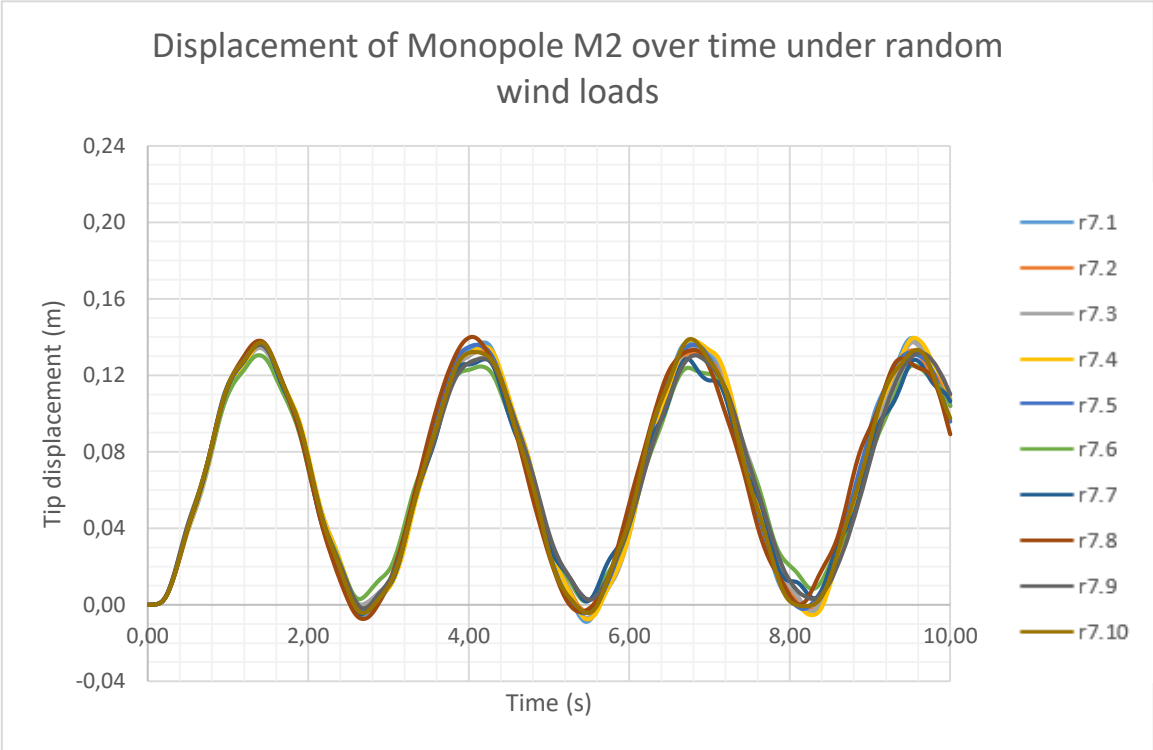

Figure B7: Horizontal tip displacement of Monopole M2 under random wind load time histories of mean value of 70% of maximum static load

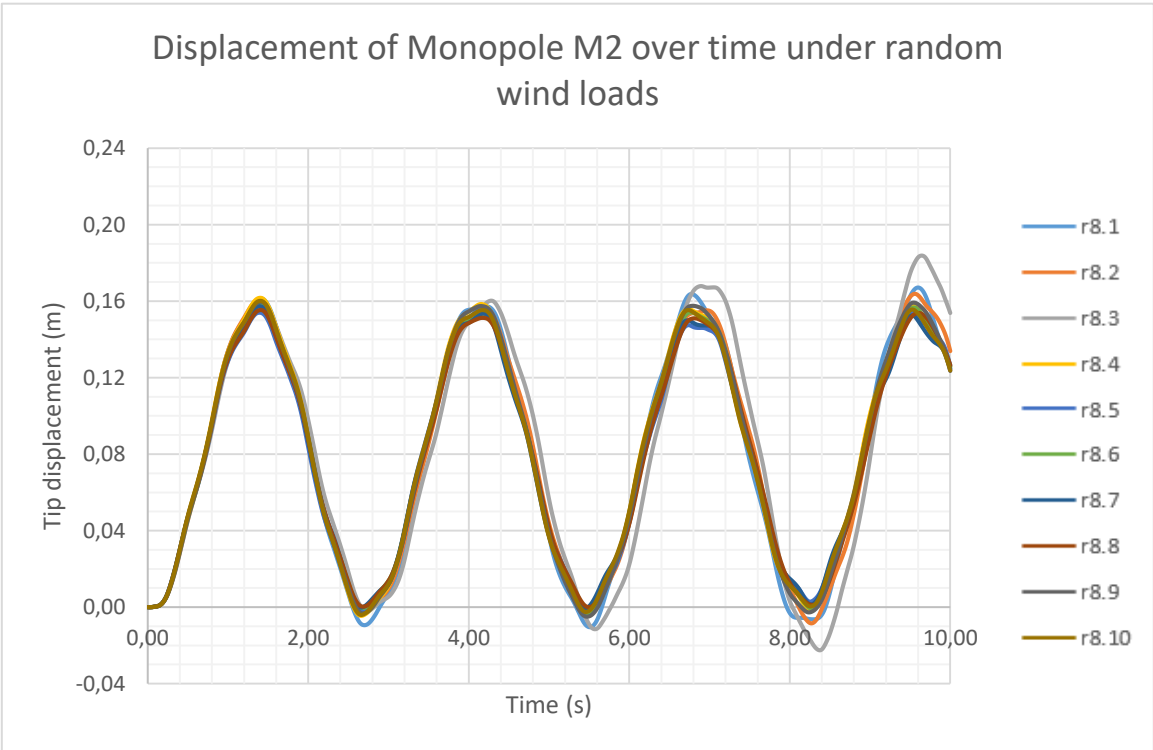

Figure B8: Horizontal tip displacement of Monopole M2 under random wind load time histories of mean value of 80% of maximum static load

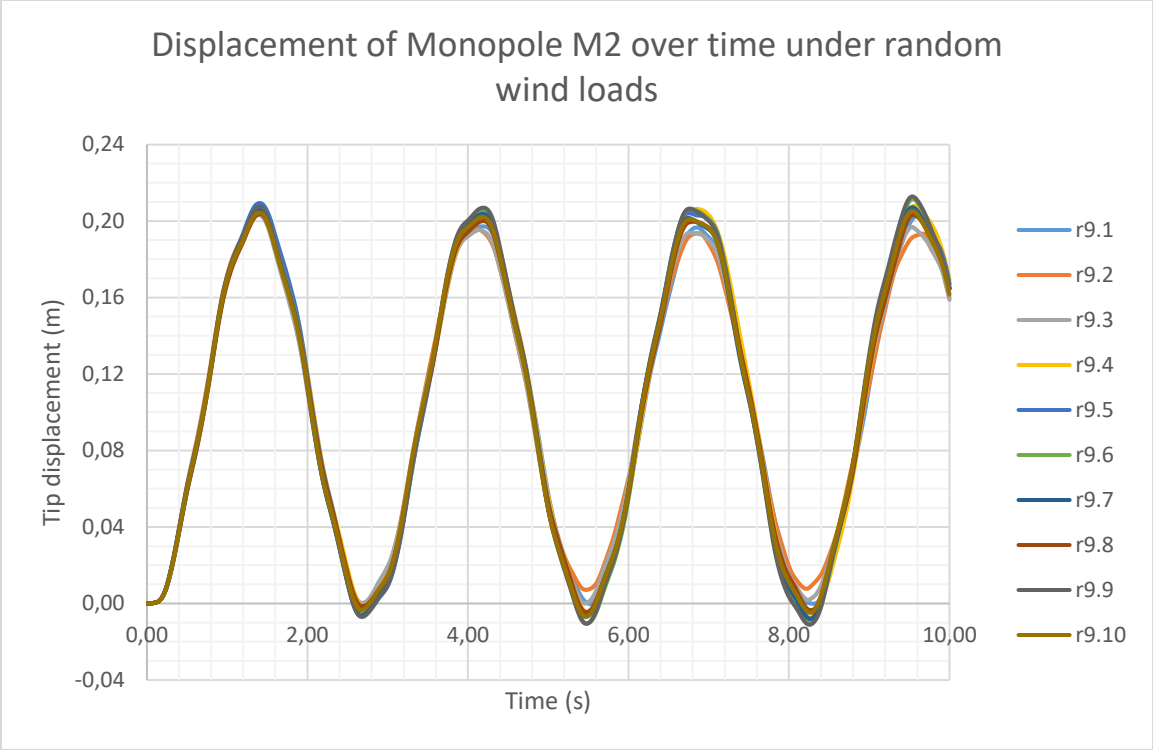

Figure B9: Horizontal tip displacement of Monopole M2 under random wind load time histories of mean value of 90% of maximum static load

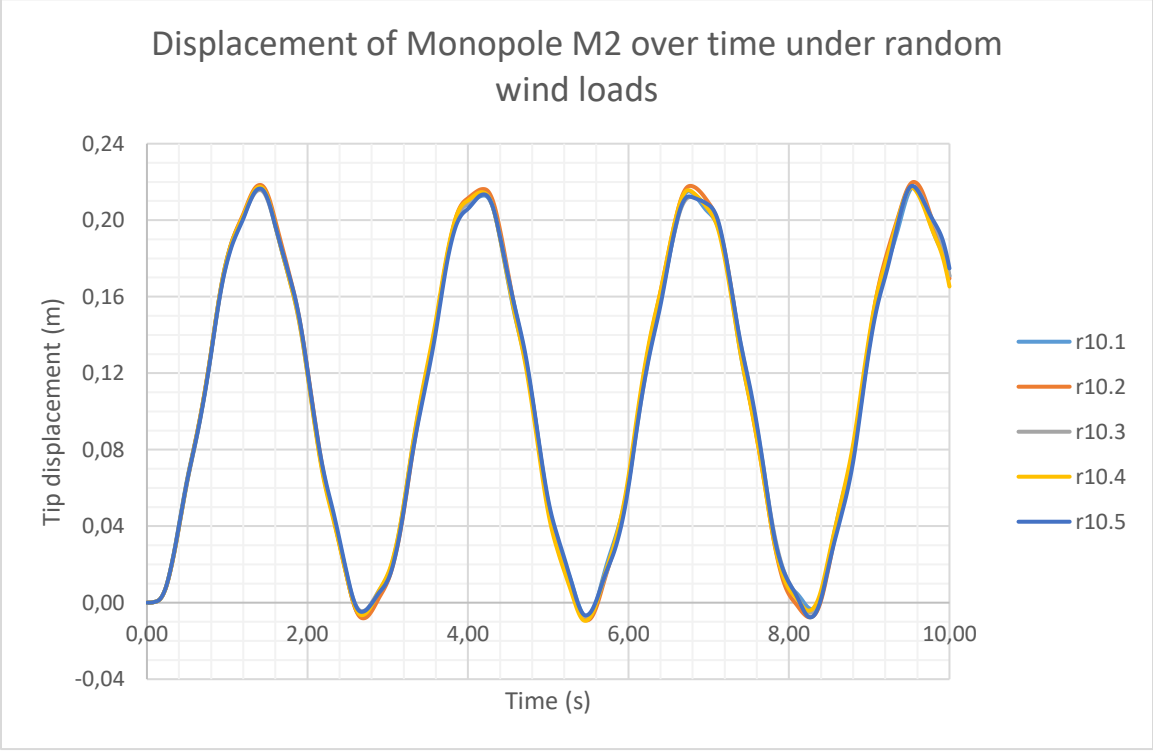

Figure B10: Horizontal tip displacement of Monopole M2 under random wind load time histories of mean value of 100% of maximum static load

Annex C: Results of the sign structure under random wind time histories

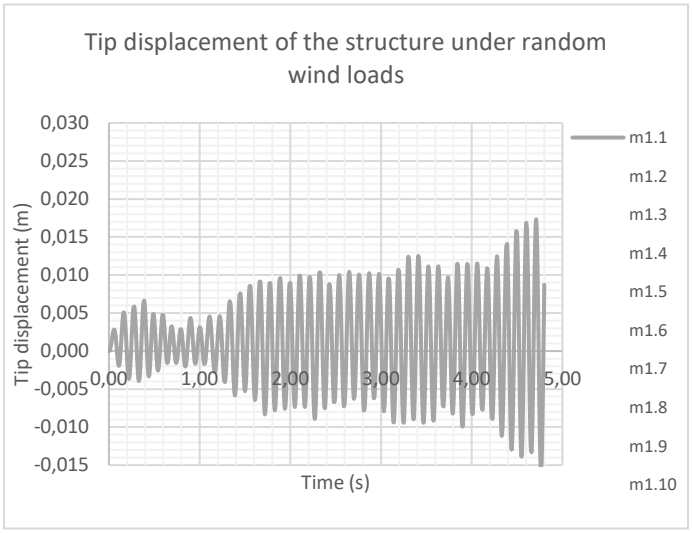

(a)

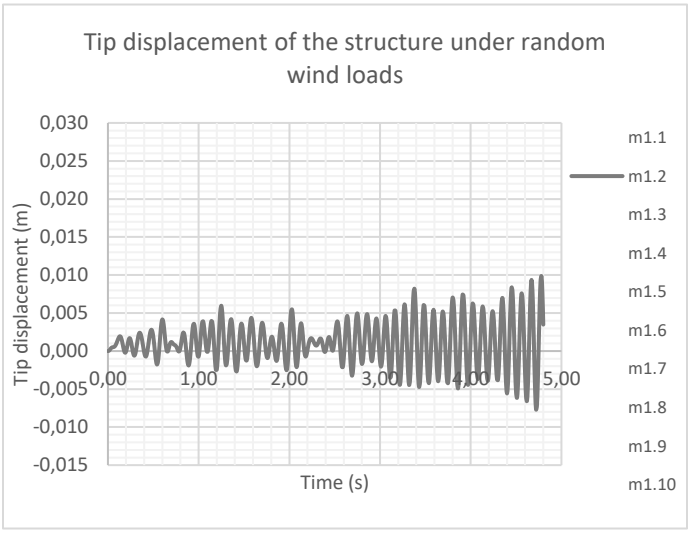

(b)

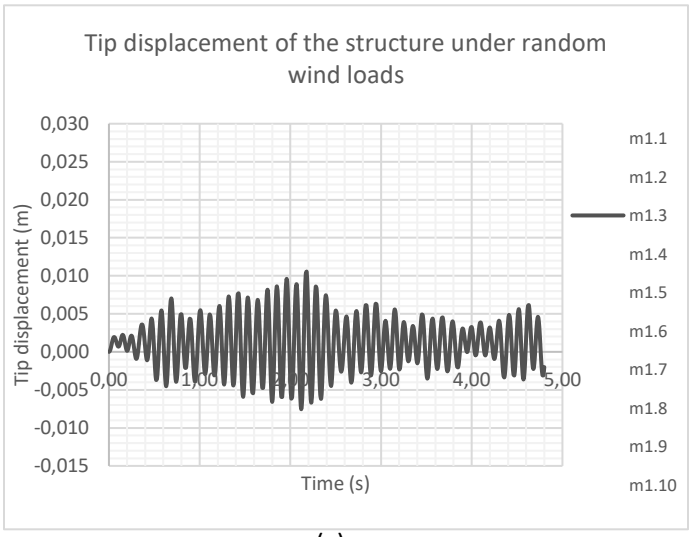

(c)

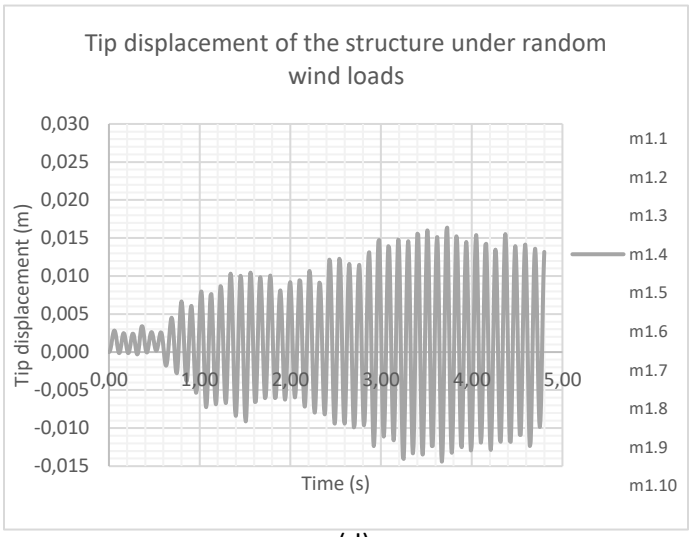

(d)

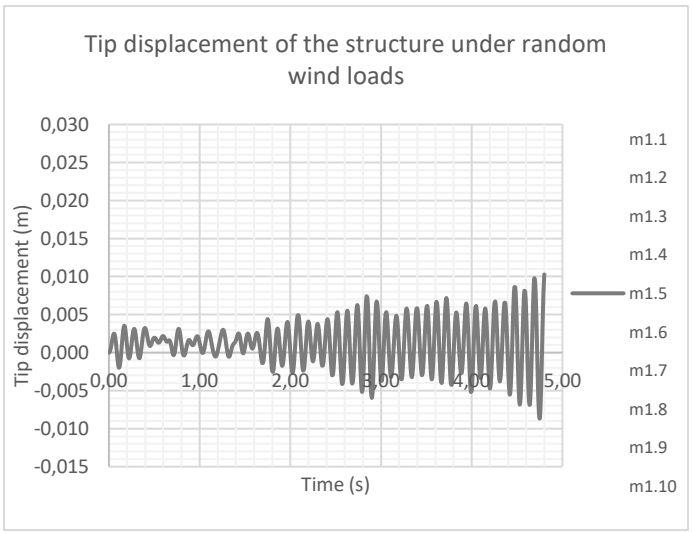

(e)

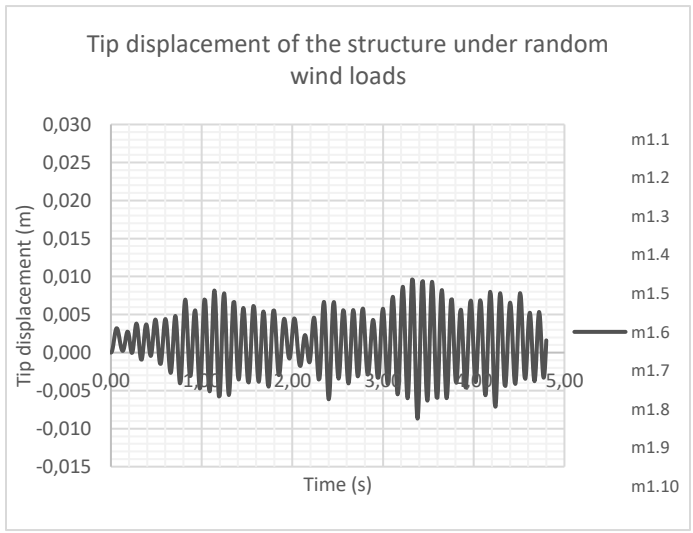

(f)

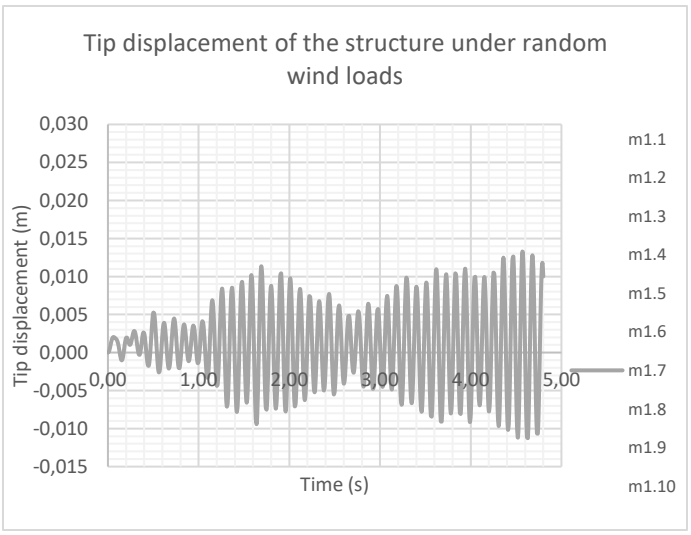

(g)

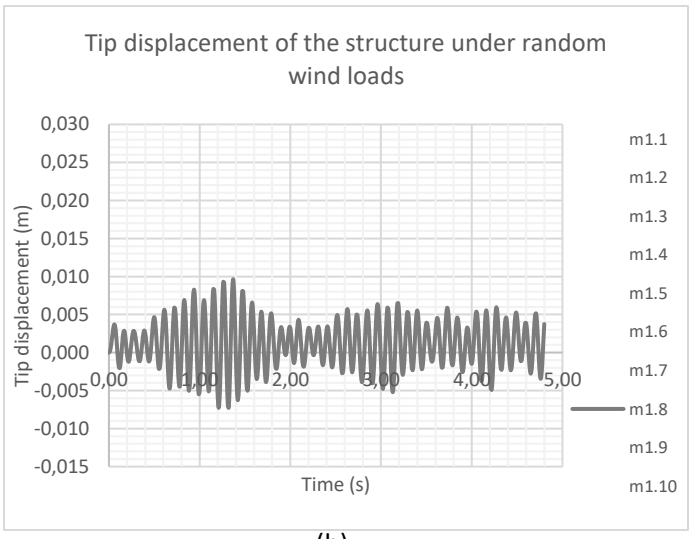

(h)

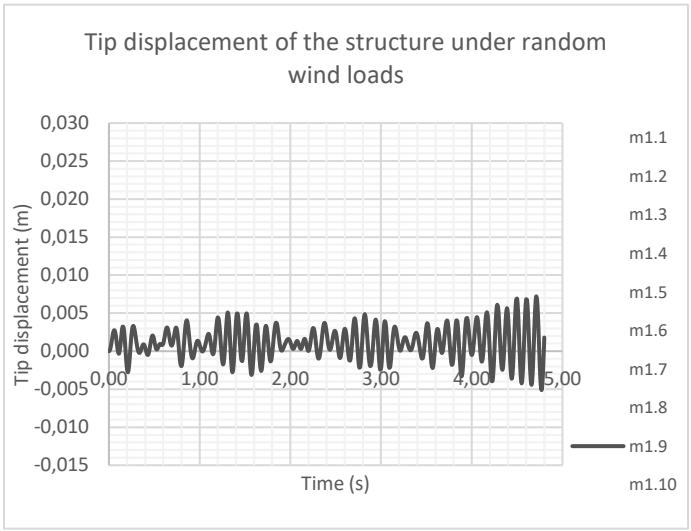

(i)

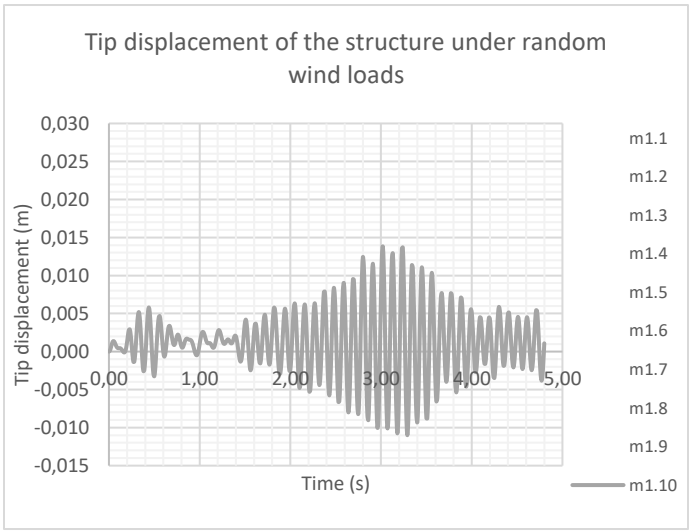

(j)

Figure C1: Horizontal tip displacement at the tip of the cantilevered arm under random wind load time histories of mean value of 10% of maximum static load (a)-(j).

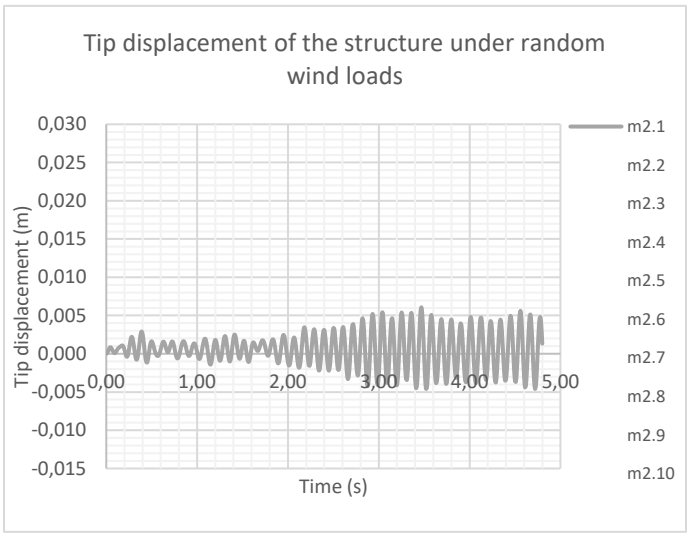
Tip displacement of the structure under random wind loads
Tip displacement (m)
0,030
0,025
0,020
0,015
0,010
0,005
0,000
-0,005
-0,010
-0,015
0,00
1,00
2,00
3,00
4,00
5,00
Time (s)
m2.1
m2.2
m2.3
m2.4
m2.5
m2.6
m2.7
m2.8
m2.9
m2.10

(a)

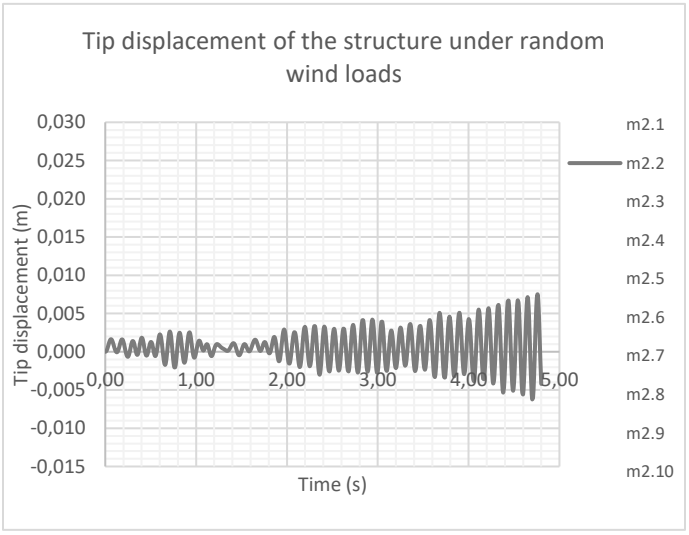
Tip displacement of the structure under random wind loads
Tip displacement (m)
0,030
0,025
0,020
0,015
0,010
0,005
0,000
-0,005
-0,010
-0,015
0,00
1,00
2,00
3,00
4,00
5,00
Time (s)
m2.1
m2.2
m2.3
m2.4
m2.5
m2.6
m2.7
m2.8
m2.9
m2.10

(b)

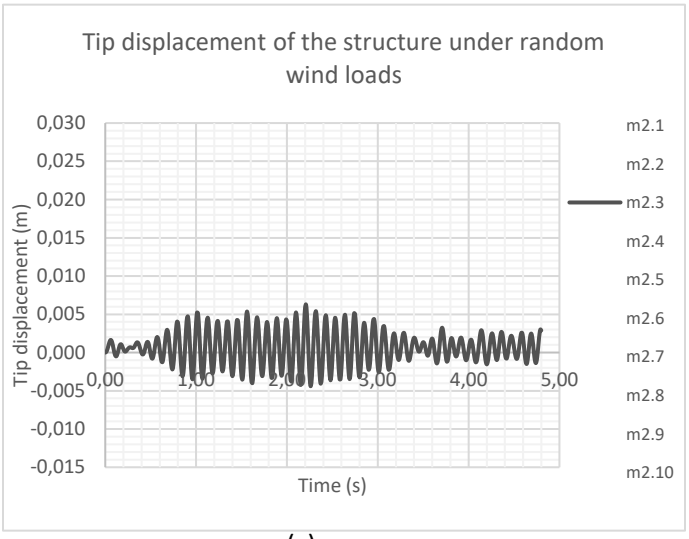
Tip displacement of the structure under random wind loads
Tip displacement (m)
0,030
0,025
0,020
0,015
0,010
0,005
0,000
-0,005
-0,010
-0,015
0,00
1,00
2,00
3,00
4,00
5,00
Time (s)
m2.1
m2.2
m2.3
m2.4
m2.5
m2.6
m2.7
m2.8
m2.9
m2.10

(c)

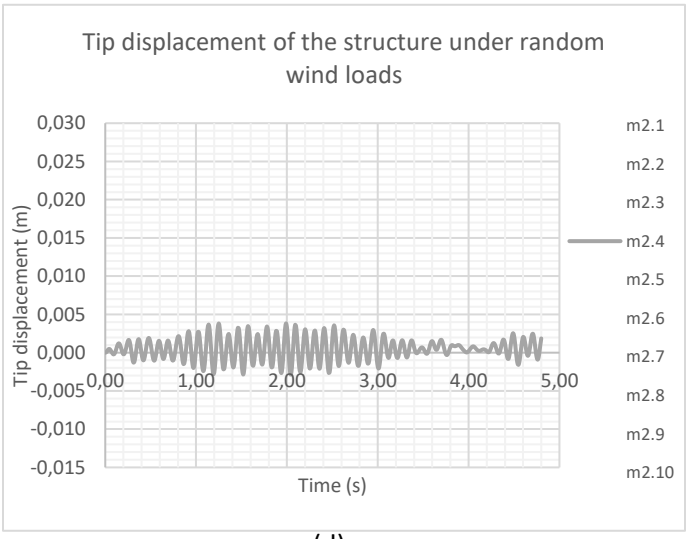
Tip displacement of the structure under random wind loads
Tip displacement (m)
0,030
0,025
0,020
0,015
0,010
0,005
0,000
-0,005
-0,010
-0,015
0,00
1,00
2,00
3,00
4,00
5,00
Time (s)
m2.1
m2.2
m2.3
m2.4
m2.5
m2.6
m2.7
m2.8
m2.9
m2.10

(d)

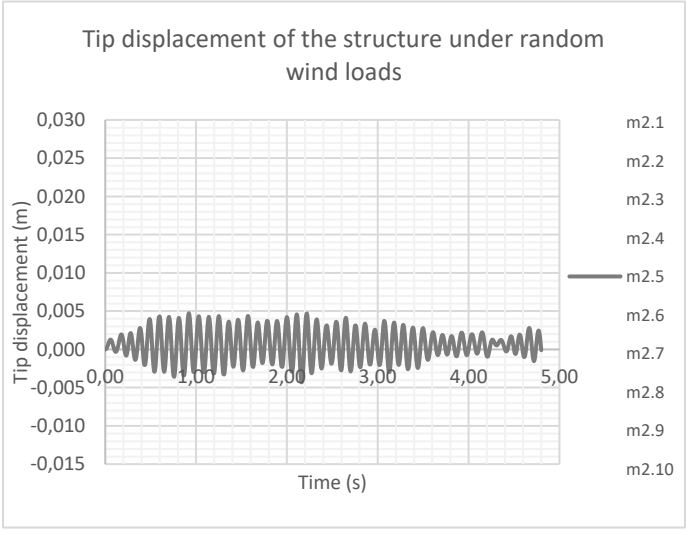
Tip displacement of the structure under random wind loads
Tip displacement (m)
0,030
0,025
0,020
0,015
0,010
0,005
0,000
-0,005
-0,010
-0,015
0,00
1,00
2,00
3,00
4,00
5,00
Time (s)
m2.1
m2.2
m2.3
m2.4
m2.5
m2.6
m2.7
m2.8
m2.9
m2.10

(e)

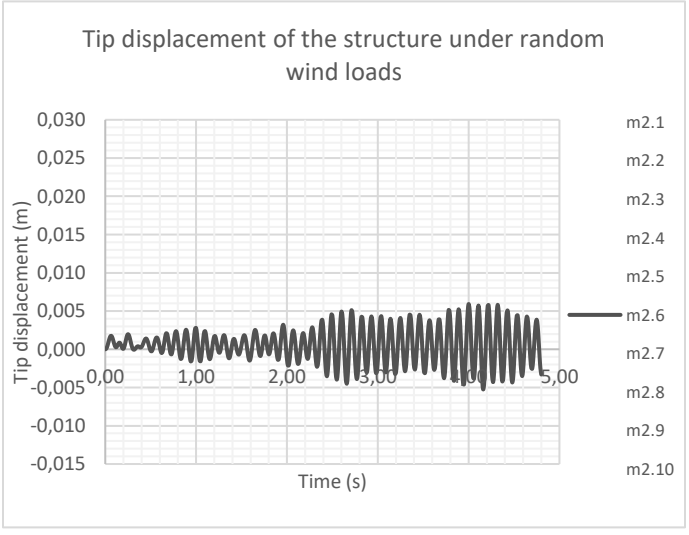
Tip displacement of the structure under random wind loads
Tip displacement (m)
0,030
0,025
0,020
0,015
0,010
0,005
0,000
-0,005
-0,010
-0,015
0,00
1,00
2,00
3,00
4,00
5,00
Time (s)
m2.1
m2.2
m2.3
m2.4
m2.5
m2.6
m2.7
m2.8
m2.9
m2.10

(f)

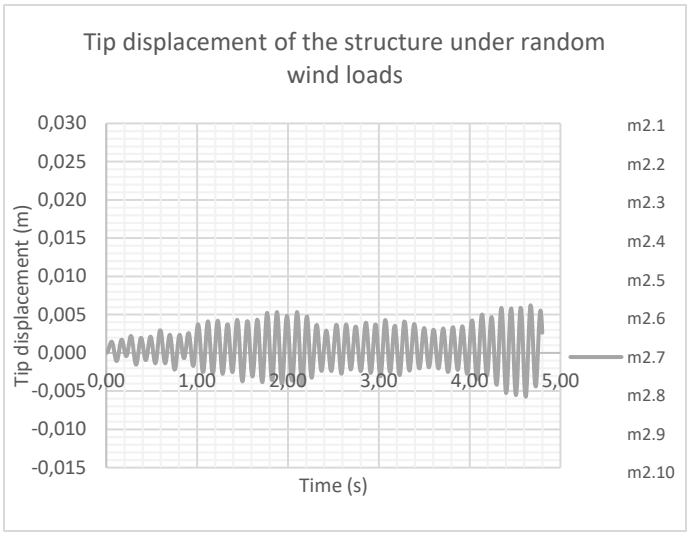

(g)

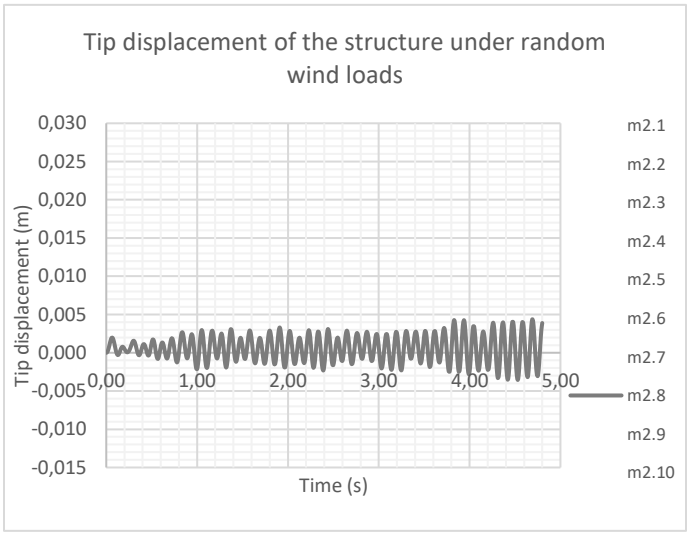

(h)

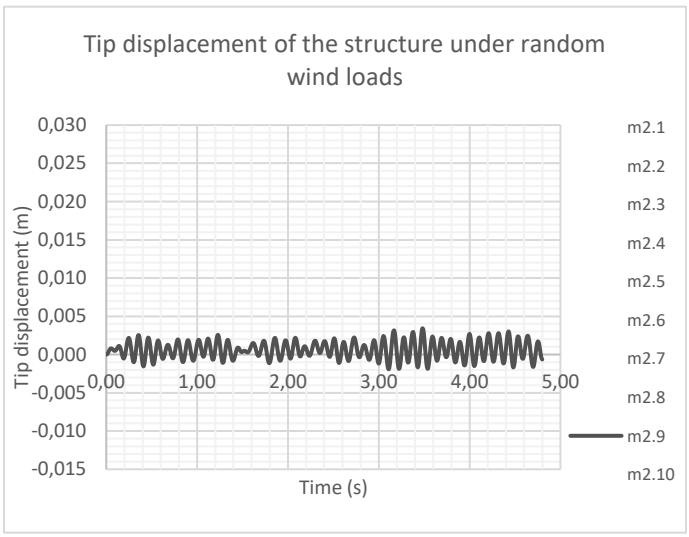

(i)

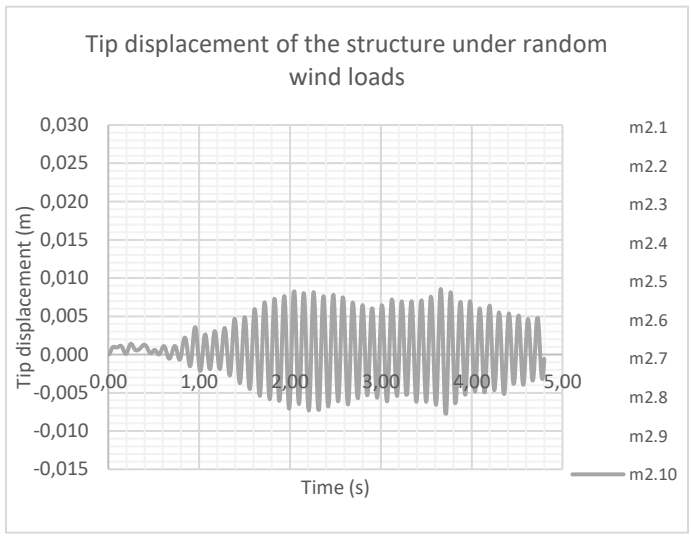

(j)

Figure C2: Horizontal tip displacement at the tip of the cantilevered arm under random wind load time histories of mean value of 20% of maximum static load (a)-(j).

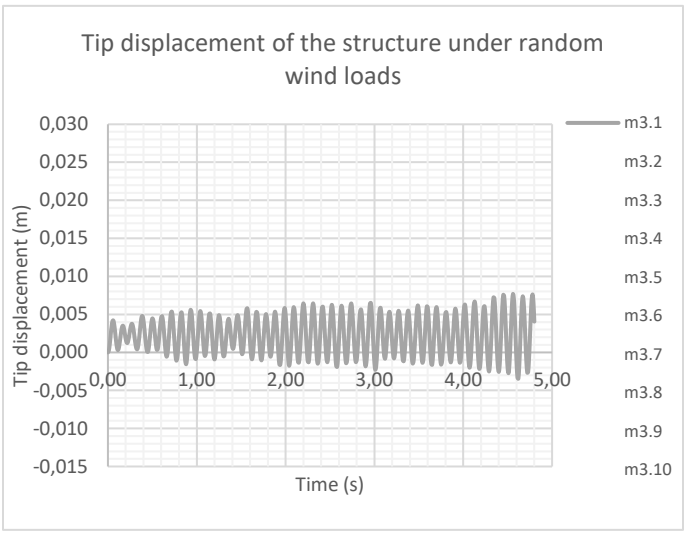
Tip displacement of the structure under random wind loads
Tip displacement (m)
0,030
0,025
0,020
0,015
0,010
0,005
0,000
-0,005
-0,010
-0,015
0,00
1,00
2,00
3,00
4,00
5,00
Time (s)
m3.1
m3.2
m3.3
m3.4
m3.5
m3.6
m3.7
m3.8
m3.9
m3.10

(a)

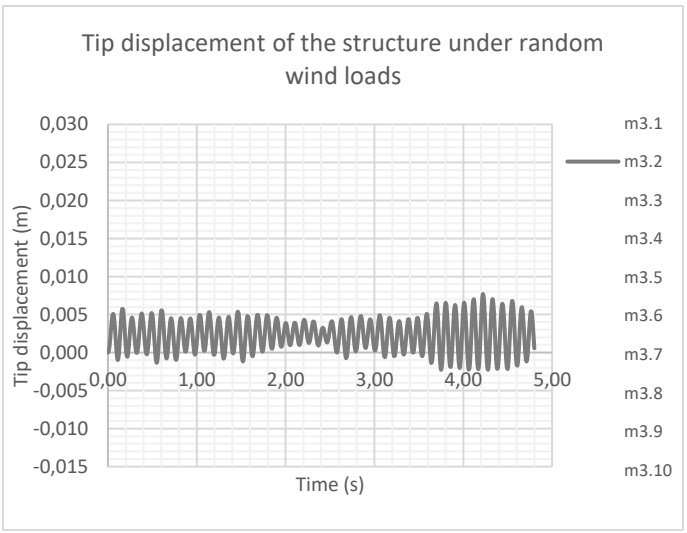
Tip displacement of the structure under random wind loads
Tip displacement (m)
0,030
0,025
0,020
0,015
0,010
0,005
0,000
-0,005
-0,010
-0,015
0,00
1,00
2,00
3,00
4,00
5,00
Time (s)
m3.1
m3.2
m3.3
m3.4
m3.5
m3.6
m3.7
m3.8
m3.9
m3.10

(b)

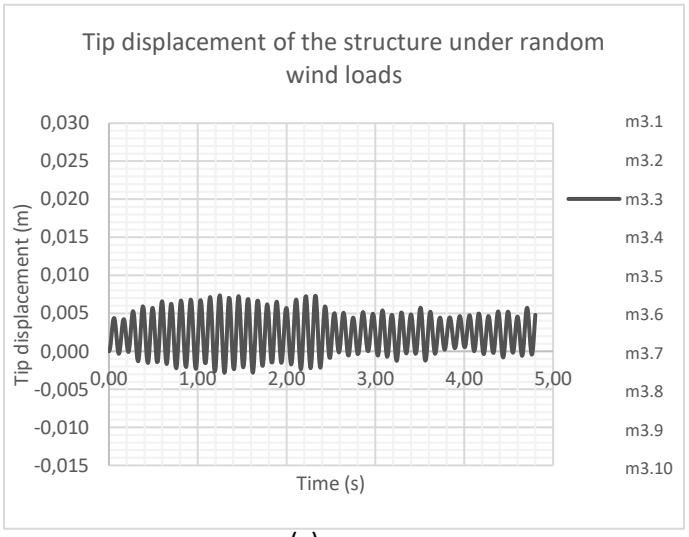
Tip displacement of the structure under random wind loads
Tip displacement (m)
0,030
0,025
0,020
0,015
0,010
0,005
0,000
-0,005
-0,010
-0,015
0,00
1,00
2,00
3,00
4,00
5,00
Time (s)
m3.1
m3.2
m3.3
m3.4
m3.5
m3.6
m3.7
m3.8
m3.9
m3.10

(c)

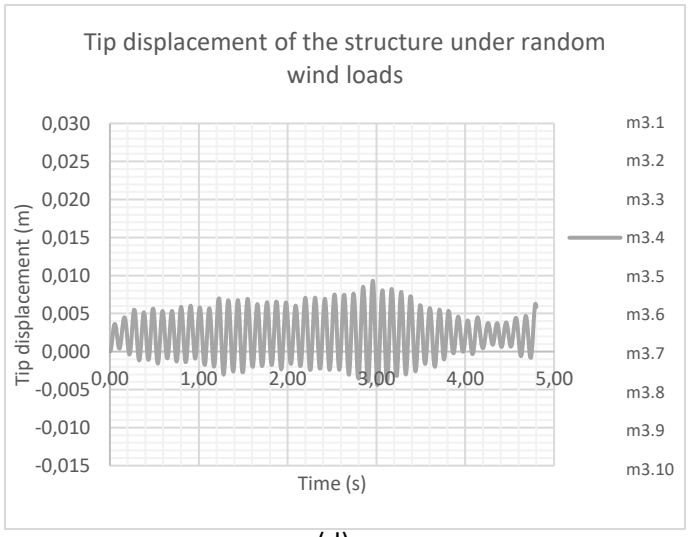
Tip displacement of the structure under random wind loads
Tip displacement (m)
0,030
0,025
0,020
0,015
0,010
0,005
0,000
-0,005
-0,010
-0,015
0,00
1,00
2,00
3,00
4,00
5,00
Time (s)
m3.1
m3.2
m3.3
m3.4
m3.5
m3.6
m3.7
m3.8
m3.9
m3.10

(d)

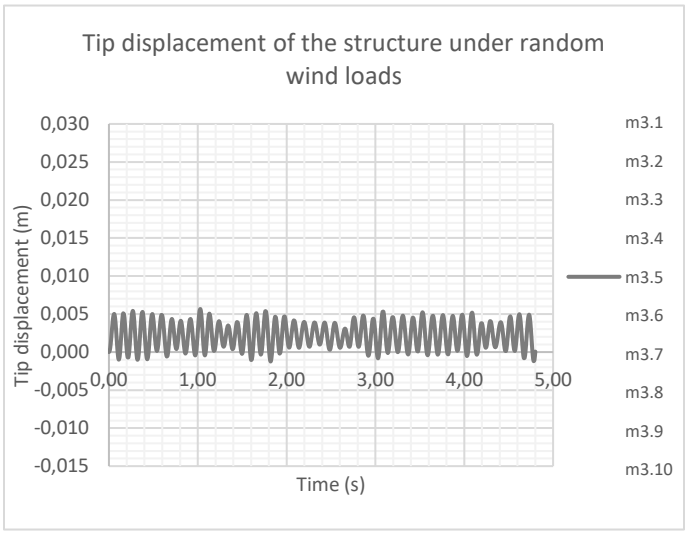
Tip displacement of the structure under random wind loads
Tip displacement (m)
0,030
0,025
0,020
0,015
0,010
0,005
0,000
-0,005
-0,010
-0,015
0,00
1,00
2,00
3,00
4,00
5,00
Time (s)
m3.1
m3.2
m3.3
m3.4
m3.5
m3.6
m3.7
m3.8
m3.9
m3.10

(e)

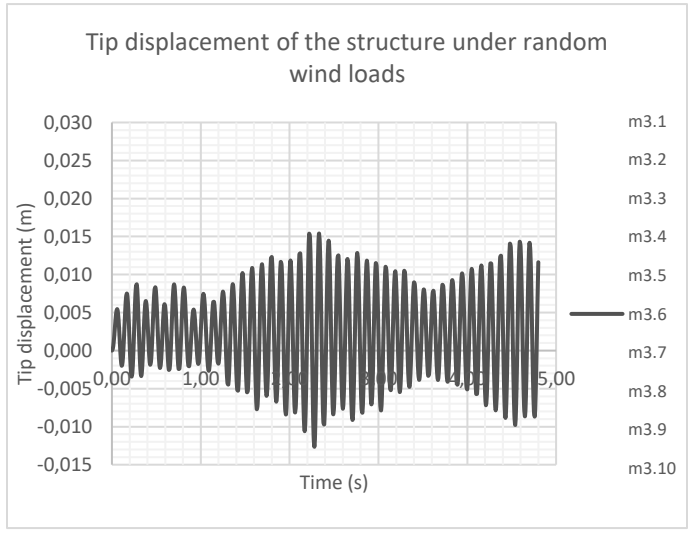
Tip displacement of the structure under random wind loads
Tip displacement (m)
0,030
0,025
0,020
0,015
0,010
0,005
0,000
-0,005
-0,010
-0,015
0,00
1,00
5,00
Time (s)
m3.1
m3.2
m3.3
m3.4
m3.5
m3.6
m3.7
m3.8
m3.9
m3.10

(f)

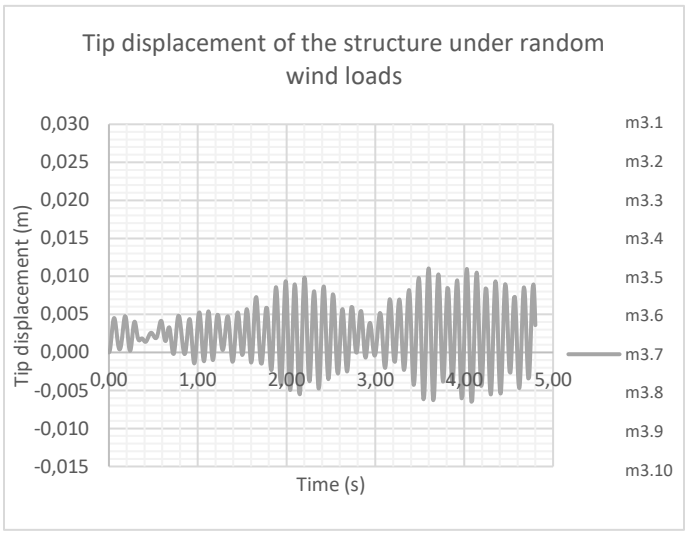

(g)

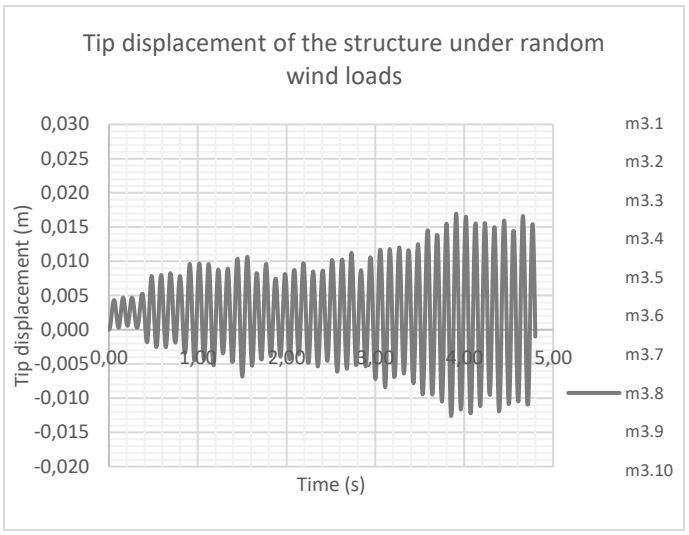

(h)

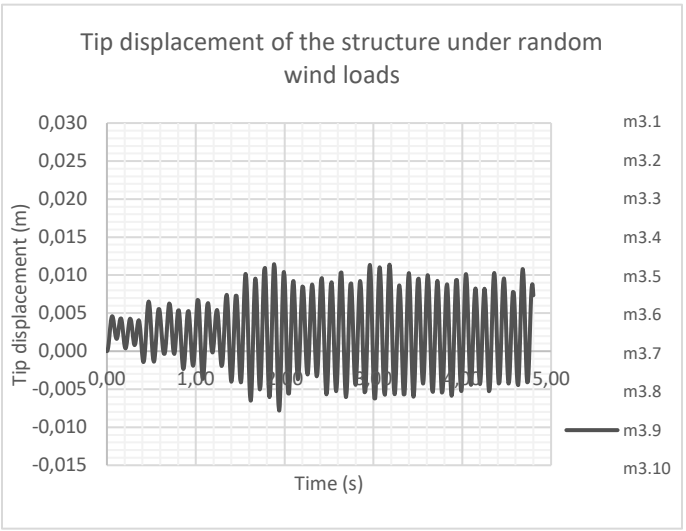

(i)

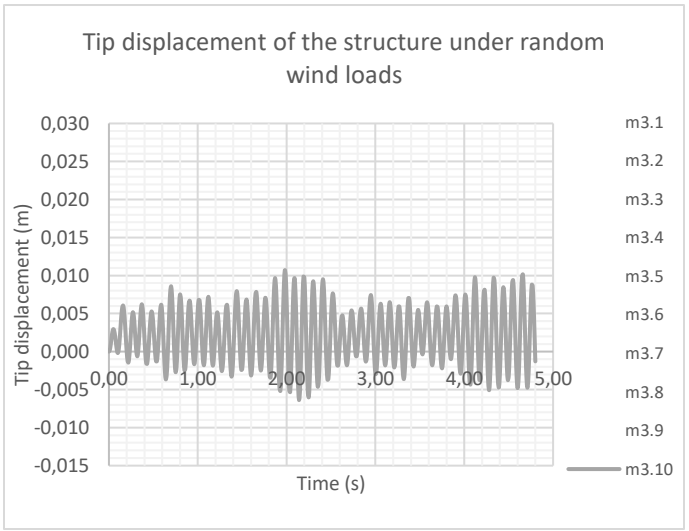

(j)

Figure C3: Horizontal tip displacement at the tip of the cantilevered arm under random wind load time histories of mean value of 30% of maximum static load (a)-(j).

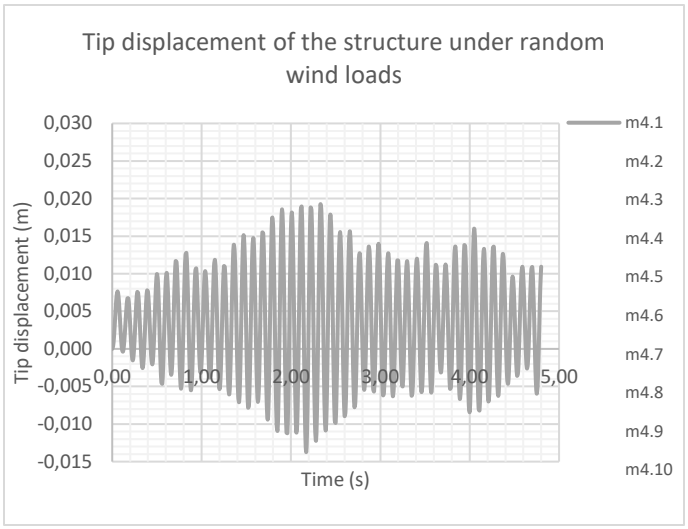
Tip displacement of the structure under random wind loads
Tip displacement (m)
0,030
0,025
0,020
0,015
0,010
0,005
0,000
-0,005
-0,010
-0,015
0,00
1,00
2,00
3,00
4,00
5,00
Time (s)
m4.1
m4.2
m4.3
m4.4
m4.5
m4.6
m4.7
m4.8
m4.9
m4.10

(a)

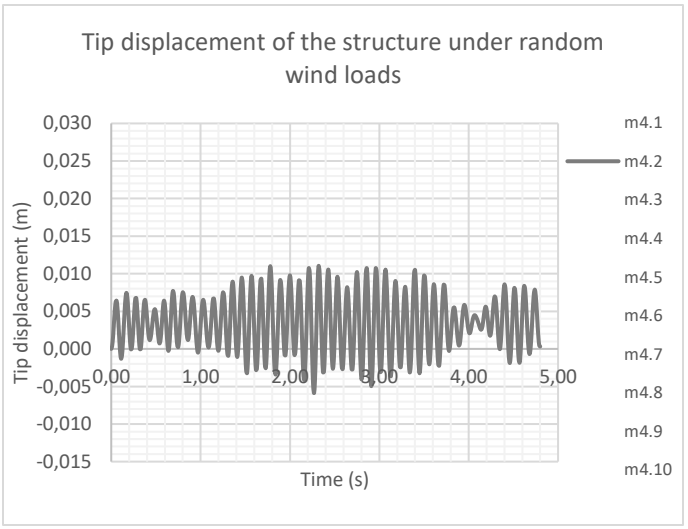
Tip displacement of the structure under random wind loads
Tip displacement (m)
0,030
0,025
0,020
0,015
0,010
0,005
0,000
-0,005
-0,010
-0,015
0,00
1,00
2,00
3,00
4,00
5,00
Time (s)
m4.1
m4.2
m4.3
m4.4
m4.5
m4.6
m4.7
m4.8
m4.9
m4.10

(b)

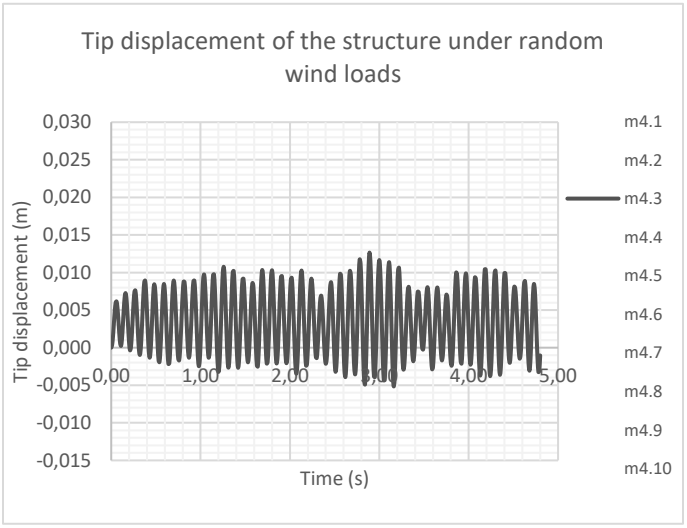
Tip displacement of the structure under random wind loads
Tip displacement (m)
0,030
0,025
0,020
0,015
0,010
0,005
0,000
-0,005
-0,010
-0,015
0,00
1,00
2,00
3,00
4,00
5,00
Time (s)
m4.1
m4.2
m4.3
m4.4
m4.5
m4.6
m4.7
m4.8
m4.9
m4.10

(c)

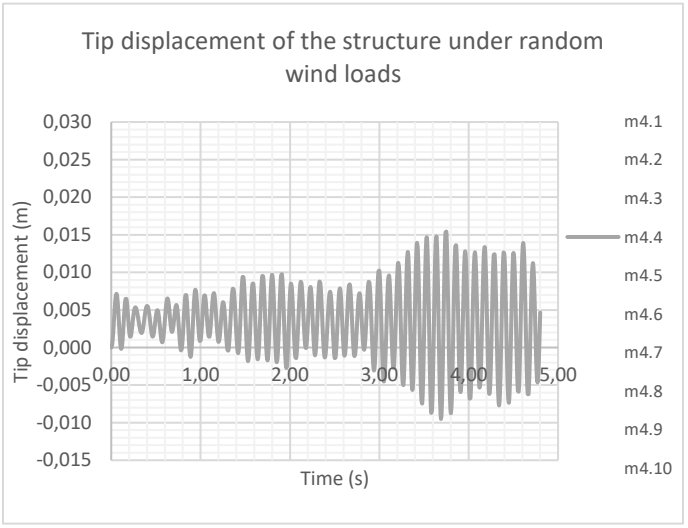
Tip displacement of the structure under random wind loads
Tip displacement (m)
0,030
0,025
0,020
0,015
0,010
0,005
0,000
-0,005
-0,010
-0,015
0,00
1,00
2,00
3,00
4,00
5,00
Time (s)
m4.1
m4.2
m4.3
m4.4
m4.5
m4.6
m4.7
m4.8
m4.9
m4.10

(d)

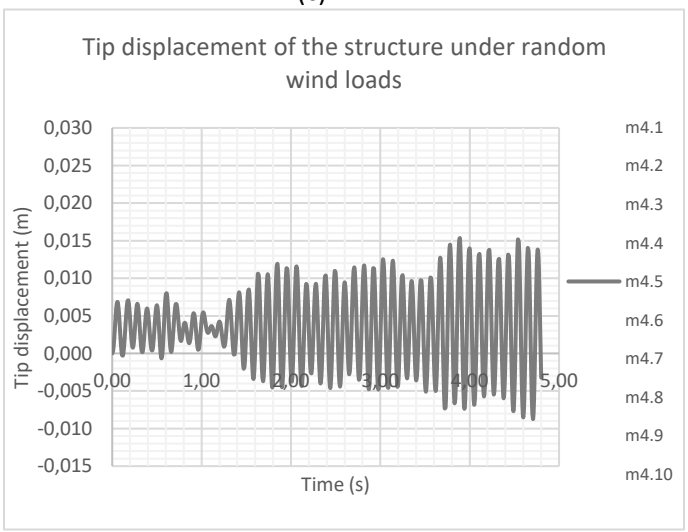
Tip displacement of the structure under random wind loads
Tip displacement (m)
0,030
0,025
0,020
0,015
0,010
0,005
0,000
-0,005
-0,010
-0,015
0,00
1,00
2,00
3,00
4,00
5,00
Time (s)
m4.1
m4.2
m4.3
m4.4
m4.5
m4.6
m4.7
m4.8
m4.9
m4.10

(e)

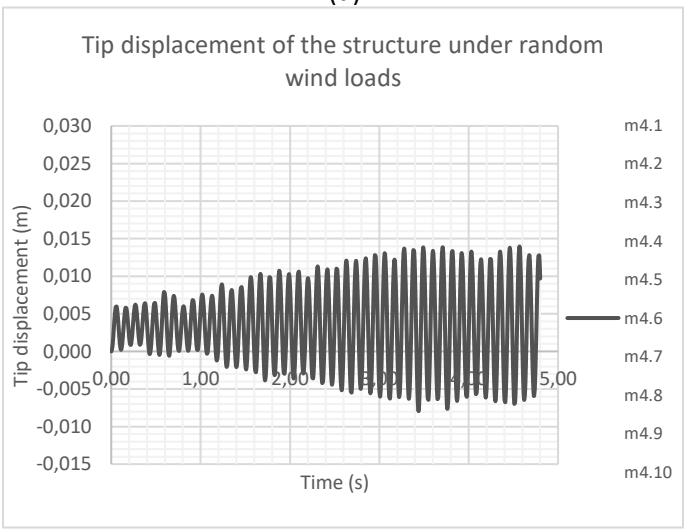
Tip displacement of the structure under random wind loads
Tip displacement (m)
0,030
0,025
0,020
0,015
0,010
0,005
0,000
-0,005
-0,010
-0,015
0,00
1,00
2,00
3,00
4,00
5,00
Time (s)
m4.1
m4.2
m4.3
m4.4
m4.5
m4.6
m4.7
m4.8
m4.9
m4.10

(f)

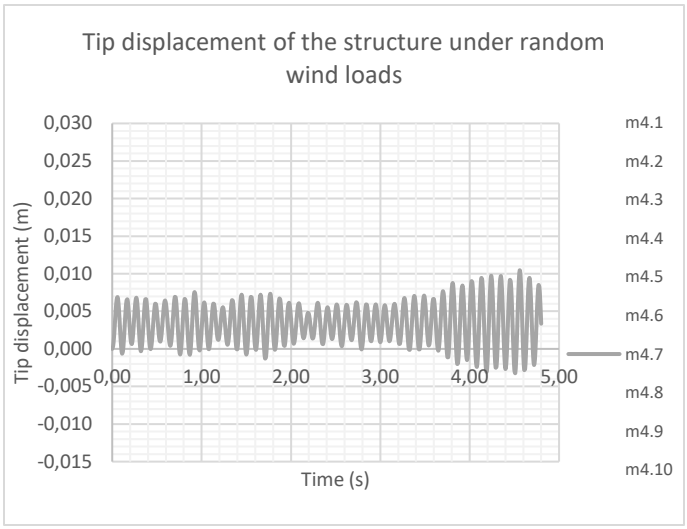

(g)

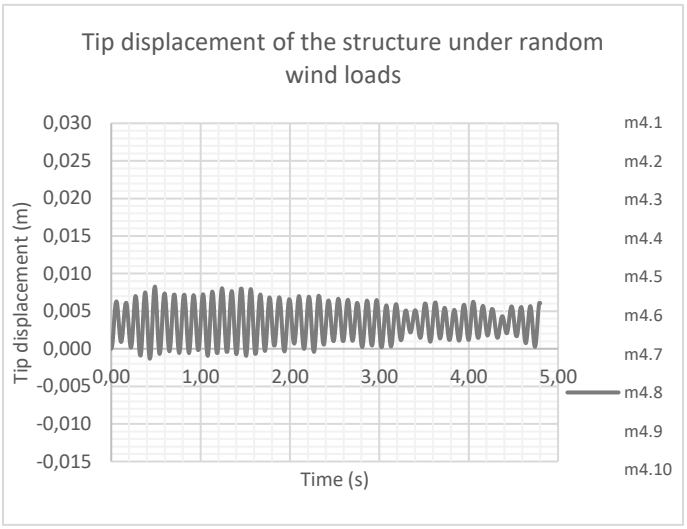

(h)

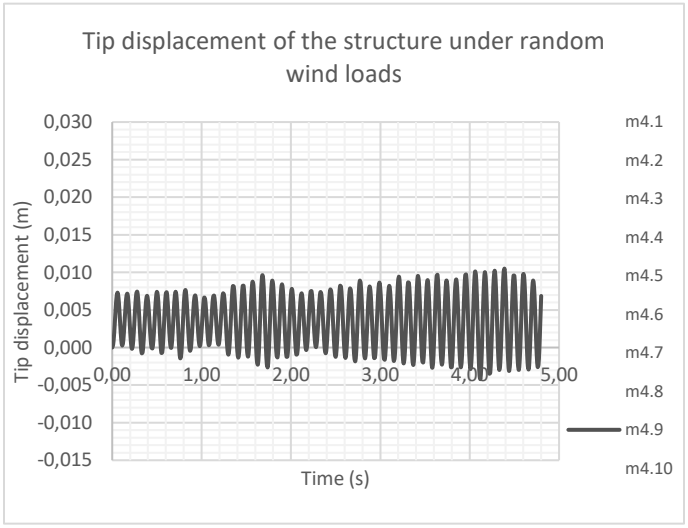

(i)

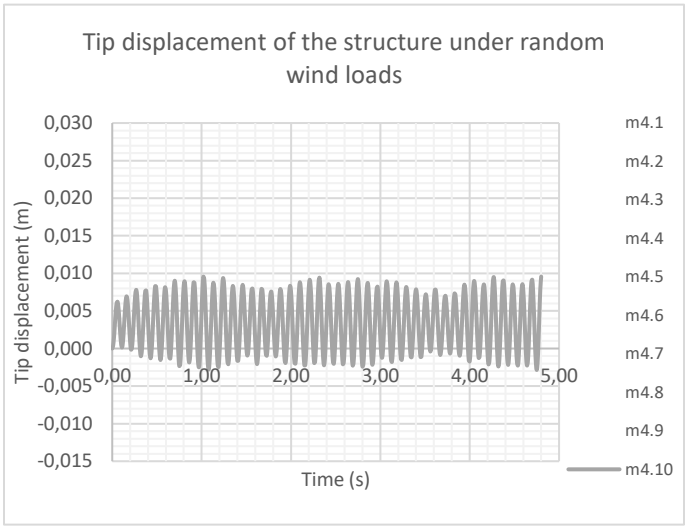

(j)

Figure C4: Horizontal tip displacement at the tip of the cantilevered arm under random wind load time histories of mean value of 40% of maximum static load (a)-(j).

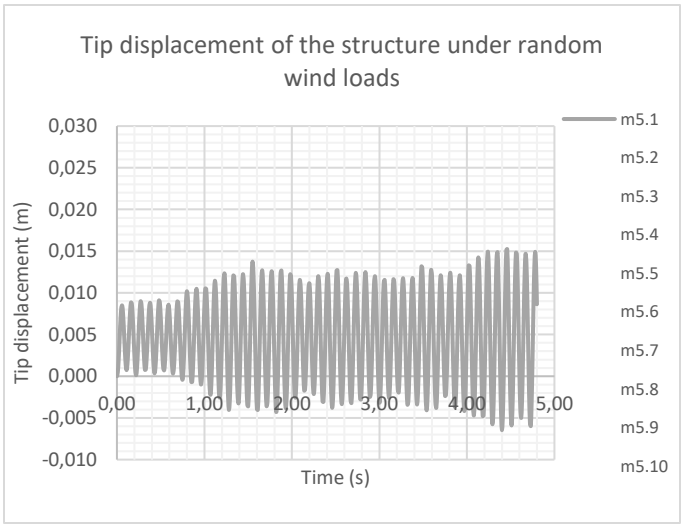
Tip displacement of the structure under random wind loads
Tip displacement (m)
0,030
0,025
0,020
0,015
0,010
0,005
0,000
-0,005
-0,010
0,00
1,00
2,00
3,00
4,00
5,00
Time (s)
m5.1
m5.2
m5.3
m5.4
m5.5
m5.6
m5.7
m5.8
m5.9
m5.10

(a)

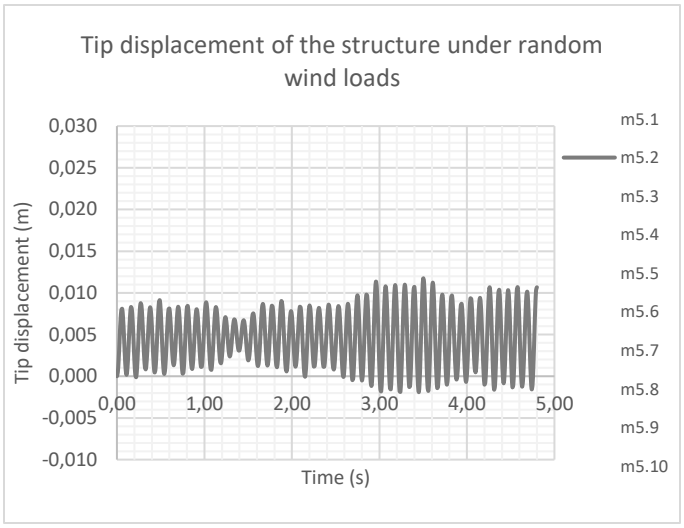
Tip displacement of the structure under random wind loads
Tip displacement (m)
0,030
0,025
0,020
0,015
0,010
0,005
0,000
-0,005
-0,010
0,00
1,00
2,00
3,00
4,00
5,00
Time (s)
m5.1
m5.2
m5.3
m5.4
m5.5
m5.6
m5.7
m5.8
m5.9
m5.10

(b)

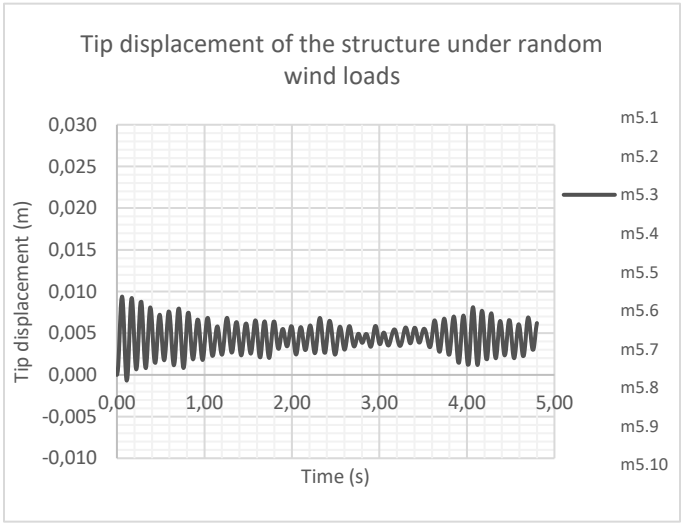
Tip displacement of the structure under random wind loads
Tip displacement (m)
0,030
0,025
0,020
0,015
0,010
0,005
0,000
-0,005
-0,010
0,00
1,00
2,00
3,00
4,00
5,00
Time (s)
m5.1
m5.2
m5.3
m5.4
m5.5
m5.6
m5.7
m5.8
m5.9
m5.10

(c)

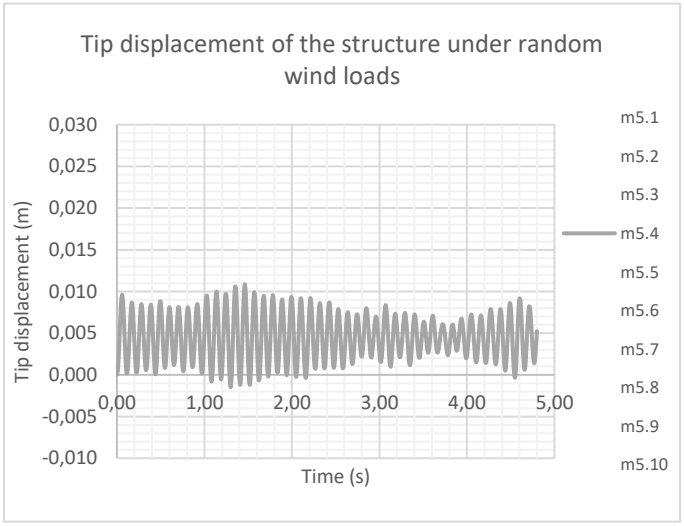
Tip displacement of the structure under random wind loads
Tip displacement (m)
0,030
0,025
0,020
0,015
0,010
0,005
0,000
-0,005
-0,010
0,00
1,00
2,00
3,00
4,00
5,00
Time (s)
m5.1
m5.2
m5.3
m5.4
m5.5
m5.6
m5.7
m5.8
m5.9
m5.10

(d)

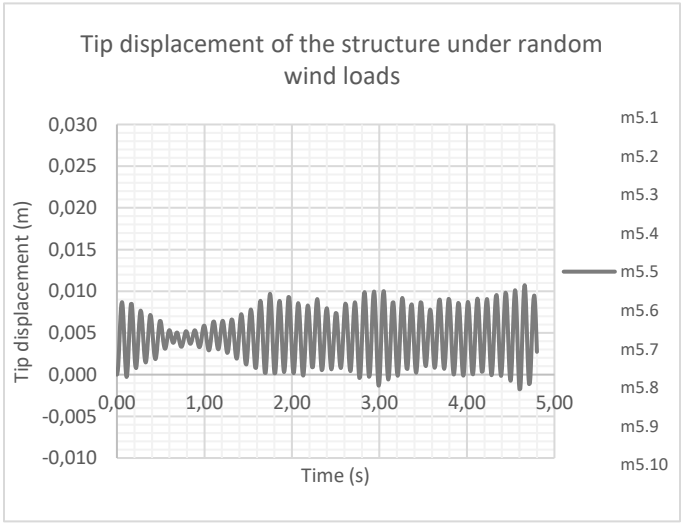
Tip displacement of the structure under random wind loads
Tip displacement (m)
0,030
0,025
0,020
0,015
0,010
0,005
0,000
-0,005
-0,010
0,00
1,00
2,00
3,00
4,00
5,00
Time (s)
m5.1
m5.2
m5.3
m5.4
m5.5
m5.6
m5.7
m5.8
m5.9
m5.10

(e)

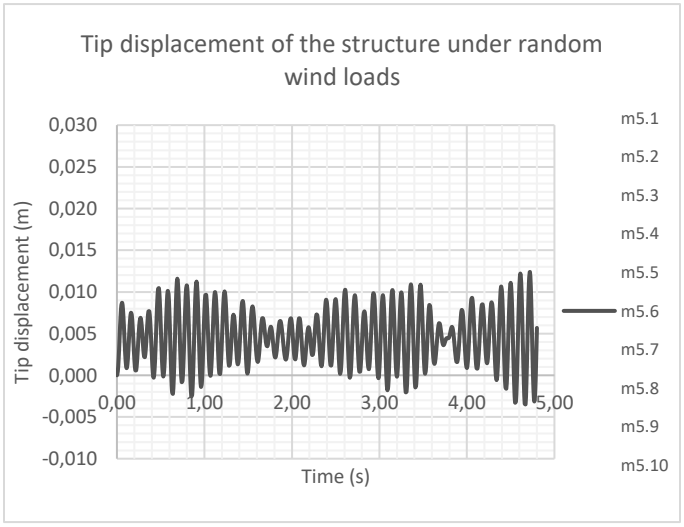
Tip displacement of the structure under random wind loads
Tip displacement (m)
0,030
0,025
0,020
0,015
0,010
0,005
0,000
-0,005
-0,010
0,00
1,00
2,00
3,00
4,00
5,00
Time (s)
m5.1
m5.2
m5.3
m5.4
m5.5
m5.6
m5.7
m5.8
m5.9
m5.10

(f)

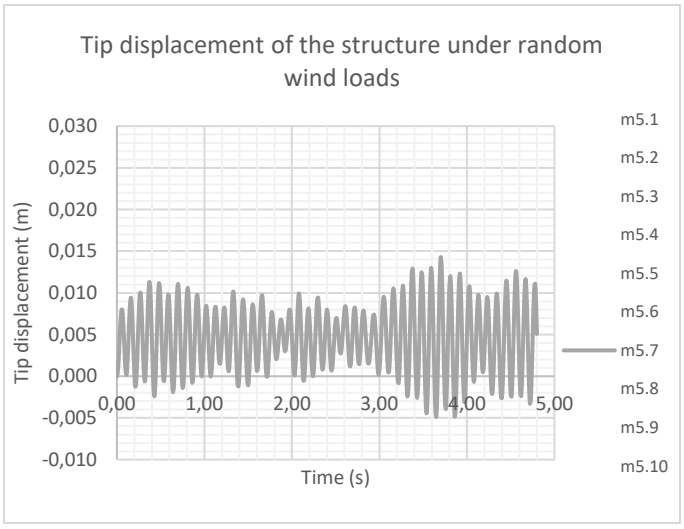

(g)

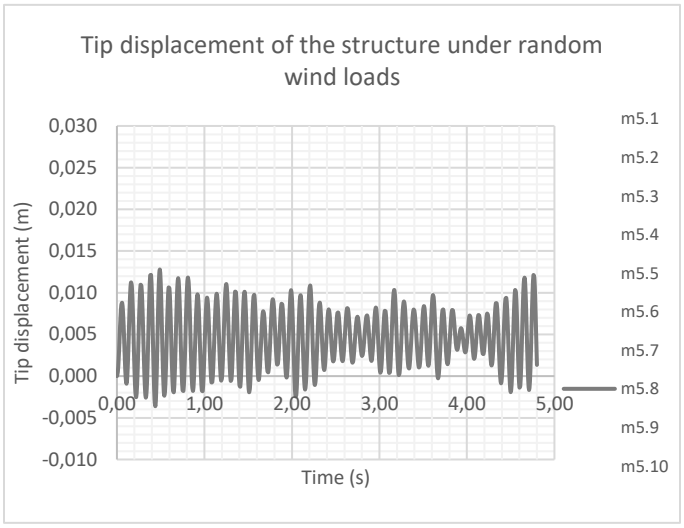

(h)

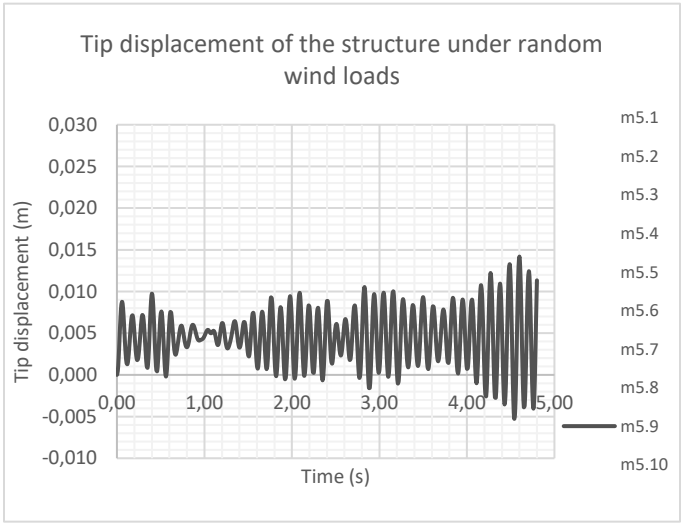

(i)

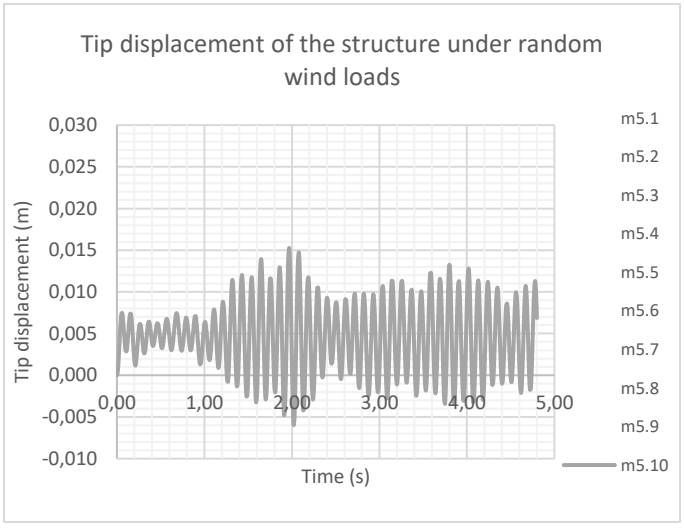

(j)

Figure C5: Horizontal tip displacement at the tip of the cantilevered arm under random wind load time histories of mean value of 50% of maximum static load (a)-(j).

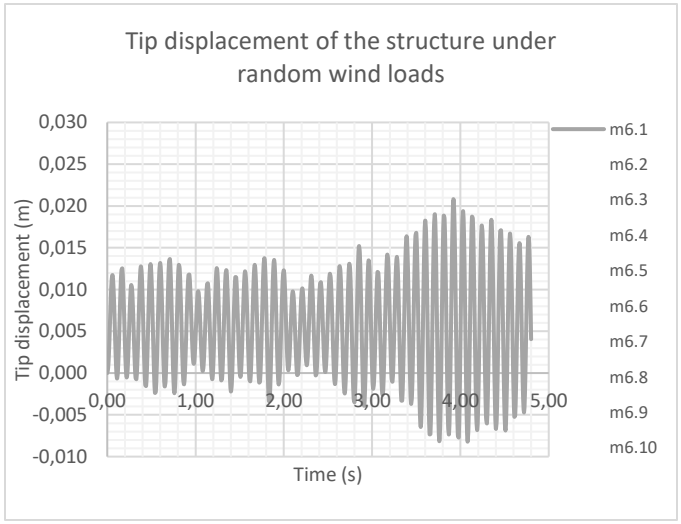
Tip displacement of the structure under random wind loads
Tip displacement (m)
0,030
0,025
0,020
0,015
0,010
0,005
0,000
-0,005
-0,010
0,00
1,00
2,00
3,00
4,00
5,00
Time (s)
m6.1
m6.2
m6.3
m6.4
m6.5
m6.6
m6.7
m6.8
m6.9
m6.10

(a)

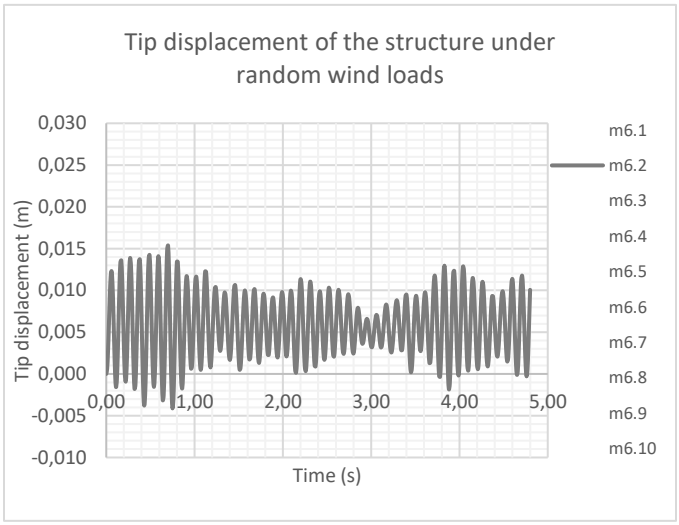
Tip displacement of the structure under random wind loads
Tip displacement (m)
0,030
0,025
0,020
0,015
0,010
0,005
0,000
-0,005
-0,010
0,00
1,00
2,00
3,00
4,00
5,00
Time (s)
m6.1
m6.2
m6.3
m6.4
m6.5
m6.6
m6.7
m6.8
m6.9
m6.10

(b)

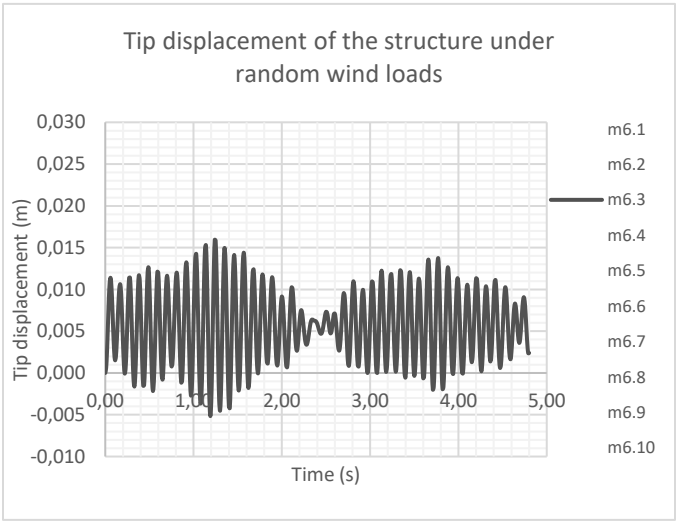
Tip displacement of the structure under random wind loads
Tip displacement (m)
0,030
0,025
0,020
0,015
0,010
0,005
0,000
-0,005
-0,010
0,00
1,00
2,00
3,00
4,00
5,00
Time (s)
m6.1
m6.2
m6.3
m6.4
m6.5
m6.6
m6.7
m6.8
m6.9
m6.10

(c)

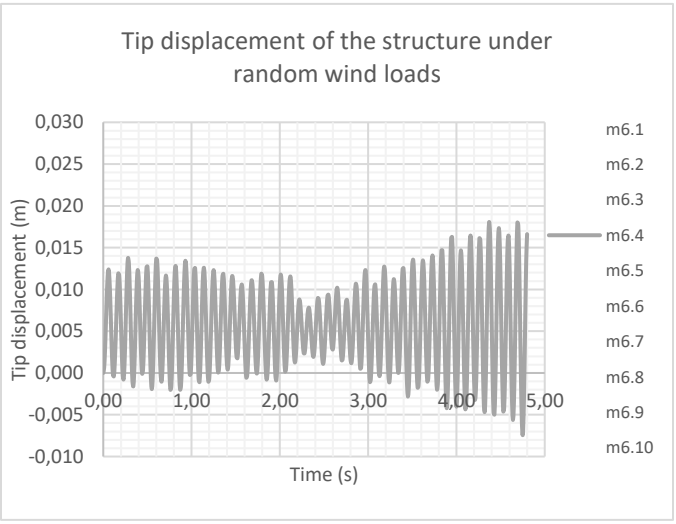
Tip displacement of the structure under random wind loads
Tip displacement (m)
0,030
0,025
0,020
0,015
0,010
0,005
0,000
-0,005
-0,010
0,00
1,00
2,00
3,00
4,00
5,00
Time (s)
m6.1
m6.2
m6.3
m6.4
m6.5
m6.6
m6.7
m6.8
m6.9
m6.10

(d)

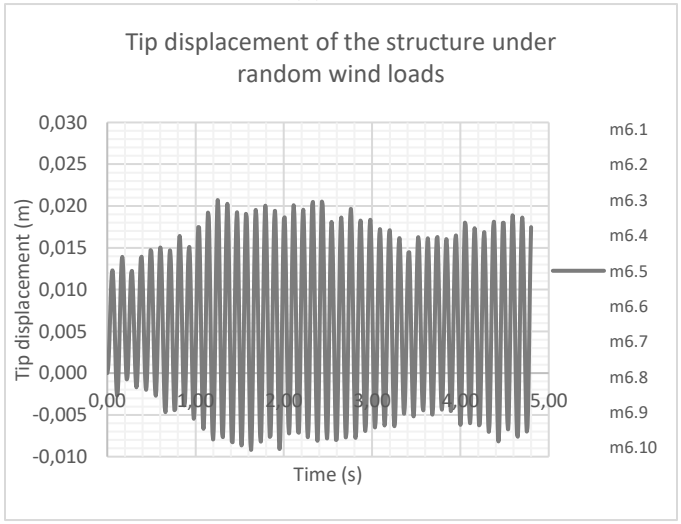
Tip displacement of the structure under random wind loads
Tip displacement (m)
0,030
0,025
0,020
0,015
0,010
0,005
0,000
-0,005
-0,010
0,00
1,00
2,00
3,00
4,00
5,00
Time (s)
m6.1
m6.2
m6.3
m6.4
m6.5
m6.6
m6.7
m6.8
m6.9
m6.10

(e)

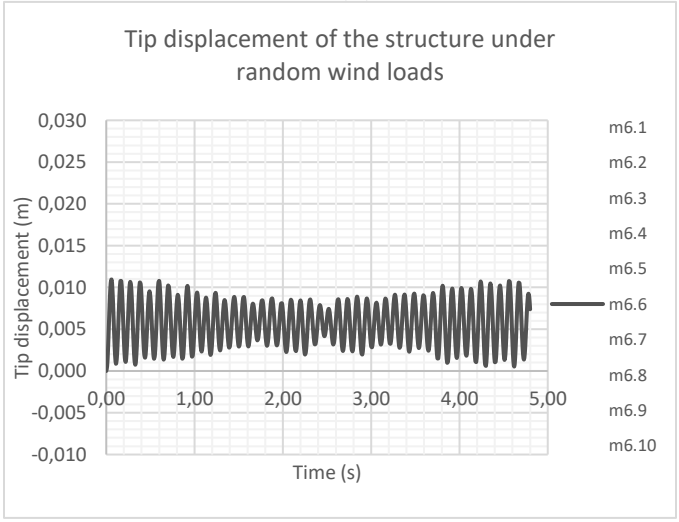
Tip displacement of the structure under random wind loads
Tip displacement (m)
0,030
0,025
0,020
0,015
0,010
0,005
0,000
-0,005
-0,010
0,00
1,00
2,00
3,00
4,00
5,00
Time (s)
m6.1
m6.2
m6.3
m6.4
m6.5
m6.6
m6.7
m6.8
m6.9
m6.10

(f)

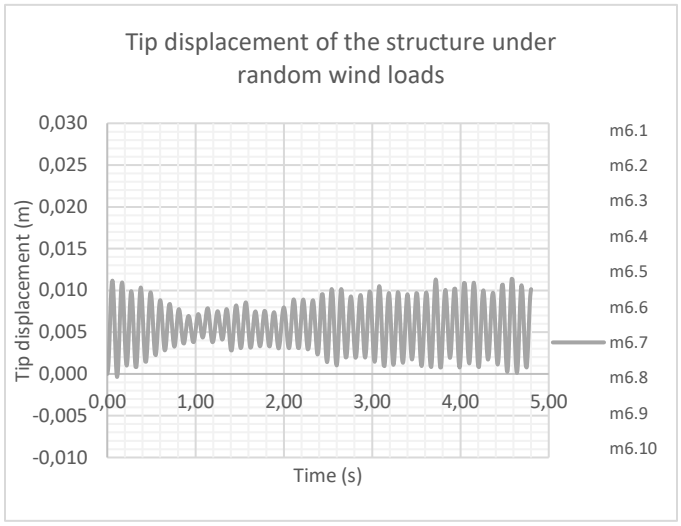

(g)

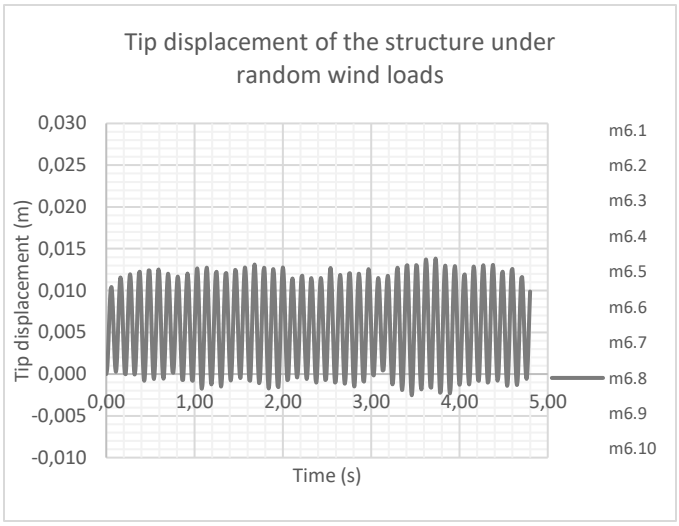

(h)

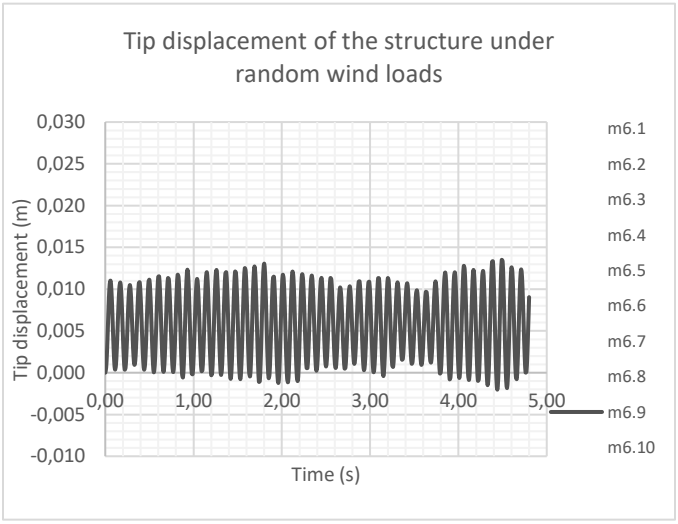

(i)

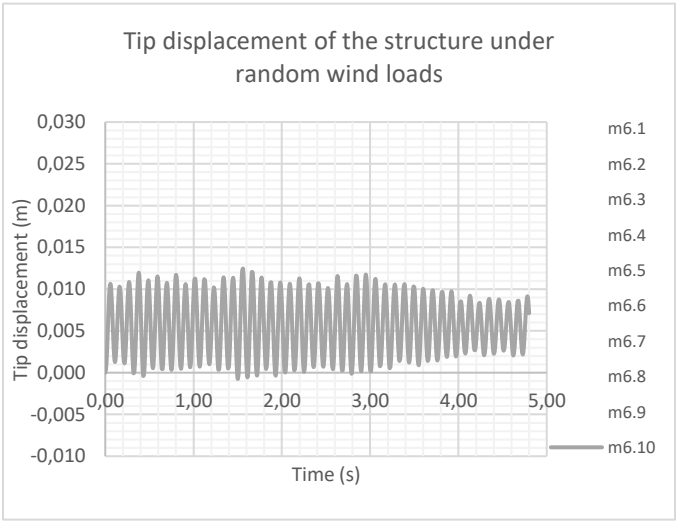

(j)

Figure C6: Horizontal tip displacement at the tip of the cantilevered arm under random wind load time histories of mean value of 60% of maximum static load (a)-(j).

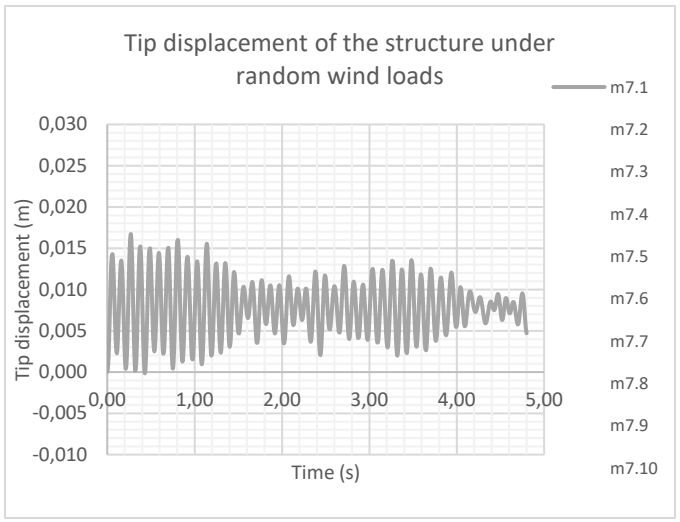
Tip displacement of the structure under random wind loads
Tip displacement (m)
0,030
0,025
0,020
0,015
0,010
0,005
0,000
-0,005
-0,010
0,00
1,00
2,00
3,00
4,00
5,00
Time (s)
m7.1
m7.2
m7.3
m7.4
m7.5
m7.6
m7.7
m7.8
m7.9
m7.10

(a)

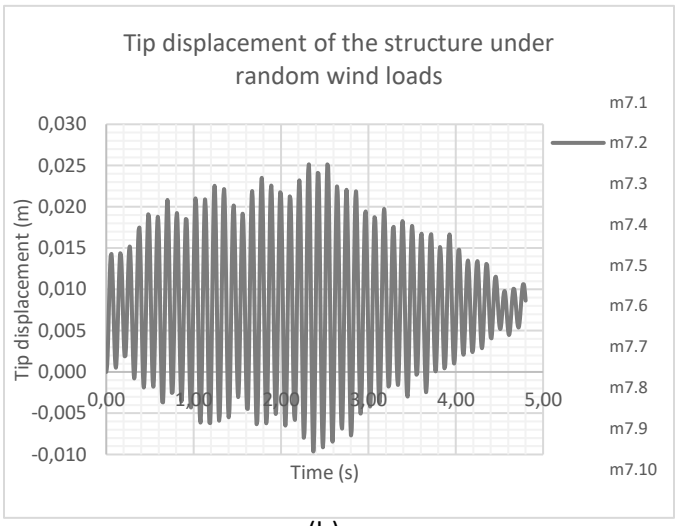
Tip displacement of the structure under random wind loads
Tip displacement (m)
0,030
0,025
0,020
0,015
0,010
0,005
0,000
-0,005
-0,010
0,00
1,00
2,00
3,00
4,00
5,00
Time (s)
m7.1
m7.2
m7.3
m7.4
m7.5
m7.6
m7.7
m7.8
m7.9
m7.10

(b)

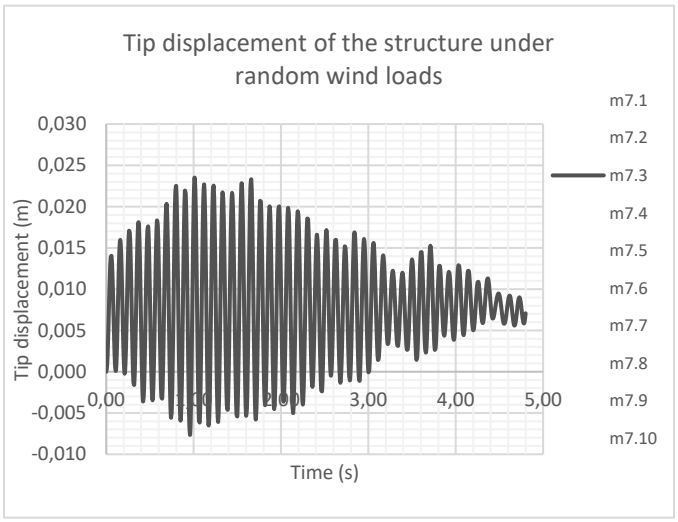
Tip displacement of the structure under random wind loads
Tip displacement (m)
0,030
0,025
0,020
0,015
0,010
0,005
0,000
-0,005
-0,010
0,00
1,00
2,00
3,00
4,00
5,00
Time (s)
m7.1
m7.2
m7.3
m7.4
m7.5
m7.6
m7.7
m7.8
m7.9
m7.10

(c)

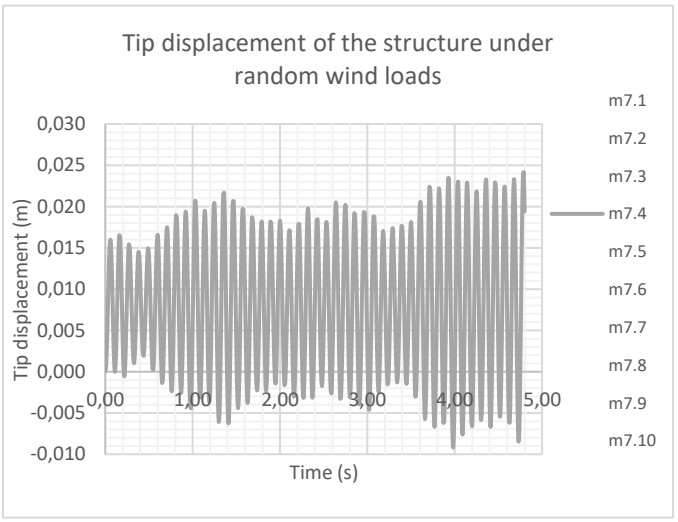
Tip displacement of the structure under random wind loads
Tip displacement (m)
0,030
0,025
0,020
0,015
0,010
0,005
0,000
-0,005
-0,010
0,00
1,00
2,00
3,00
4,00
5,00
Time (s)
m7.1
m7.2
m7.3
m7.4
m7.5
m7.6
m7.7
m7.8
m7.9
m7.10

(d)

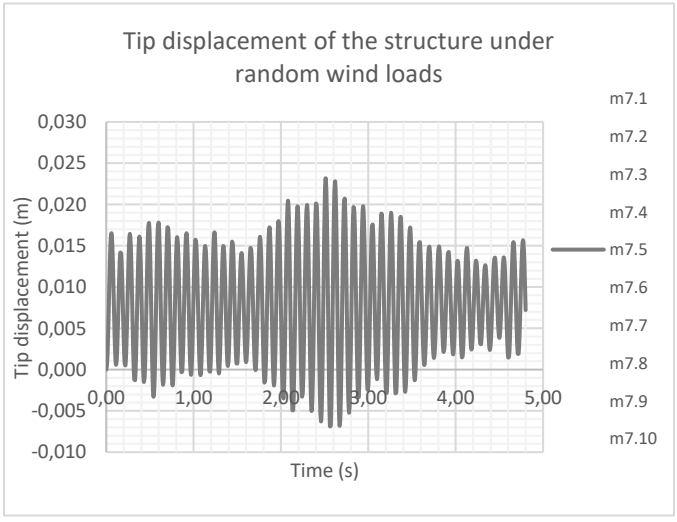
Tip displacement of the structure under random wind loads
Tip displacement (m)
0,030
0,025
0,020
0,015
0,010
0,005
0,000
-0,005
-0,010
0,00
1,00
2,00
3,00
4,00
5,00
Time (s)
m7.1
m7.2
m7.3
m7.4
m7.5
m7.6
m7.7
m7.8
m7.9
m7.10

(e)

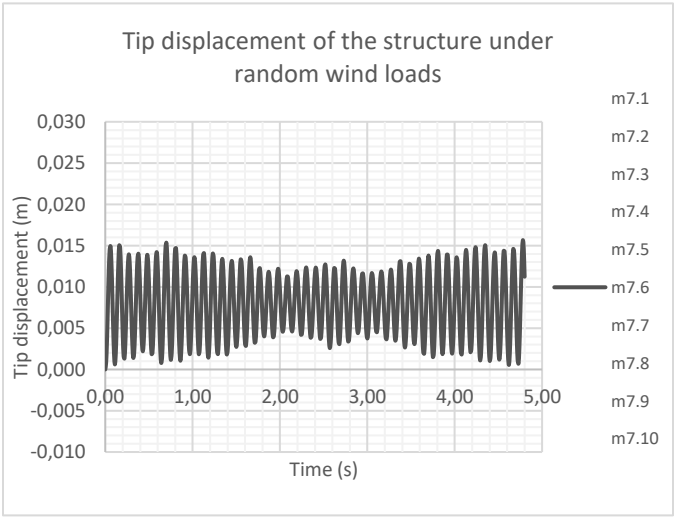
Tip displacement of the structure under random wind loads
Tip displacement (m)
0,030
0,025
0,020
0,015
0,010
0,005
0,000
-0,005
-0,010
0,00
1,00
2,00
3,00
4,00
5,00
Time (s)
m7.1
m7.2
m7.3
m7.4
m7.5
m7.6
m7.7
m7.8
m7.9
m7.10

(f)

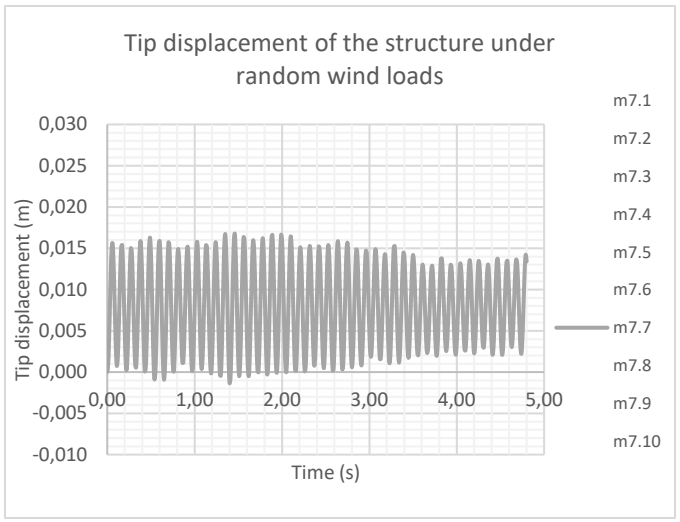

(g)

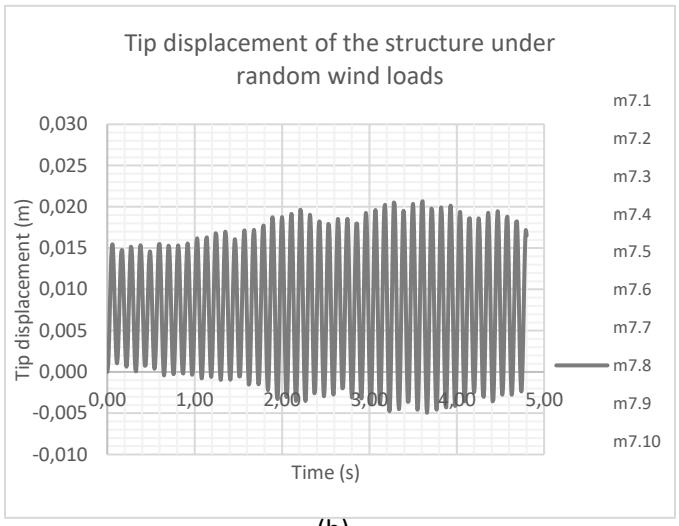

(h)

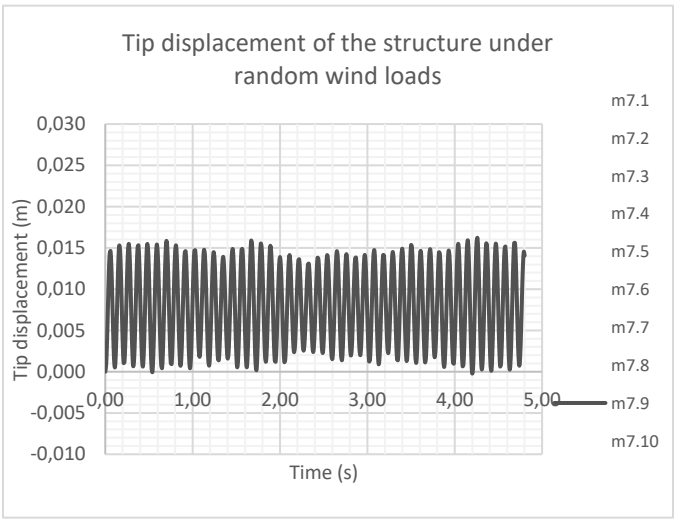

(i)

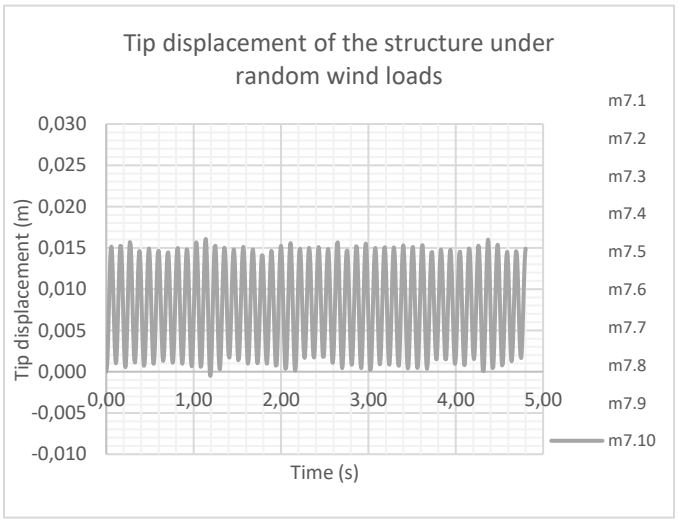

(j)

Figure C7: Horizontal tip displacement at the tip of the cantilevered arm under random wind load time histories of mean value of 70% of maximum static load (a)-(j).

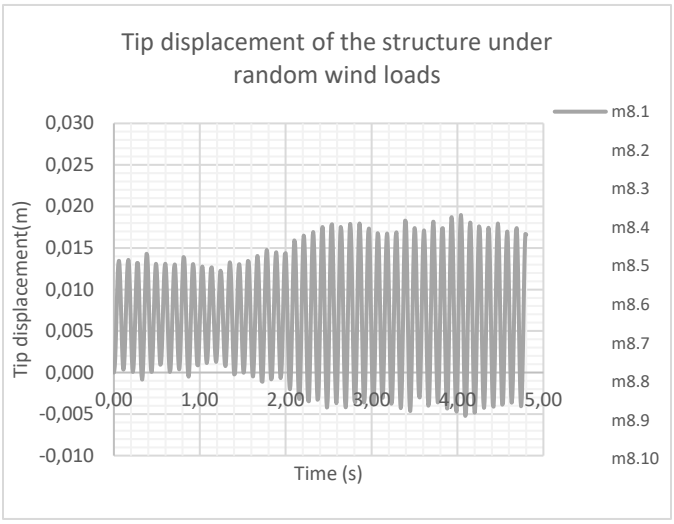
Tip displacement of the structure under random wind loads
Tip displacement(m)
0,030
0,025
0,020
0,015
0,010
0,005
0,000
-0,005
-0,010
0,00
1,00
2,00
3,00
4,00
5,00
Time (s)
m8.1
m8.2
m8.3
m8.4
m8.5
m8.6
m8.7
m8.8
m8.9
m8.10

(a)

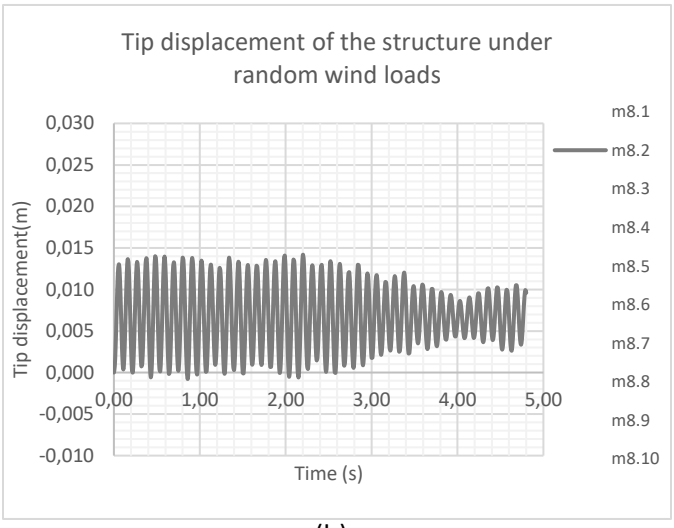
Tip displacement of the structure under random wind loads
Tip displacement(m)
0,030
0,025
0,020
0,015
0,010
0,005
0,000
-0,005
-0,010
0,00
1,00
2,00
3,00
4,00
5,00
Time (s)
m8.1
m8.2
m8.3
m8.4
m8.5
m8.6
m8.7
m8.8
m8.9
m8.10

(b)

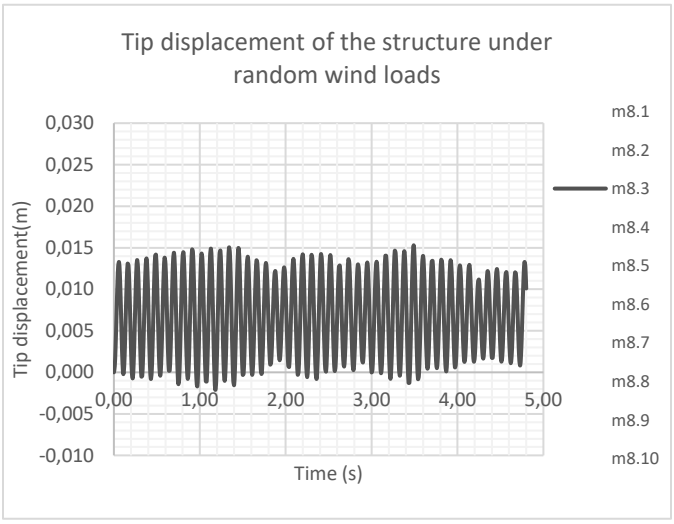
Tip displacement of the structure under random wind loads
Tip displacement(m)
0,030
0,025
0,020
0,015
0,010
0,005
0,000
-0,005
-0,010
0,00
1,00
2,00
3,00
4,00
5,00
Time (s)
m8.1
m8.2
m8.3
m8.4
m8.5
m8.6
m8.7
m8.8
m8.9
m8.10

(c)

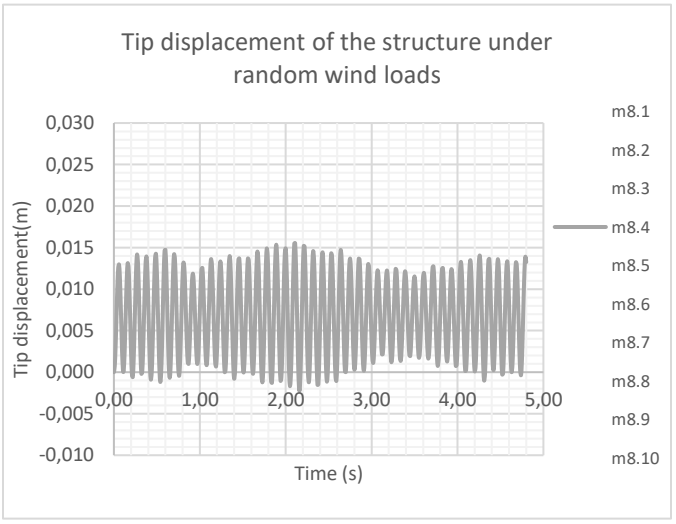
Tip displacement of the structure under random wind loads
Tip displacement(m)
0,030
0,025
0,020
0,015
0,010
0,005
0,000
-0,005
-0,010
0,00
1,00
2,00
3,00
4,00
5,00
Time (s)
m8.1
m8.2
m8.3
m8.4
m8.5
m8.6
m8.7
m8.8
m8.9
m8.10

(d)

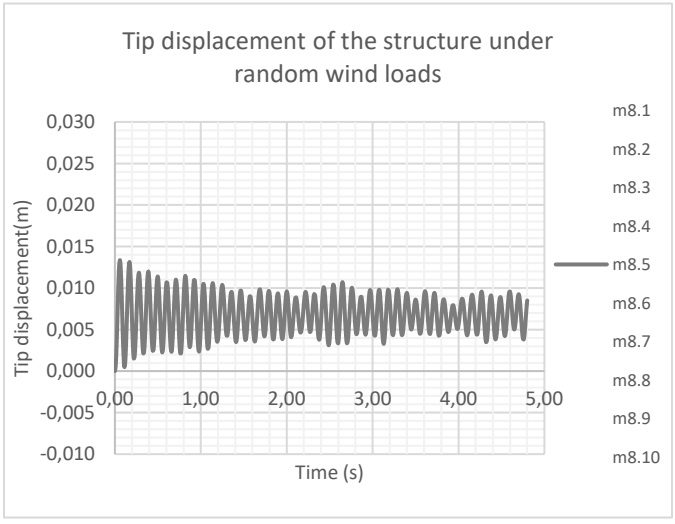
Tip displacement of the structure under random wind loads
Tip displacement(m)
0,030
0,025
0,020
0,015
0,010
0,005
0,000
-0,005
-0,010
0,00
1,00
2,00
3,00
4,00
5,00
Time (s)
m8.1
m8.2
m8.3
m8.4
m8.5
m8.6
m8.7
m8.8
m8.9
m8.10

(e)

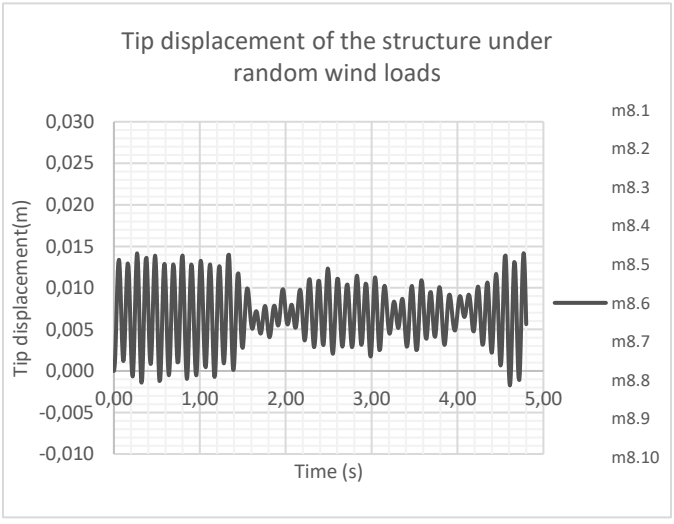
Tip displacement of the structure under random wind loads
Tip displacement(m)
0,030
0,025
0,020
0,015
0,010
0,005
0,000
-0,005
-0,010
0,00
1,00
2,00
3,00
4,00
5,00
Time (s)
m8.1
m8.2
m8.3
m8.4
m8.5
m8.6
m8.7
m8.8
m8.9
m8.10

(f)

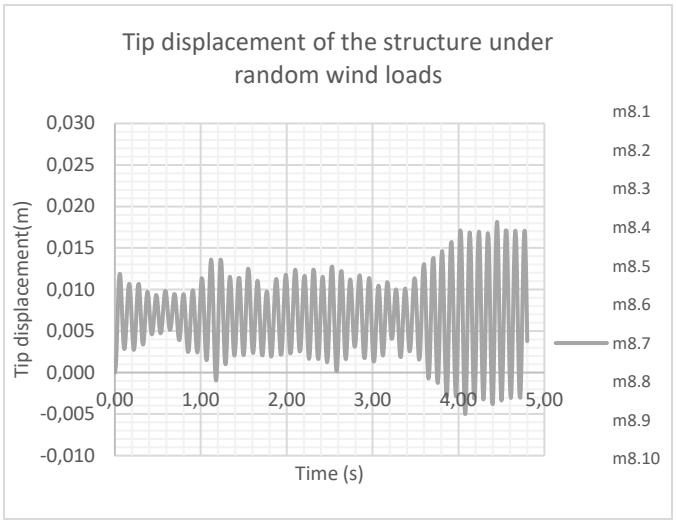

(g)

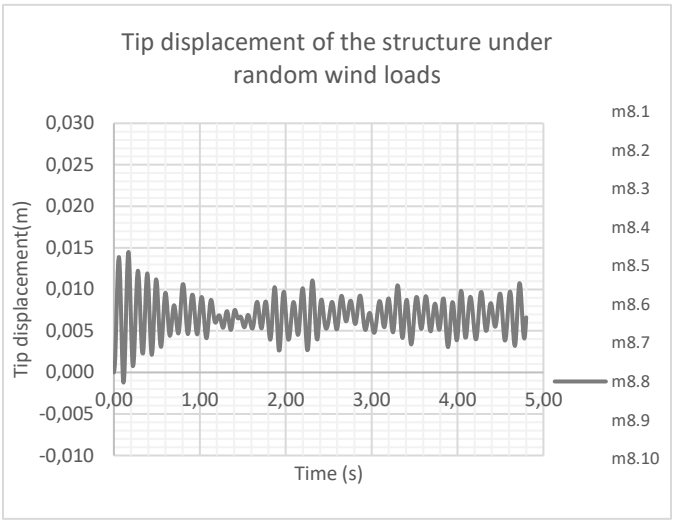

(h)

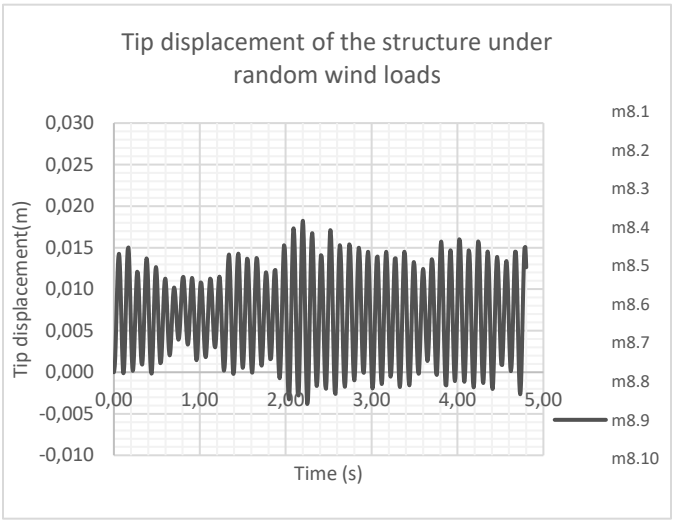

(i)

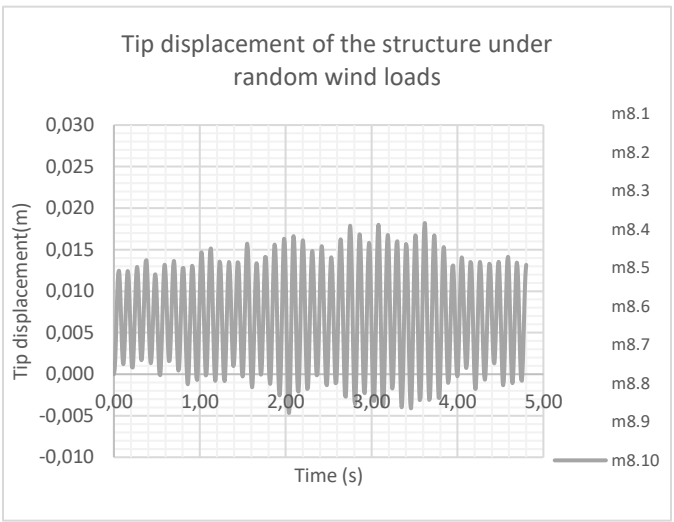

(j)

Figure C8: Horizontal tip displacement at the tip of the cantilevered arm under random wind load time histories of mean value of 80% of maximum static load (a)-(j).

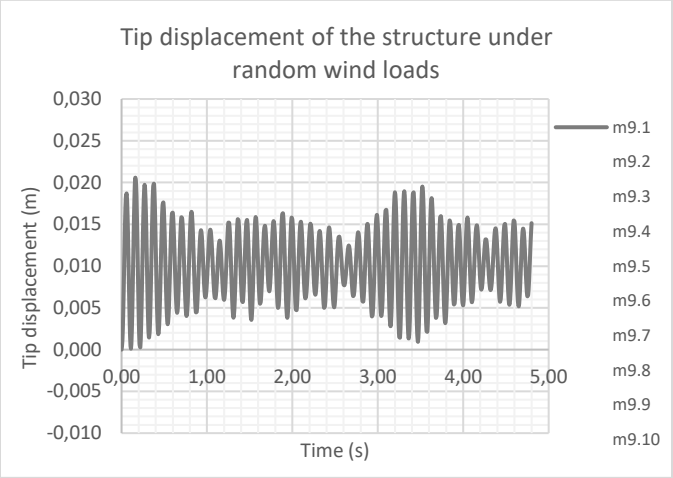
Tip displacement of the structure under random wind loads
Tip displacement (m)
0,030
0,025
0,020
0,015
0,010
0,005
0,000
-0,005
-0,010
0,00
1,00
2,00
3,00
4,00
5,00
Time (s)
m9.1
m9.2
m9.3
m9.4
m9.5
m9.6
m9.7
m9.8
m9.9
m9.10

(a)

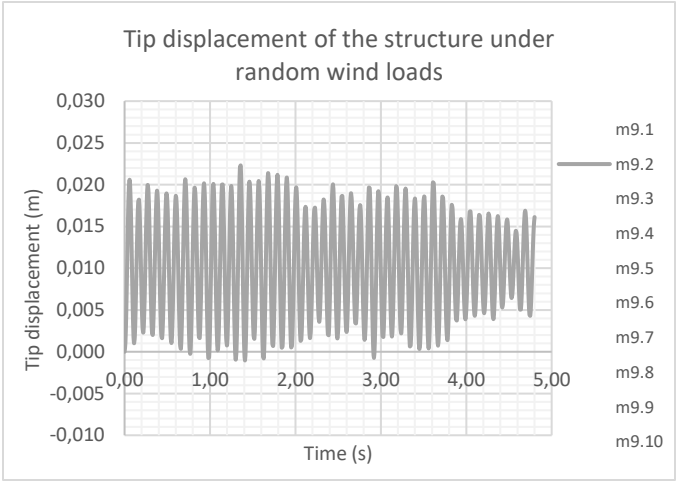
Tip displacement of the structure under random wind loads
Tip displacement (m)
0,030
0,025
0,020
0,015
0,010
0,005
0,000
-0,005
-0,010
0,00
1,00
2,00
3,00
4,00
5,00
Time (s)
m9.1
m9.2
m9.3
m9.4
m9.5
m9.6
m9.7
m9.8
m9.9
m9.10

(b)

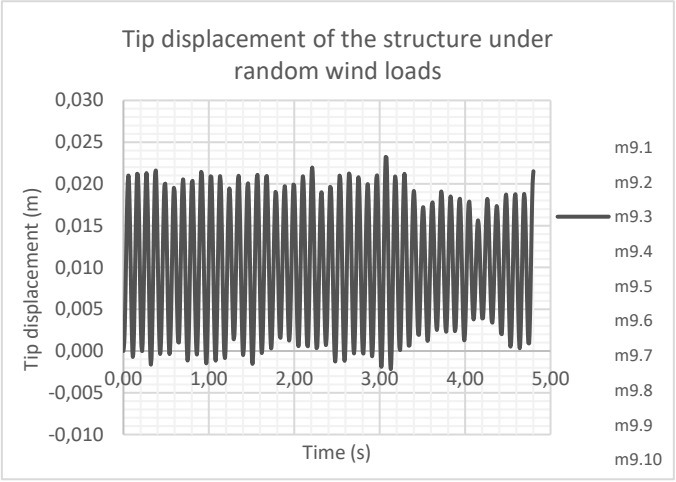
Tip displacement of the structure under random wind loads
Tip displacement (m)
0,030
0,025
0,020
0,015
0,010
0,005
0,000
-0,005
-0,010
0,00
1,00
2,00
3,00
4,00
5,00
Time (s)
m9.1
m9.2
m9.3
m9.4
m9.5
m9.6
m9.7
m9.8
m9.9
m9.10

(c)

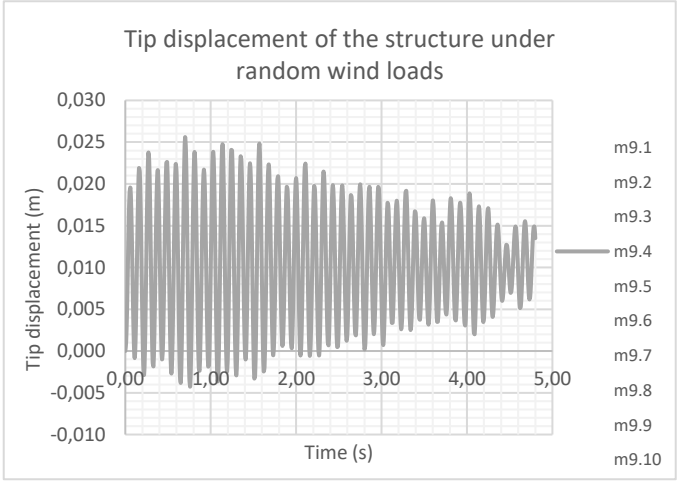
Tip displacement of the structure under random wind loads
Tip displacement (m)
0,030
0,025
0,020
0,015
0,010
0,005
0,000
-0,005
-0,010
0,00
1,00
2,00
3,00
4,00
5,00
Time (s)
m9.1
m9.2
m9.3
m9.4
m9.5
m9.6
m9.7
m9.8
m9.9
m9.10

(d)

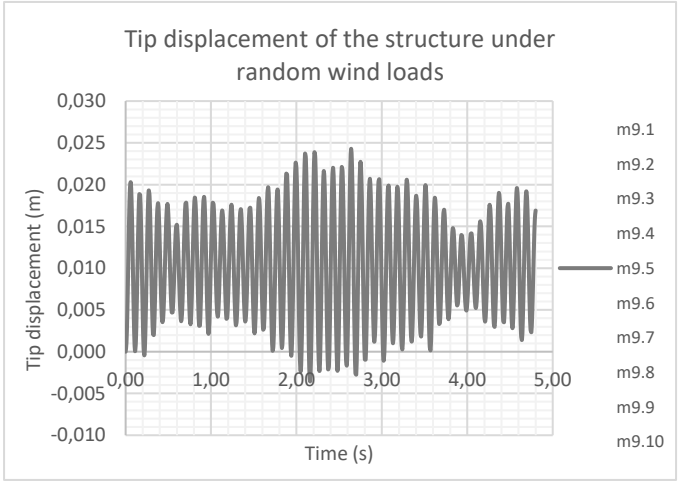
Tip displacement of the structure under random wind loads
Tip displacement (m)
0,030
0,025
0,020
0,015
0,010
0,005
0,000
-0,005
-0,010
0,00
1,00
2,00
3,00
4,00
5,00
Time (s)
m9.1
m9.2
m9.3
m9.4
m9.5
m9.6
m9.7
m9.8
m9.9
m9.10

(e)

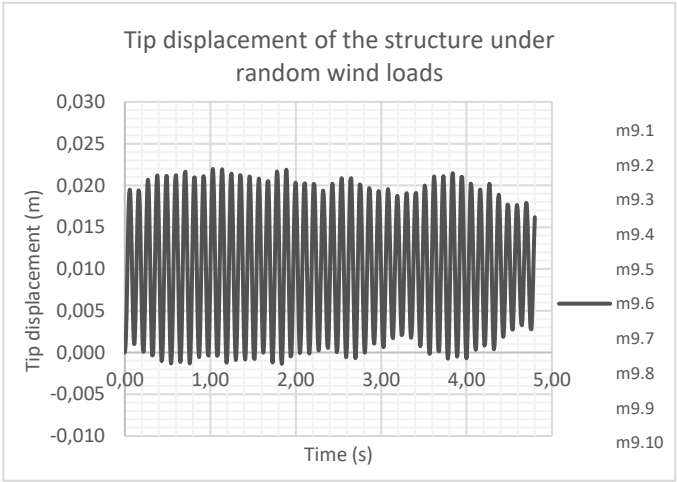
Tip displacement of the structure under random wind loads
Tip displacement (m)
0,030
0,025
0,020
0,015
0,010
0,005
0,000
-0,005
-0,010
0,00
1,00
2,00
3,00
4,00
5,00
Time (s)
m9.1
m9.2
m9.3
m9.4
m9.5
m9.6
m9.7
m9.8
m9.9
m9.10

(f)

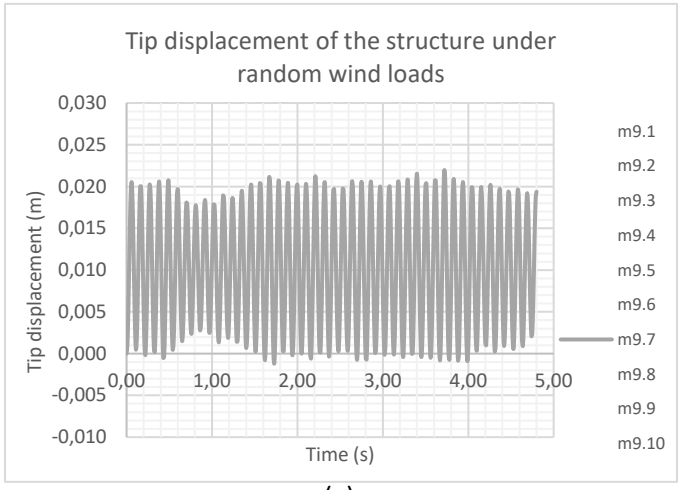

(g)

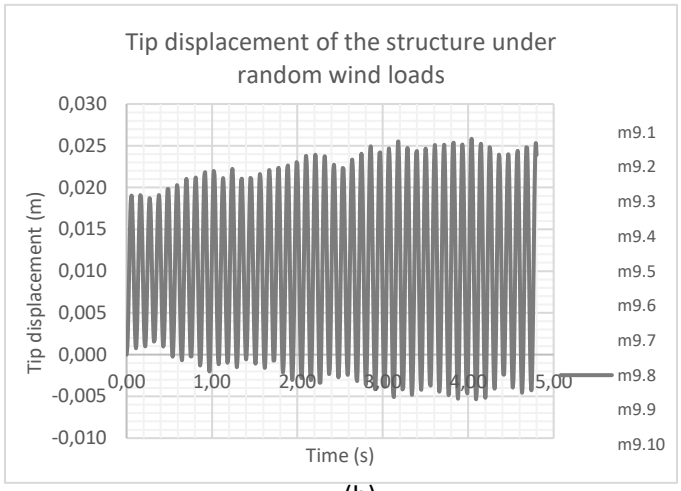

(h)

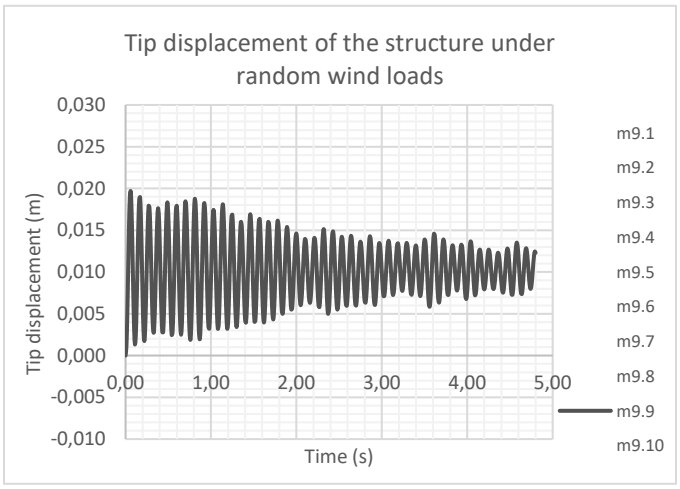

(i)

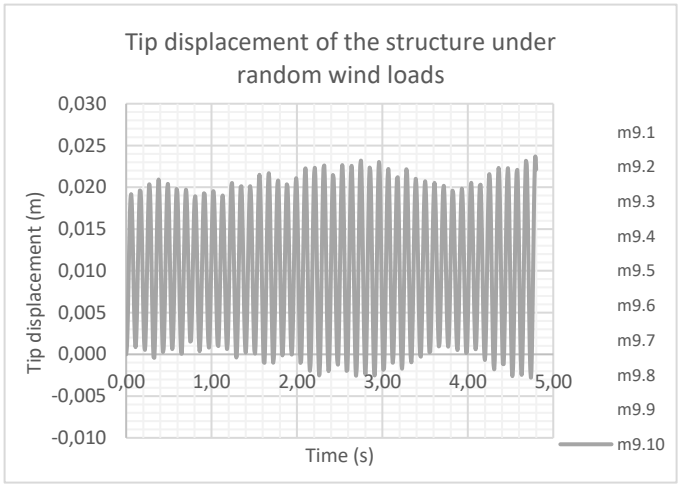

(j)

Figure C9: Horizontal tip displacement at the tip of the cantilevered arm under random wind load time histories of mean value of 90% of maximum static load (a)-(j).

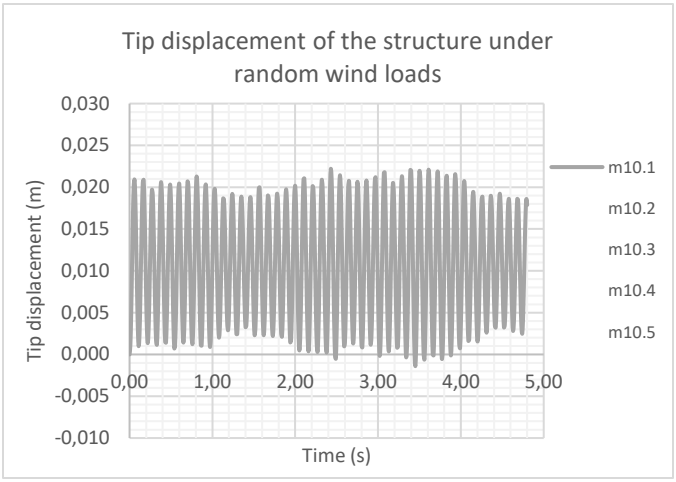

(a)

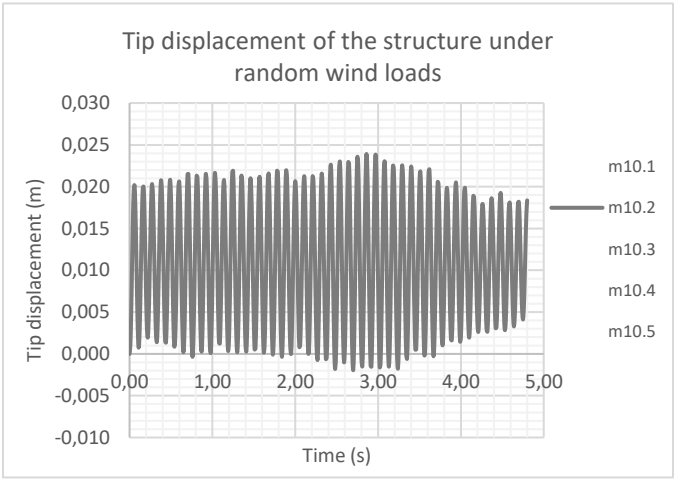

(b)

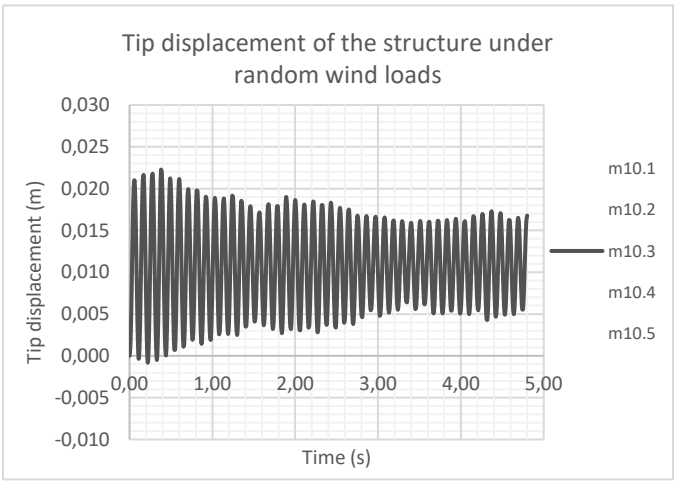

(c)

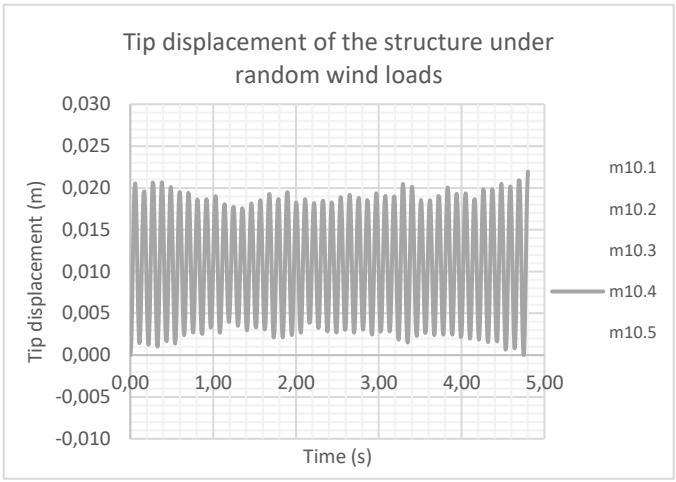

(d)

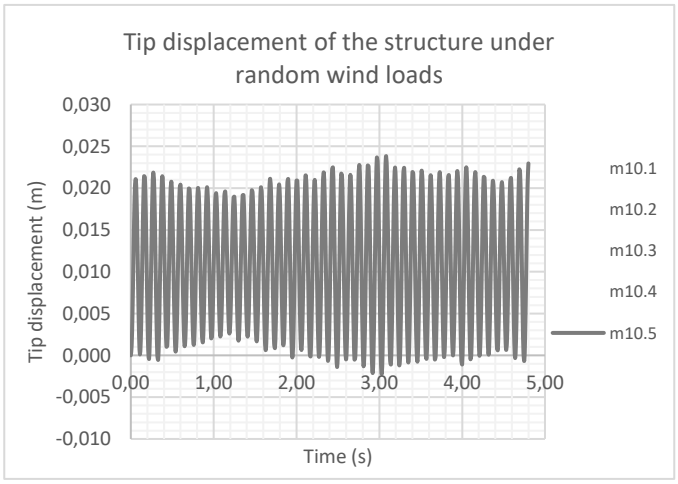

(e)

Figure C10: Horizontal tip displacement at the tip of the cantilevered arm under random wind load time histories of mean value of 100% of maximum static load (a)-(e).

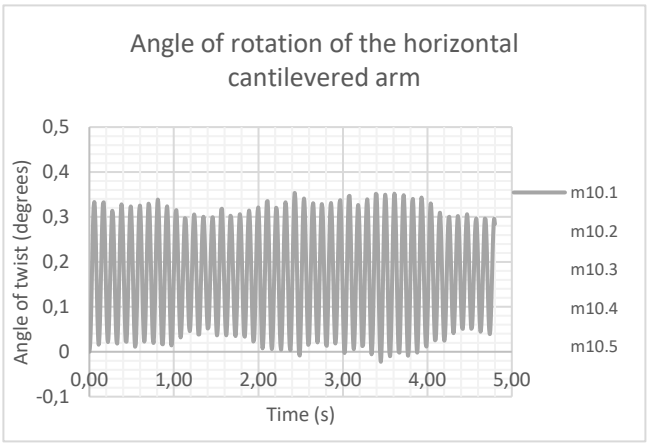

(a)

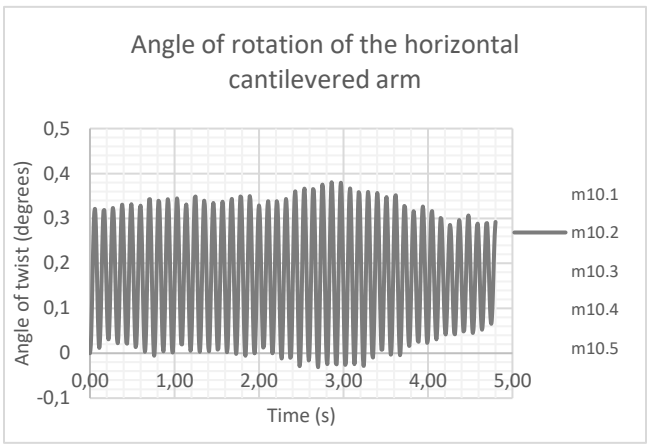

(b)

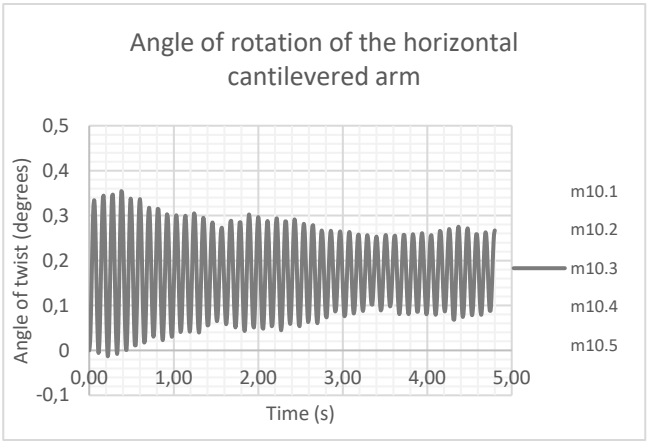

(c)

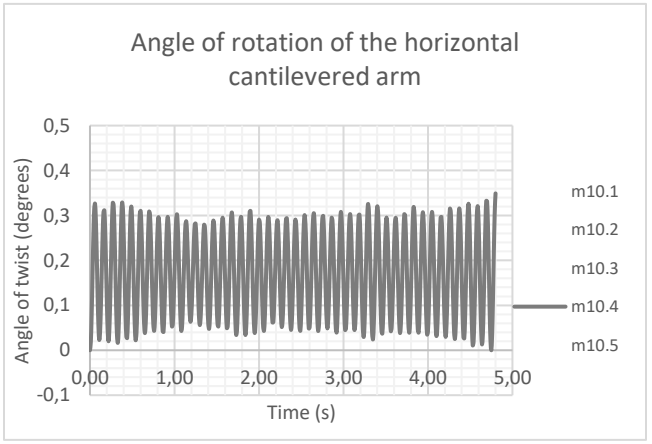

(d)

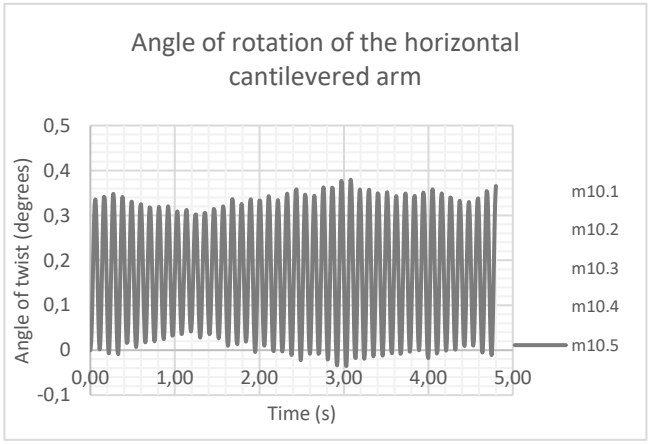

(e)

Figure C11: Angle of rotation of the cantilevered arm under random wind load time histories of mean value of 100% of maximum static load (a)-(e).